# Epitaxial growth of GaN quantum dots on smooth AlN

vorgelegt von

Dipl.-Ing. Konrad Bellmann

geb. in Dresden

von der Fakultät II – Mathematik und Naturwissenschaften
der Technischen Universität Berlin
zur Erlangung des akademischen Grades

Doktor der Naturwissenschaften

– Dr. rer. nat. –

genehmigte Dissertation

Promotionsausschuss:

| | |
|---|---|
| Vorsitzender: | Prof. Dr. Michael Lehmann |
| Gutachter: | Prof. Dr. Michael Kneissl |
| Gutachter: | Prof. Dr. Ferdinand Scholz |
| Gutachter: | Prof. Dr. Udo W. Pohl |

Tag der wissenschaftlichen Aussprache: 16.02.2018

Berlin 2018

*Knowledge is the food of the soul.*
— Plato

dedicated to my beloved family

# Abstract

A fundamental limitation of current quantum dot based monolithic quantum-devices emitting single or entangled photons is the operation at cryogenic temperatures. A straightforward solution is the use of group-III nitrides. In particular, the large bandgap difference between the two binary compounds GaN and AlN of 2.6 eV can provide superior exciton confinement for an energy separation between distinct eigenstates larger than 25 meV, which is required for room temperature operation. In fact, single photon emission from GaN quantum dots has been demonstrated up to 350 K. Despite the very promising optical properties, growing GaN quantum dots on AlN by metalorganic vapor-phase epitaxy is still very challenging. Two major reasons are the need of smooth AlN substrates for a homogenous GaN nucleation, and the lattice mismatch between GaN and AlN with $\epsilon_{\mathrm{GaN/AlN}} = 2.4\%$. The latter is similar to the required minimum lattice mismatch of about $\epsilon = 2.5\%$ for Stranski-Krastanow quantum dot growth.

This thesis aims at establishing GaN quantum dot growth on AlN buffer layers by metalorganic vapor-phase epitaxy within an in-depth study of homoepitaxial and heteroepitaxial growth processes. In order to address this in a comprehensive manner, fundamental physics are illustrated in theoretical models and compared with extensive growth studies. Additionally, optical properties of GaN quantum dots are presented to demonstrate the feasibility for optical applications. The manuscript is divided into three major parts.

In the first part, the homoepitaxial growth transition between common step-bunching growth and desired step-flow growth is studied for AlN. A surface diffusion model is presented and examined via a novel Monte-Carlo approach, which shows an extended growth window for the favored step-flow growth by increasing the vicinal terrace width of the substrate (small offcut angles). The results are experimentally applied to pseudo-homoepitaxial AlN growth on (0001) AlN templates with different growth conditions and offcut angles. A change of the surface termination is observed within the presented parameter window yielding step-flow growth under high $V/III > 11$ and step-bunching

growth under low $V/III < 11$. Additionally, small offcut angles maintain step-flow growth essential for homogenous GaN quantum dot nucleation.

In the second part, the influence of a growth interruption on the quantum dot formation is investigated. After the two-dimensional GaN growth under a high $V/III = 1200$, a morphology transition occurs during the growth interruption without ammonia present. This process is governed by material desorption yielding flat GaN quantum dots with very low aspect ratios $< 0.1$. Capped samples exhibit typical optical properties of flat elongated GaN quantum dots, like excitons with a fine-structure splitting of about $(7.5 \pm 1.0)$ meV.

In the third part, the influence of the surface energy on the heteroepitaxial growth transition between two-dimensional Frank-van-der-Merve growth and three-dimensional Stranski-Krastanow growth is studied for GaN on AlN. A qualitative growth model is presented and the influence of the surface energy is discussed yielding two-dimensional growth for high surface energies and three-dimensional growth for low surface energies. During growth, the surface energy can be controlled via the V/III ratio yielding two-dimensional growth for high $V/III \geq 300$ and three-dimensional growth for low $V/III \leq 150$. A detailed investigation of the achieved Stranski-Krastanow quantum dots yield a characteristic wetting layer thickness of $(2.5 \pm 1)$ ML and a truncated pyramidal shape with $\{10\bar{1}3\}$ side facets. Capped samples exhibit typical optical properties of Stranski-Krastanow GaN quantum dots, like excitons and biexcitons with binding-energies of $(12 \pm 9)$ meV.

# Zusammenfassung

Aktuelle Quanten-Bauelemente mit Quantenpunkten in der aktiven Zone besitzen auf Grund der verwendeten Materialsysteme eine eingeschränkte Betriebstemperatur bei flüssigem Stickstoff oder niedriger. Eine naheliegende Lösung bietet die Verwendung von Gruppe-III-Nitriden. Insbesondere der große Bandlückenunterschied der beiden binären Verbindungen GaN und AlN von 2.6 eV ermöglicht einen sehr großen Exzitoneneinschluss. In nulldimensionalen Strukturen kann somit die Separation individueller exzitonischer Eigenzustände mehr als 25 meV betragen. Dies ist eine wesentliche Voraussetzung für Anwendungen bei Raumtemperatur. In der Tat wurde die Emission einzelner Photonen auch schon bis Temperaturen von 350 K berichtet. Trotz dieser vielversprechenden optischen Eigenschaften ist jedoch das kontrollierte Wachstum von GaN-Quantenpunkten mit Hilfe der metallorganischen Gasphasenepitaxie nach wie vor eine große Herausforderung. Hierbei sind zwei wesentliche Gründe identifizierbar. Zum einen werden glatte AlN-Oberflächen mit Stufenflusswachstum benötigt. Zum anderen entspricht die Gitterfehlanpassung zwischen GaN und AlN mit $\epsilon_{\mathrm{GaN/AlN}} = 2.4\%$ genau der minimalen Gitterfehlanpassung des Stranski-Krastanow Wachstums von $\epsilon = 2.5\%$.

Ziel der vorliegenden Arbeit ist es, GaN-Quantenpunkte auf AlN-Oberflächen epitaktisch abzuscheiden und dabei das homoepitaktische und heteroepitaktische Wachstum ausführlich zu untersuchen. Zuerst werden grundlegende physikalische Zusammenhänge mit theoretischen Modellen diskutiert und anschließend mit gezielten Wachstumsstudien verglichen. Exemplarisch werden auch optische Eigenschaften von GaN-Quantenpunkten präsentiert als Nachweis für die Anwendbarkeit in optoelektronischen Bauelementen. Die Arbeit ist in drei Teile untergliedert.

Im ersten Teil werden im Rahmen einer homoepitaktischen Wachstumsuntersuchung zwischen Stufenfluss- und Stufenbündelwachstum glatte AlN-Oberflächen erzeugt. Hierfür wird zunächst der Übergang theoretisch mit Hilfe eines gängigen Modells durch Adatom-Diffusion beschrieben. Zur besseren Interpretation werden Oberflächen durch Monte-

Carlo-Simulationen erzeugt und analysiert. Diese gewonnenen Ergebnisse werden auf das pseudo-homoepitaktische Wachstum von AlN angewendet. Hierbei konnte innerhalb des Wachstumsfensters ein Übergang der Oberflächenterminierung beobachtet werden, welcher Stufenbündel bei geringem $V/III < 11$ und Stufenfluss bei hohem $V/III > 11$ begünstigt. Unabhängig vom V/III-Verhältnis konnten glatte Oberflächen für kleine Fehlschnitte realisiert werden.

Im zweiten Teil konnten flache GaN-Quantenpunkte mit einem sehr geringem Aspektverhältnis von $< 0.1$ erzeugt werden. Hierfür wird eine zweidimensional gewachsene GaN-Schicht durch eine Wachstumsunterbrechung in dreidimensionale Strukturen überführt, wobei vorrangig Materialdesorption identifiziert werden konnte. Optische Strukturen zeigen typische exzitonische Lumineszenzen von flachen elongierten GaN-Quantenpunkten.

Im dritten Teil der Arbeit konnten Stranski-Krastanow-GaN-Quantenpunkte erzeugt werden. Hierfür wird zunächst der Einfluss der Oberflächenenergie auf den heteroepitaktische Übergang zwischen zweidimensionalem Frank-van-der-Merve Wachstum und dreidimensionalem Stranski-Krastanow Wachstum an Hand eines qualitativen Modells erklärt. Die geringe Oberflächenenergie, welche für Stranski-Krastanow-GaN-Quantenpunkte benötigt wird, konnte experimentell bei einem $V/III \leq 150$ eingestellt werden. Eine detaillierte Analyse der Stranski-Krastanow-Quantenpunkte hat eine charakteristische Benetzungsschichtdicke von $(2.5 \pm 1)$ ML und pyramidenstumpfförmige Quantenpunke mit $\{10\bar{1}3\}$-Seidenfacetten ergeben. Optische Strukturen zeigen typische exzitonische Lumineszenzen von Stranski-Krastanow-GaN-Quantenpunkten.

# Contents


**1 Introduction** **1**

**2 Basic principles of group-III nitride epitaxy** **5**

2.1 Fundamental properties of group-III nitrides . . . . . 6

2.1.1 Bulk crystal . . . . . 6

2.1.2 Surface reconstruction . . . . . 8

2.1.3 Surface energy . . . . . 8

2.1.4 Optical properties of GaN quantum dots . . . . . 12

2.2 Epitaxial layer growth . . . . . 15

2.2.1 Substrate offcut providing vicinal terraces . . . . . 15

2.2.2 Surface energy potential for adatom kinetics . . . . . 16

2.2.3 Terrace ledge kink model . . . . . 17

2.2.4 Growth modes in homoepitaxy . . . . . 19

2.2.5 Growth modes in heteroepitaxy . . . . . 20

**3 Experimental methods** **23**

3.1 Metalorganic vapor-phase epitaxy . . . . . 24

3.2 Atomic force microscopy . . . . . 27

3.3 Electron beam lithography of mesa structures . . . . . 29

3.4 Micro photoluminescence . . . . . 32

**4 Achieving smooth step-flow AlN surfaces** **35**

4.1 Analytical model . . . . . 37

4.1.1 Derivation of equations . . . . . 37

4.1.2 Adatom density and adatom flux . . . . . 39

4.2 Monte-Carlo approach . . . . . 45

4.2.1 Monte-Carlo algorithm . . . . . 45

4.2.2 Morphology evolution for different growth conditions . . . . . 48

4.2.3 Homoepitaxial phase diagrams by the Monte-Carlo approach . . . 50

4.3 Sample structure and growth conditions . . . . . 55

4.4 Pseudo-homoepitaxial growth of AlN . . . . . 56

4.5 Conclusion . . . . . 60

**5 Desorption induced GaN quantum dot growth 61**
5.1 Sample structure and growth conditions . . . . . 63
5.2 Morphological results of uncapped samples . . . . . 64
5.2.1 Influence of growth interruption time . . . . . 64
5.2.2 Influence of temperature . . . . . 66
5.3 Optical properties of capped samples . . . . . 68
5.4 Conclusion . . . . . 71

**6 Surface energy induced 2D to 3D transition in GaN 73**
6.1 Review of GaN quantum dot epitaxy . . . . . 75
6.2 Qualitative heteroepitaxial growth model . . . . . 77
6.2.1 Heteroepitaxial growth as a function of strain . . . . . 78
6.2.2 Heteroepitaxial growth as a function of surface energy . . . . . 81
6.3 Sample structure and growth conditions . . . . . 83
6.4 Morphological results of uncapped samples . . . . . 84
6.4.1 High V/III ratio – 2D growth . . . . . 84
6.4.2 Influence of V/III ratio – 2D/3D transition . . . . . 85
6.4.3 Low V/III ratio – 2D/3D transition . . . . . 86
6.4.4 Analysis of the wetting layer thickness . . . . . 88
6.4.5 Surface energy balance . . . . . 92
6.5 Optical properties of capped samples . . . . . 95
6.6 Conclusion . . . . . 99

**7 Conclusion and outlook 101**
7.1 Conclusion . . . . . 101
7.2 Outlook . . . . . 102

**Bibliography 105**

**List of publications 123**

**List of figures 127**

**List of growth samples 129**

**Acknowledgments 131**

# 1 Introduction

GaN quantum dots embedded in AlN are very promising candidates for future monolithic quantum-devices [1–3] emitting single or entangled photons on demand at room temperature [4, 5]. Already in 1982, Arakawa and Sakaki [6] proposed the exceptional optoelectronic properties of such zero-dimensional structures. When embedding a nanosized low-bandgap material inside a matrix of high-bandgap material, an energy confinement in all three dimensions can yield individual energy levels with a delta-like density of states similar to single isolated atoms [7]. Therefore, quantum dots are often called artificial atoms even though a single quantum dot consist of more than $10^4$ atoms. Such a solid-state system can be quantum-mechanically tailored to access novel physics of an upcoming quantum age employing quantum computation [8–11] and quantum cryptography [12–14]. In general, optoelectronic devices based on quantum dots have already been proven to be very efficient candidates for engineered photon emission [15–17]. However, they operate at cryogenic temperatures.

Group-III nitrides are wide bandgap materials, which have just recently been honored with the Nobel Prize in 2014 [18] for Isamu Akasaki [19], Hiroshi Amano [19], and Shuji Nakamura [20, 21]. Besides the achieviements in the visible spectrum with light emitting diodes and laser diodes, other very promising applications such as ultraviolet light emitting diodes [22–24], high-temperature, and high-power electronics [25, 26] can be realized with group-III nitrides. In contrast to established material systems like arsenides and phosphides, the exceptional large bandgap difference between GaN and AlN of 2.6 eV can provide superior exciton confinement for energy separation of distinct excitonic eigenstates larger than 25 meV, which is required for room temperature applications. E.g. the biexciton binding energy, one natural limitation factor for pure single photon emission,

can be tuned up to 30 meV by tailoring the quantum dot structure [27–31]. Despite those excellent optical properties, synthesizing high quality GaN quantum dots is still very challenging. Several techniques have been reported to realize GaN quantum dots by bottom-up approaches. In 1996, Tanaka et al. [32, 33] used silicon to partially mask the surface for selective area nucleation of GaN quantum dots on AlGaN. However, it appears that the silicon prevents good optical properties [34, 35]. Other uncommon techniques are vapor-liquid-solid epitaxy [36], droplet-epitaxy [37, 38], atomic layer deposition [39], and even thickness fluctuations inside quantum wells [40]. Commonly, quantum dots are synthesized by Stranski-Krastanow heteroepitaxial growth, which yields self-assembled coherently strained islands on a wetting layer. For other material systems, this approach has been proven to provide defect-free quantum dot structures with excellent optical properties [15–17]. Stranski-Krastanow growth depends on an energy balance between the surface energy and the strain energy. For a large number of material systems, Stranski-Krastanow growth is observed at a minimum lattice mismatch of about $\epsilon = 2.5\%$ [41, 42], which is close to the lateral lattice mismatch between GaN and AlN with $\epsilon_{\mathrm{GaN/AlN}} = 2.4\%$. Consequently, the growth of GaN on AlN is very sensitive to changes of the surface energy.

Daudin et al. [43–46] reported Stranski-Krastanow GaN quantum dots on AlN by plasma-assisted molecular beam epitaxy under nitrogen-rich growth conditions. Furthermore, GaN quantum dots could be realized by employing a Ga bilayer under gallium-rich growth conditions followed by a growth interruption [47–53]. For ammonia-assisted molecular beam epitaxy, quantum dot formation was reported in a similar manner [31, 54–57]. The quantum dot formation could be achieved by an advanced growth interruption right after the GaN deposition. In molecular beam epitaxy with an ultra-high vacuum, the feasibility of reflection high-energy electron diffraction allows monitoring in-situ the island formation on a nanoscale, which is a big advantage over metalorganic vapor-phase epitaxy. Consequently, studying quantum dot formation appears to be more challenging for metalorganic vapor-phase epitaxy. However, metalorganic vapor-phase epitaxy provides high scalability for commercial mass production of optoelectronic devices. Two major approaches have been reported so far. An island formation introduced by a growth interruption after the growth of a two-dimensional GaN layer [58, 59] or the use of a very low V/III ratio [60–65]. As pointed out, GaN nucleation is very sensitive to surface energy and strain energy fluctuations. A favored GaN nucleation has been reported at step-bunches [31, 66–68] and threading dislocations [69–71]. Therefore, smooth AlN substrates are mandatory for Stranski-Krastanow quantum dot growth.

The aim of this thesis is to establish GaN quantum dots on AlN substrates by metalorganic vapor-phase epitaxy and to provide further insights to homoepitaxial and heteroepitaxial growth processes. At first, basic principles for epitaxy of group-III nitride semiconductors are presented in Chapter 2. This includes structural properties of the material system, optoelectronic properties of a GaN/AlN quantum dot heterostructure, and the epitaxial growth process. In Chapter 3, the primary experimental methods are described, which are metalorganic vapor-phase epitaxy for sample synthesis, atomic force microscopy for surface morphology characterization, electron beam lithography to process mesa structures, and micro photoluminescence for optical investigations. In Chapter 4, achieving smooth AlN surfaces on AlN templates with step-bunches is presented. The homoepitaxial growth transition between step-flow growth and step-bunching growth is theoretically investigated by a surface diffusion model and experimentally confirmed by metalorganic vapor-phase epitaxy. In Chapter 5, GaN quantum dot formation is studied by growing a two-dimensional GaN layer with a high V/III ratio followed by a growth interruption of different durations at various temperatures. Additionally, optical properties of capped samples are presented to demonstrate typical optical features of GaN quantum dots. In Chapter 6, Stranski-Krastanow GaN quantum dots are achieved by analyzing the impact of the surface energy on the heteroepitaxial growth transition between two-dimensional Frank-van-der-Merve growth and three-dimensional Stranski-Krastanow growth. First, the impact of the surface energy on the heteroepitaxial growth transition is qualitatively discussed by an empirically motivated growth model. Then, different growth modes are experimentally studied by controlling the V/III ratio in metalorganic vapor-phase epitaxy. In order to confirm the Stranski-Krastanow growth mode, detailed investigations of the wetting layer thickness as well as the side facets of the GaN quantum dots are presented. Again, optical properties of capped samples exhibit typical GaN quantum dot features. A final conclusion is presented in Chapter 7 and an outlook for future work is proposed.

# 2 Basic principles of group-III nitride epitaxy

Group-III nitrides are a remarkable material system [18] with a superior wide bandgap range of up to 6.0 eV at room temperature [72] and the feasibility of doping [19–21] enabling optoelectronic devices for exceptional applications. Besides the single and entangled photon generation at room temperature, other very promising group-III nitride based applications are hot research topics such as UV-LEDs [22–24], high-temperature, high-power electronics [25, 26], and highly-specialized optoelectronic devices for space operations [73–75].

In this chapter, basic principles of the group-III nitrides for this thesis will be presented. It starts with the structural properties of the wurtzite crystal, which define most of the underlying physical processes. Epitaxial growth proceeds at the vapor-solid interface of the semiconductor. Therefore, the impact of the surface during epitaxy is discussed by the use of two classic surface reconstructions. After exhibiting their structural properties, the correlation between the vapor-phase conditions and the occurrence of the surface reconstruction is explained. Then, the optoelectronic properties of a GaN/AlN quantum dot heterostructure is presented. Being fundamental for epitaxial growth, the macroscopic surface with vicinal terraces is defined. Additionally, the microscopic surface is expressed by a surface potential with energy barriers for adatom diffusion. Adatom kinetics are illustrated by a typical model for layer-by-layer growth, the terrace ledge kink model. Finally, different growth morphologies are introduced in general for homoepitaxial and heteroepitaxial growth, which are both explored in this thesis for AlN and GaN on AlN, respectively.

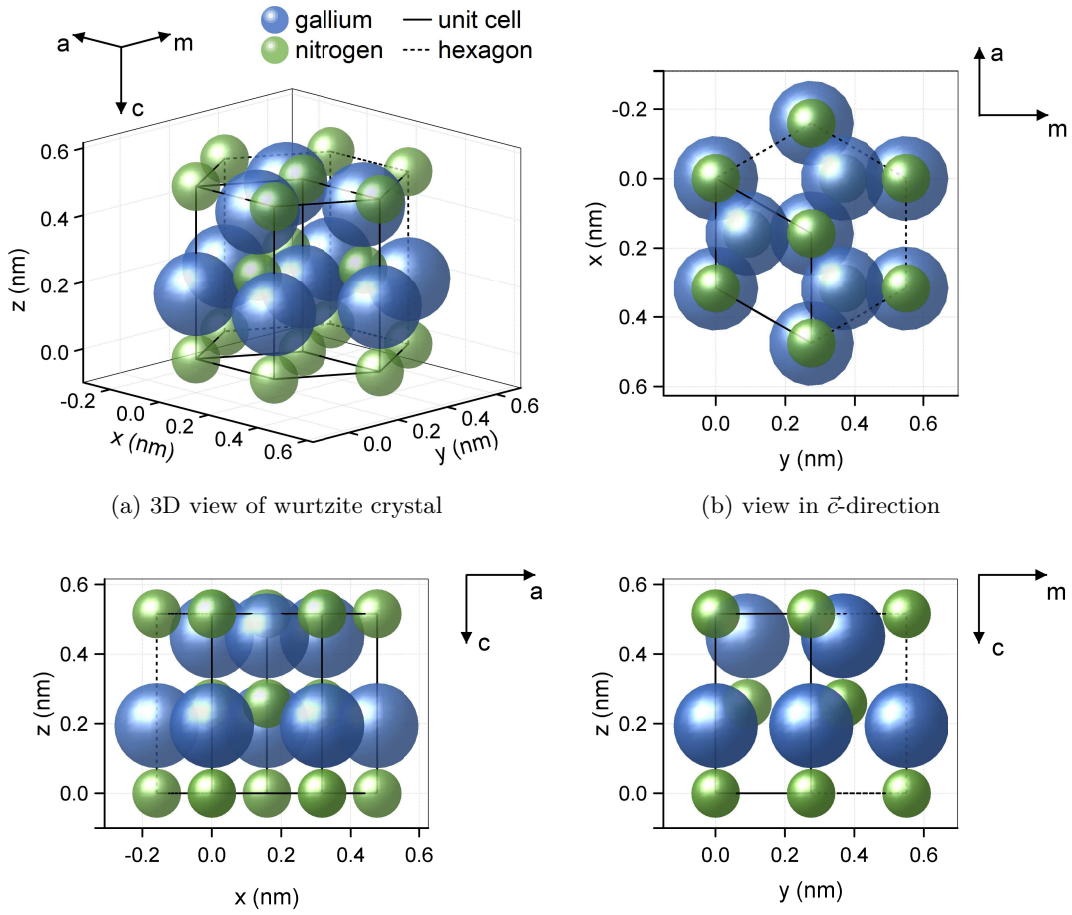


(a) 3D view of wurtzite crystal

(b) view in $\vec{c}$-direction

(c) view in $\vec{m}$-direction

(d) view in $\vec{a}$-direction

Figure 2.1: Schematic structure of the wurtzite crystal on the example of GaN. The diameters represent the covalent radii of nitrogen with $r_{\mathrm{N}} = 0.074\,\mathrm{nm}$ and gallium with $r_{\mathrm{Ga}} = 0.126\,\mathrm{nm}$ [76].

## 2.1 Fundamental properties of group-III nitrides

### 2.1.1 Bulk crystal

The thermodynamically most favored crystal structure of group-III nitride semiconductors is the wurtzite structure [77, 78]. Figure 2.1 exhibits the atomic arrangement of GaN with gallium atoms (big blue spheres) and nitrogen atoms (small green spheres) inside the primitive unit cell (solid lines) and a hexagonal unit cell (dashed lines). The wurtzite structure can be described by a hexagonal closed package with a basis containing two atoms, one gallium and one nitrogen atom, to emphasize the symmetrical properties. A common property of the wurtzite structure, the large ionic character of the covalent

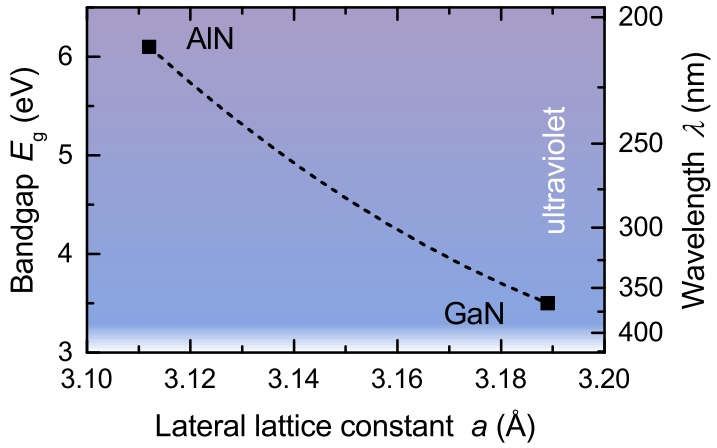


Figure 2.2: Energy bandgap $E_g$ and lateral lattice constant $a$ of the binary compounds AlN and GaN marked with solid squares and the ternary alloy of AlGaN with a dashed line.

bonds, is expressed by the difference of the electronegativity of the nitrogen and gallium atom $\chi(\mathrm{N}) - \chi(\mathrm{Ga}) = 1.4$ [76]. According to Pauling's method [76] the ionic character $p$ of a polar covalent bond can be estimated by an empirical equation:

$$p(\mathrm{GaN}) = 16\% \, |\chi(\mathrm{N}) - \chi(\mathrm{Ga})| + 3.5\% \, |\chi(\mathrm{N}) - \chi(\mathrm{Ga})|^2 \quad \approx \quad 30\%$$

This large dipole between the nitrogen and the gallium atoms favors the wurtzite structure [77, 78]. Furthermore, the very large internal polarization for group-III nitrides leads to huge sheet charges at heterointerfaces [79]. One advantage of the sheet charges is a potential generation of a two-dimensional electron-gas. However, for optical applications, additional sheet charges are often unwanted due to the many negative effects of the quantum-confined Stark effect (Chapter 2.1.4).

Figure 2.2 exhibits a diagram with the energy bandgap $E_g$ and the lateral lattice constant $a$ of the binary compounds AlN and GaN. Both binary materials offer exceptionally large bandgap energies of 6.1 eV for AlN and 3.5 eV for GaN at $T$=15 K [72], which enable superior optoelectronic devices in the ultraviolet spectral range. A heterostructure based on both materials can offer very high confinement energies for electrons and holes enabling well isolated energy levels with delta-like density of states, which is explained in Chapter 2.1.4. Important for epitaxial growth, the difference of the lateral lattice constants with $a_{\mathrm{AlN}} = 0.3112\,\mathrm{nm}$ and $a_{\mathrm{GaN}} = 0.3189\,\mathrm{nm}$ at room temperature [80, 81] introduces biaxial strain. This is a key parameter for heteroepitaxial growth modes, which is explained in Chapter 2.2.5.

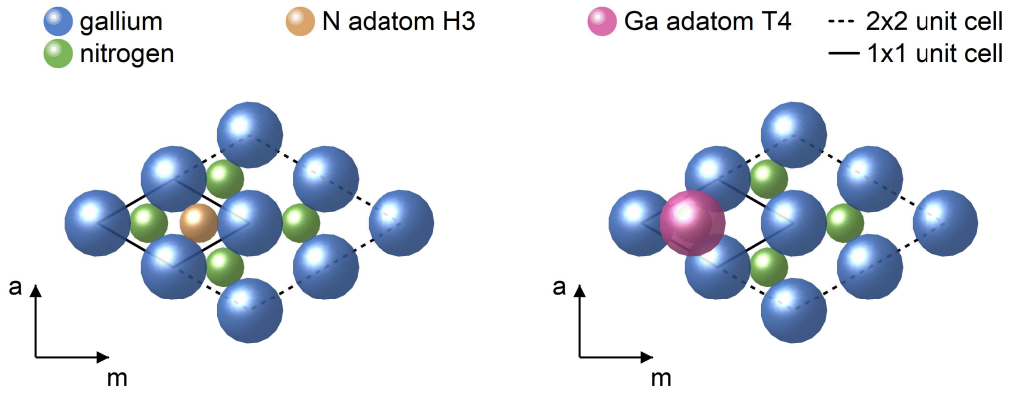


(a) 2x2 N adatom at H3 position

(b) 2x2 Ga adatom at T4 position

Figure 2.3: 2x2 unit cell of two major surface reconstructions based on Northrup et al. [82, 83].

### 2.1.2 Surface reconstruction

The energetically favored c-plane [84] is commonly used for epitaxial growth with growth along the $\vec{c}$-direction. The top-most monolayer at the surface is sketched in Fig. 2.3 with gallium atoms in blue and nitrogen atoms in green. The distance between stable monolayers is half of the lattice unit, which is $\frac{c_{\mathrm{AlN}}}{2} = 0.249\,\mathrm{nm}$ for AlN and $\frac{c_{\mathrm{GaN}}}{2} = 0.259\,\mathrm{nm}$ for GaN [80, 81]. At the vapor-solid interface, a surface reconstruction minimizes the surface energy. Depending on the vapor-phase conditions, a metal-rich surface reconstruction for high metal partial pressures or a nitrogen-rich reconstruction for high nitrogen partial pressures can be expected [82, 83]. Metalorganic vapor-phase epitaxy contains large numbers of vapor species, which can form even more complicated surface reconstructions [85–89]. Due to the lack of explicit knowledge, the discussion of the impact of different surface reconstructions is kept to two rather simple surface reconstruction: a nitrogen-terminated 2x2 surface reconstruction with a nitrogen atom at the H3 position in the top-most layer (sketched yellow in Fig. 2.3a), and a metal-terminated 2x2 surface reconstruction with a metal atom at the T4 position in the top most layer (sketched magenta in Fig. 2.3b).

### 2.1.3 Surface energy

Epitaxial growth relies on self-assembled atomic arrangements. One of the main driving forces is the surface energy depending on the surface reconstruction. Additionally, the correlated surface potential has an influence on the adatom kinetics with adatom diffusion

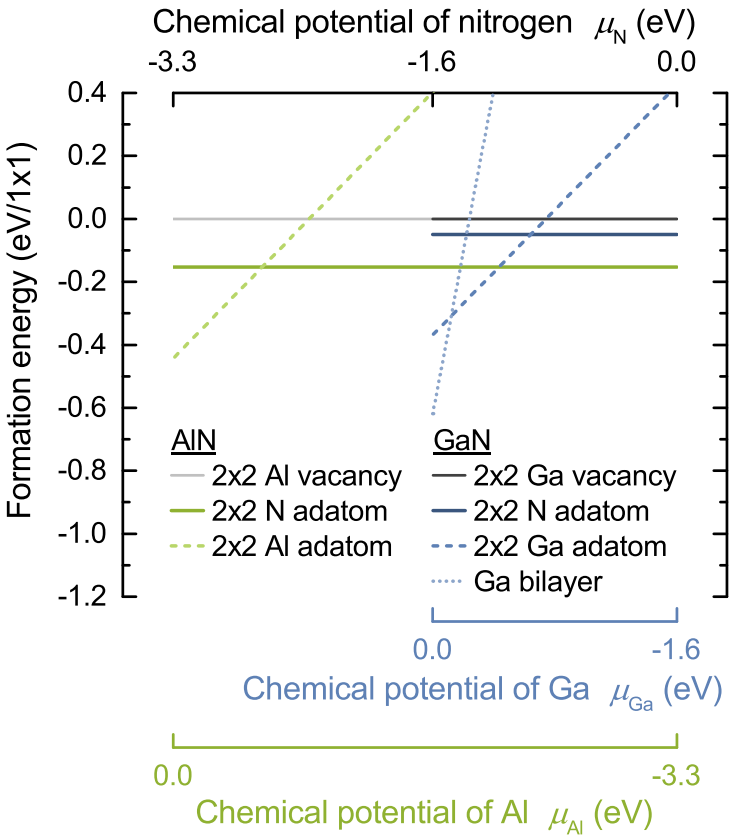


Figure 2.4: Relative formation energies at equilibrium of different surface reconstructions of AlN (green) and GaN (blue) taken from Northrup et al. [82, 83]. The chemical potential of bulk is $\mu_{\mathrm{III(bulk)}} \equiv 0$.

energy barriers (Chapter 2.2.2). Theoretically, the surface energy $\gamma$ can be calculated by density functional theory for various surface reconstructions. One key problem is to consider a complete set of surface reconstructions to ensure the thermodynamically most favored surface reconstruction at different vapor-phase conditions. By combining experimental observations and theoretical calculations a good estimation can be achieved for molecular beam epitaxy [90, 91]. For metalorganic vapor-phase epitaxy the situation is much more complicated due to additional vapor-phase species [85–89]. Lacking explicit knowledge, the discussion will be kept to two rather simple surface reconstructions. Northrup et al. have calculated formation energies for different surface reconstructions of AlN [82] and GaN [83, 90] as a function of the chemical potential of the group-III element. Thermodynamically favored surface reconstructions with the lowest formation energies are plotted in Fig. 2.4 and correlated with the chemical potentials of the group-III element. The chemical potential of the group-III element is set to zero $\mu_{\mathrm{III(bulk)}} \equiv 0$ for metallic Al or Ga. For atomic nitrogen, the chemical potential must remain below zero $\mu_N < 0$. The formation energy of the nitride compound $E\,(\mathrm{AlN_{bulk}/GaN_{bulk}})$ is the sum of the

chemical potentials of the educts [82, 92]:

$$\begin{aligned} \mu_{\mathrm{Al}} + \mu_{\mathrm{N}} &= 2E\left(\mathrm{AlN_{bulk}}\right) \\ \mu_{\mathrm{Ga}} + \mu_{\mathrm{N}} &= 2E\left(\mathrm{GaN_{bulk}}\right) \end{aligned} \tag{2.1}$$

This leads to the lower boundary of the chemical potential of the group-III elements:

$$\begin{aligned} \Delta H_{\mathrm{AlN}} &= E\left(\mathrm{Al_{metal}}\right) + E\left(\mathrm{N_2}\right) - 2E\left(\mathrm{AlN_{bulk}}\right) \\ &= -2E\left(\mathrm{AlN_{bulk}}\right) \end{aligned} \tag{2.2}$$

$$\begin{aligned} \Delta H_{\mathrm{GaN}} &= E\left(\mathrm{Ga_{metal}}\right) + E\left(\mathrm{N_2}\right) - 2E\left(\mathrm{GaN_{bulk}}\right) \\ &= -2E\left(\mathrm{GaN_{bulk}}\right) \end{aligned} \tag{2.3}$$

with the standard enthalpy of formation $\Delta H$ and the formation energies of pure elements defined as zero $E\left(\mathrm{N_2}\right) = E\left(\mathrm{Al_{metal}}\right) = E\left(\mathrm{Ga_{metal}}\right) \equiv 0$. This determines the lower boundary for AlN to $\mu_{\mathrm{Almin}} = -\Delta H_{\mathrm{AlN}} = -3.3\,\mathrm{eV}$ [82, 93] and for GaN to $\mu_{\mathrm{Gamin}} = -\Delta H_{\mathrm{GaN}} = -1.6\,\mathrm{eV}$ [94–96]. In equilibrium, both chemical potentials of the group-III element and the nitrogen are related by Eq. 2.1. As seen in Fig. 2.4, a change of the chemical potential of nitrogen will change the surface reconstruction. Each surface reconstruction provides different surface diffusion channels for adatoms, which corresponds to specific diffusion coefficients. High diffusion coefficients are obtained for metal-rich reconstructions and low diffusion coefficients are obtained for nitrogen-rich reconstructions, which is both the case for GaN [97] and AlN [98].

For an ideal gas, the chemical potential $\mu_i$ can be described as a function of the partial pressure $p_i$ [99] by

$$\mu_i = \mu_i^{\circ}\left(T\right) + RT \ln\left(\frac{p_i}{p_0}\right) \tag{2.4}$$

with the gas constant $R$, the temperature $T$, a reference pressure $p_0$, and a reference chemical potential $\mu_i^{\circ}$, which are both typically chosen at standard conditions. For metalorganic vapor-phase epitaxy, the growth is often limited by the group-III element. Therefore, a change of the group-III supply is accompanied with a change of the growth rate. In order to control the surface kinetics independent of the growth rate, the nitrogen supply is varied at constant group-III supply. The chemical potential of nitrogen $\mu_{\mathrm{N}}$ during growth is controlled by the nitrogen partial pressure $p_{\mathrm{N}}$ with

$$\mu_{\mathrm{N}} = \mu_{\mathrm{N}}^{\circ}\left(T\right) + RT \ln\left(p_{\mathrm{N}}\right) \tag{2.5}$$

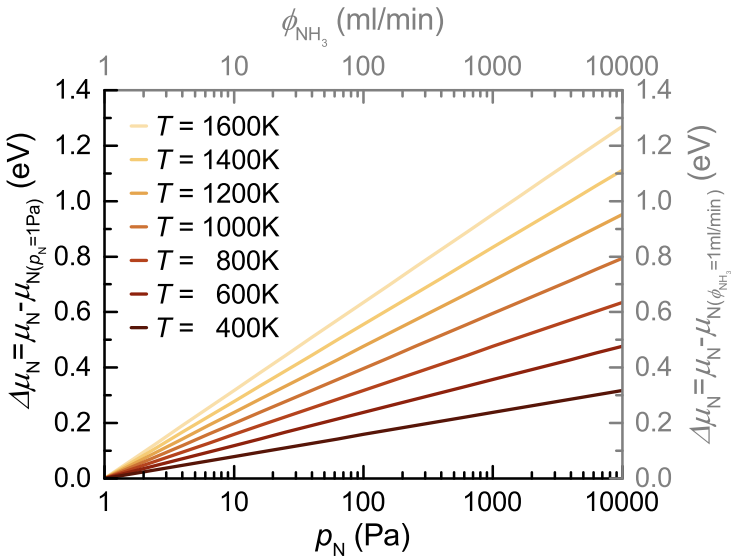


Figure 2.5: The change of the chemical potential of nitrogen $\Delta\mu_N$ as a function of the partial pressure of nitrogen $p_N$ (black axes), or as a function of the ammonia flow rate $\phi_{NH_3}$ (gray axes). Different colors correspond to different temperatures $T$.

with an arbitrary reference chemical potential of nitrogen $\mu_N^\circ$. Figure 2.5 exhibits the change of the chemical potential $\Delta\mu_N$ as a function of the temperature and the partial pressure of nitrogen (bottom, black axis). For a growth temperature of AlN with about 1400 K, a change of the nitrogen partial pressure of two orders of magnitude yields a change of the chemical potential of $\Delta\mu_N = 0.55\,\text{eV}$. For GaN with a lower growth temperature of about 1000 K, the chemical potential can be changed by $\Delta\mu_N = 0.4\,\text{eV}$ for a change of the nitrogen partial pressure by two orders of magnitude.

For metalorganic vapor-phase epitaxy, the partial pressure of nitrogen $p_N$ is provided by ammonia, which dissociates only partially even at elevated growth temperatures of 1200 K [100, 101]. By assuming such a partial pyrolysis, the nitrogen partial pressure is related to the ammonia partial pressure by

$$p_N = r_{NH_3} \cdot p_{NH_3} \tag{2.6}$$

with a temperature dependent decomposition ratio of ammonia $r_{NH_3}$. By inserting Eq. (2.6) into Eq.(2.5), the change of the chemical potential of nitrogen $\mu_N$ is related to the partial pressure of ammonia $p_{NH_3}$

$$\begin{aligned} \mu_N &= \mu_N^\circ(T) + RT \ln\left(r_{NH_3} \cdot p_{NH_3}\right) \\ &= \mu_{NH_3}^\circ(T) + RT \ln\left(p_{NH_3}\right) \end{aligned} \tag{2.7}$$

with a different reference chemical potential of ammonia $\mu_{NH_3}^\circ$. A similar discussion

can be made about the volume flow rate of ammonia $\phi_{NH_3}$ ($\phi_{NH_3} \sim p_{NH_3}$). Figure 2.5 shows the correlation between the change of the chemical potential of nitrogen and the volume flow rate of ammonia (top, gray axis) at different temperatures. By changing the volume flow rate of ammonia $\phi_{NH_3}$ by two orders of magnitude at a temperature of 1000 K or 1400 K, the chemical potential of nitrogen can be changed by $\Delta\mu_N = 0.4\,\text{eV}$ or $\Delta\mu_N = 0.55\,\text{eV}$, respectively.

In conclusion, a high partial pressure of ammonia $p_{NH_3}$ is related to a high chemical potential of nitrogen $\mu_N$, which can yield a nitrogen-terminated surface reconstruction and, therefore, high surface energies $\gamma$ with a low surface diffusivity $D_s$:

$$p_{NH_3} \uparrow \quad \curvearrowright \quad \mu_N \uparrow \quad \curvearrowright \quad \gamma \uparrow,\ D_s \downarrow \tag{2.8}$$

### 2.1.4 Optical properties of GaN quantum dots

Semiconductor quantum dot structures exhibit distinct energy levels for electrons and holes, which are very similar to energy levels in single isolated atoms. This is achieved by proper electron and hole confinement in all three dimensions with a low-bandgap material embedded in a high-bandgap matrix material. A large band offset provides a large energy space for the separation of the individual energy levels. Additionally, the structure size of a quantum dot has to be in the range of the de-Broglie wavelength of electrons and holes in all three dimensions. A simple rule of thumb is to look for the exciton diameter, which is about 5 nm for GaN. Due to the growth process, epitaxial quantum dots are typically very flat with small aspect ratios of $0.2 \pm 0.1$ [50,60]. Therefore, the optical properties are mainly defined by the vertical confinement. Unique for group-III nitrides is the internal polarization, which results in huge interface sheet charges $\pm\sigma_{pol}$ at the heterointerfaces. A band diagram of a GaN quantum dot inside an AlN matrix is sketched on the left side of Fig. 2.6 with the conduction band $E_C$ for electrons and the valence band $E_V$ for holes. The change of the internal polarization fields at the interfaces introduces a band bending by interface sheet charges $\pm\sigma_{pol}$. The optical transition is characterized by the quantum-confined Stark effect, which describes the electron and hole confinement inside an electric field. Depending on the structure size, transition energies for GaN quantum dots of 2 – 5 eV are reported [31,45,54,60]. As shown in Fig. 2.6, the internal electric field yields a large spacial separation of the electron and hole wave functions ($\Phi_{e^-}$, $\Phi_{h^+}$) along the $\vec{c}$-direction, which reduces the radiative recombination rate [102–104] and generates a large dipole moment of the exciton $\vec{\mu}_{he}$. This dipole makes excitons very sensitive to

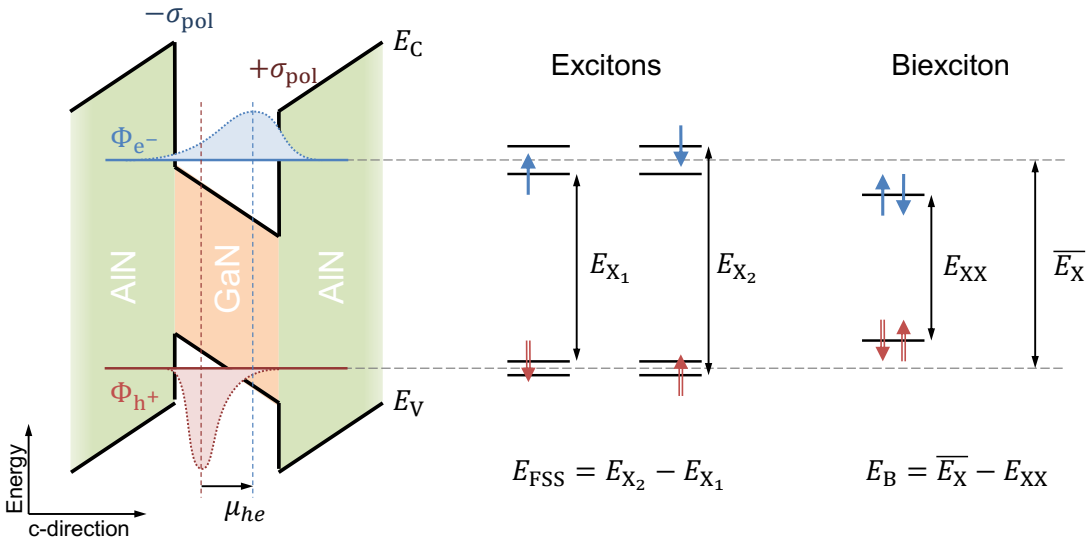


Figure 2.6: On the left side, a schematic energy band diagram of the GaN/AlN-heterostructure in the polar growth direction ($\vec{c} = [0001]$) with the polarization-induced interface sheet-charges ($-\sigma_{pol}$, $+\sigma_{pol}$) resulting in the quantum-confined Stark effect. The separation of the electron and hole wave function ($\Phi_{e^-}$, $\Phi_{h^+}$) yield a large dipole moment of the exciton $\vec{\mu}_{he}$. On the right side, the different energy levels exhibit the two orthogonal excitons ($E_{X_1} = |\uparrow\Downarrow\rangle$, $E_{X_2} = |\downarrow\Uparrow\rangle$) separated by fine-structure splitting $E_{FSS}$, and the biexciton ($E_{XX} = |\uparrow\downarrow\Uparrow\Downarrow\rangle$). The arrows represent different spin configurations.

surrounding electric charges, which are the origin of spectral diffusion [104–106] increasing the line-width by several meV. The lateral structure of the quantum dot defines the fine-structure splitting, which is related to the exchange interaction and is very sensitive to quantum dot elongation [104, 107, 108]. Ideal symmetric quantum dots could offer zero fine-structure splitting necessary for entangled photon sources [104]. The polarization of exciton transitions separated by fine-structure splitting is orthogonal to each other. Additionally, biexcitons can be formed at high optical excitation power with a population scaling approximately quadratically with the excitation power [105, 109] in contrast to the linear dependency for excitons. Again, the optical properties of biexcitons are highly correlated with the lateral size of a quantum dot [104]. On one hand, GaN quantum dots with very low aspect ratios and large lateral sizes provide enough space to obtain holes with the same spin state [104]. This can result in large biexciton binding energies $E_B$ up to 30 meV. On the other hand, GaN quantum dots with large aspect ratios and small lateral sizes exhibit biexciton binding energies down to $E_B = -50$ meV. Additionally, the polarization properties are highly influenced by the spin configuration. For small quantum dots with intermediate aspect ratios of about 0.2, the exciton and biexciton transitions are parallel polarized with a positive biexciton binding energy $E_B > 0$ [104].

If the aspect ratio gets smaller, the biexciton can still be positive, however, both holes may share the same spin, which results in a more complicated decay process involving dark-exciton states [104].

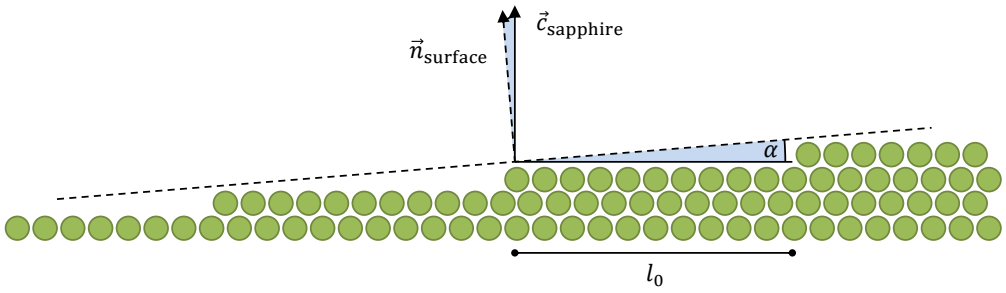


Figure 2.7: Schematic picture of the substrate offcut angle $\alpha$ between the crystal orientation $\vec{c}_{\text{sapphire}}$ and the macroscopic surface $\vec{n}_{\text{surface}}$.

## 2.2 Epitaxial layer growth

### 2.2.1 Substrate offcut providing vicinal terraces

For epitaxy, layer-by-layer growth is typically favored to maintain smooth surfaces. In order to control nucleation conditions, an offcut between the macroscopic surface $\vec{n}_{\text{surface}}$ and the crystal orientation $\vec{c}_{\text{sapphire}}$ of the basal planes is induced by a substrate offcut angle $\alpha$. Consequently, vicinal terraces on the surface are formed, which are sketched in Fig. 2.7. A simple relation of the substrate offcut angle $\alpha$ and the terrace width $l_0$ can be expressed by

$$\begin{aligned} 1\,\text{ML} &= l_0 \tan\alpha \\ l_0 &\approx 14\,\text{nm} \cdot \frac{1^\circ}{\alpha_{Al_2O_3}}. \end{aligned} \tag{2.9}$$

Large offcuts result in narrow vicinal terrace widths and vice versa. The substrate offcut angle can be determined by X-ray diffraction after adjusting the macroscopic surface with a laser pointer.

Typically, very small offcut angles with $\alpha < 1^\circ$ are implemented to preserve the main crystal plane properties of the crystal orientation. A layer-by-layer growth is maintained, if all adatoms are able to diffuse to one of the terrace steps for incorporation. This will lead to an infinite lateral growth in only one direction (to the left in Fig. 2.7) preventing the formation of grain boundaries. If the adatom diffusion length is much shorter than the terrace width, two-dimensional island nucleation can occur, which may lead to island growth. In this case, smooth layer-by-layer growth may be preserved for larger substrate offcut angles with narrow terrace widths.

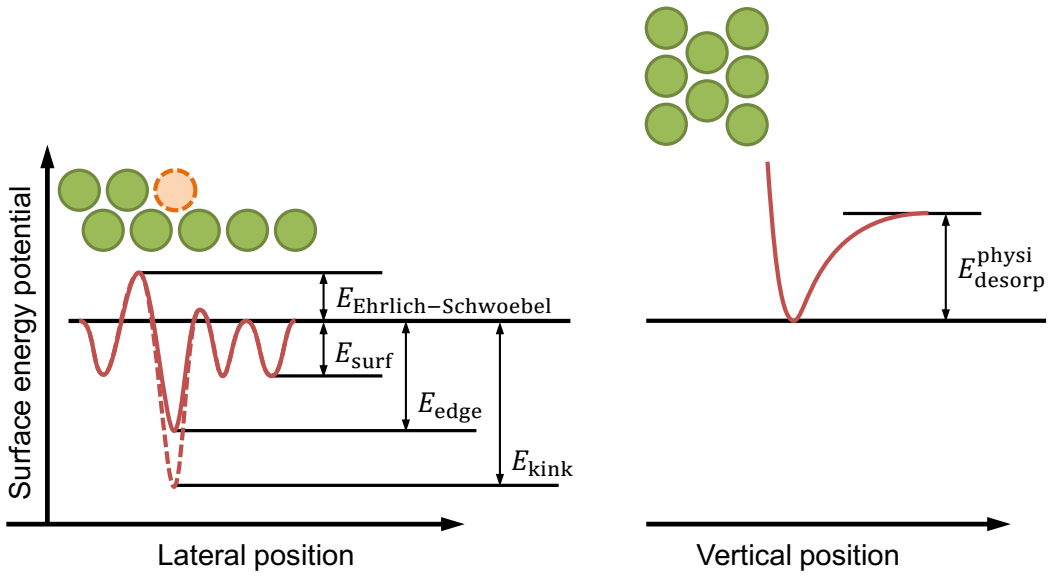


(a) Lateral surface energy potential for chemisorbed adatoms.

(b) Vertical surface energy potential for physisorbed adatoms.

Figure 2.8: (a) Lateral and (b) vertical cross section of a surface are sketched by green circles. Dashed orange circle represents prominent incorporation positions for adatoms. The surface potential is sketched in red as a function of adatom position with participating activation energies.

### 2.2.2 Surface energy potential for adatom kinetics

In a kinetic description, adatom diffusion on a surface is characterized by the surface energy potential. It is defined by local energy maxima and minima. A simplified schematic diagram of the one-dimensional surface energy potential is shown in Fig. 2.8. The activation energy $E_{\text{A}}$ for adatom hopping between two adjacent energetically stable positions determines the hopping rate constant $k$ for adatoms

$$k \sim \exp\left(-\frac{E_{\text{A}}}{\text{k}_{\text{B}}T}\right) \tag{2.10}$$

at the temperature $T$ and with the Boltzmann constant $\text{k}_{\text{B}}$. Possible activation energies for chemisorbed adatoms are a diffusion barrier $E_{\text{surf}}$, an incorporation energy at the edge $E_{\text{edge}}$, or an incorporation energy at the kink position $E_{\text{kink}}$ (Chapter 2.2.3). The Lennard-Jones potential describes adatoms, which are physisorbed in the vertical direction mainly influenced by the Born and van-der-Waals interaction (Fig. 2.8b). For chemisorbed adatoms, additional covalent bonds have to be considered. For a one-dimensional case, a perfect crystal plane is simplified to a surface diffusion energy barrier $E_{\text{surf}}$, between which adatoms have a favored position with covalent bonds (Fig. 2.8a). This may be more

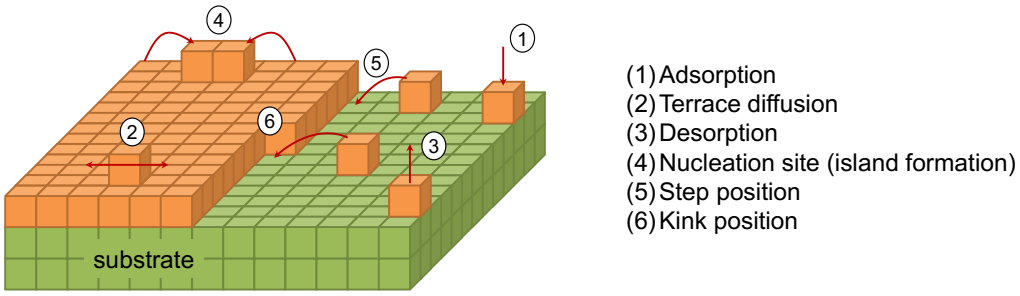


Figure 2.9: Simplified schematic diagram of the very complex adatom kinetics on a surface

complicated for anisotropic crystals. Additionally, a surface reconstruction influences the surface diffusion channel as discussed for AlN and GaN in Chapter 2.1.3. At terrace steps, additional covalent bonds can be made at the edge and kink position, which are characterized by $E_{\text{edge}}$ and $E_{\text{kink}}$, respectively. Furthermore, the surface reconstruction is disturbed at the step edge introducing additional energy barriers. The energy barrier from the upper terrace to the incorporation position is called Ehrlich-Schwoebel barrier $E_{\text{Ehrlich-Schwoebel}}$. This can be attractive or repulsive yielding inverse or positive energies. A positive or inverse $E_{\text{Ehrlich-Schwoebel}}$ is the origin of step-flow growth and step-bunching growth [110, 111], respectively. Further details are presented in Chapter 4.1.

### 2.2.3 Terrace ledge kink model

Epitaxial growth can be described by thermodynamical or kinetic models. Because epitaxial growth proceeds in general far from equilibrium, a kinetic theory offers a straightforward description of underling chemical processes. Adatom kinetics on the surface play the key role and depend on the surface energy potential (Chapter 2.2.2). The terrace ledge kink model was originally defined for cubic systems and can be generalized for any lattice configuration. Six different cases for adatom movement can be distinguished as illustrated in Fig. 2.9. At first, layer growth is provided by atoms from the vapor-phase adsorbing on the surface (Fig. 2.9(1)). For the second case, adatoms diffuse on the surface (Fig. 2.9(2)). In a simplified picture, they have to split surface bonds and regenerate them at an adjacent position, which requires an activation energy $E_{\text{surf}}$. This hopping process is described by a hopping rate. For surface diffusion, this hopping rate is called diffusivity or simply diffusion coefficient $D_{\text{s}}$:

$$D_{\text{s}} \sim \exp\left(-\frac{E_{\text{surf}}}{\text{k}_{\text{B}}T}\right), \tag{2.11}$$

with the temperature $T$ and the Boltzmann constant $k_B$. The diffusivity highly depends on the surface reconstruction by offering adatoms different diffusion channels.

The third case is adatom desorption, where adatoms leave the surface into the vapor-phase (Fig. 2.9(3)). In this case, all atomic bonds have to be broken. Therefore, the activation energy for desorption $E_{\mathrm{desorp}}$ is typically much higher than $E_{\mathrm{surf}}$. The desorption rate $C_s$ can be described by an adatom mean resident time $\tau_s$ or with the activation energy $E_{\mathrm{desorp}}$:

$$C_s = \frac{1}{\tau_s} \sim \exp\left(-\frac{E_{\mathrm{desorp}}}{k_B T}\right). \tag{2.12}$$

The desorption rate highly depends on the surface reconstruction and its formation energy at different vapor-phase conditions.

In order to calculate exact hopping rates, the constants of proportionality are mostly unknown, but they are on the order of the phonon frequencies [112]. A very suitable quantity to describe many surface processes is the surface diffusion length $\lambda_s$. Its square describes the area on the surface, with which adatoms can interact before they desorb from the surface. By assuming the same hopping frequencies for diffusion and desorption a simple relation can be derived:

$$\begin{aligned} \lambda_s^2 &= \frac{D_s}{C_s} = D_s \tau_s \\ &= a^2 \exp\left(-\frac{E_{\mathrm{surf}} - E_{\mathrm{desorp}}}{k_B T}\right) \end{aligned} \tag{2.13}$$

with a hopping distance $a$, which can be approximated by the lateral lattice constant of the crystal.

If the adatom density on the surface is high enough, adatoms can interact with each other and nucleate new islands (Fig. 2.9(4)). This minimum adatom density is the critical island nucleation density [113]. For the two last considered cases of adatom diffusion processes, a surface with terrace steps is required. This allows adatoms to be incorporated at terrace edges (Fig. 2.9(5)) providing typical layer-by-layer growth. Additionally at edges, adatoms can be pinned at kink positions (Fig. 2.9(6)). At this position, adatoms have no further motional degree of freedom and they become part of the epitaxially grown layer.

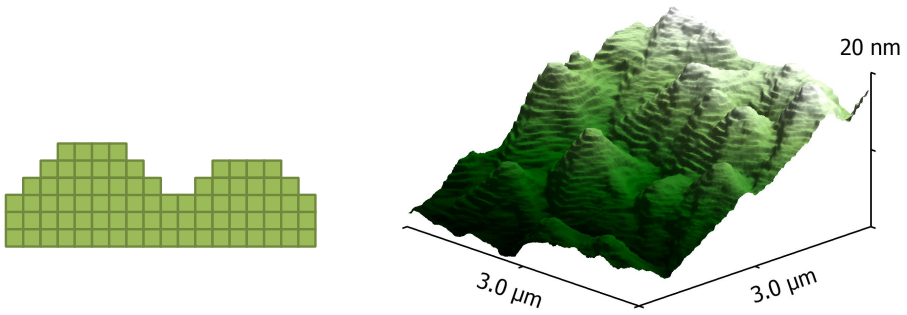

(a) Island growth




(b) Island morphology of grown AlN

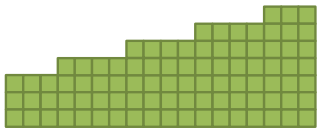

(c) Step-flow growth

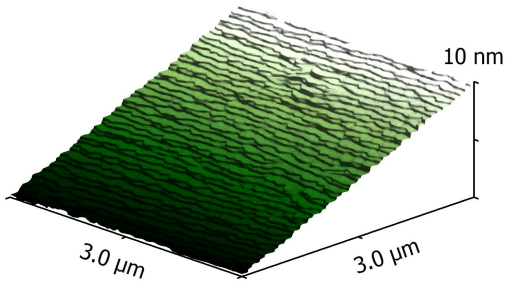


(d) Step-flow morphology of grown AlN

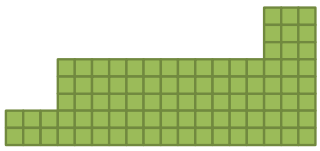

(e) Step-bunching growth

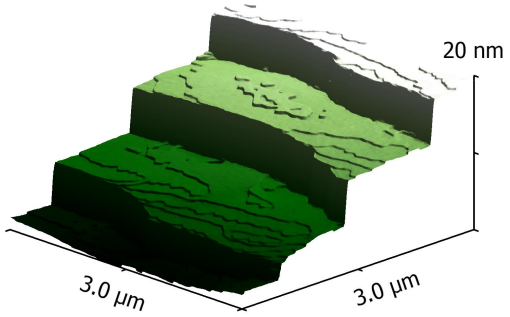


(f) Step-bunching morphology of grown AlN

Figure 2.10: Three major surface morphologies of homoepitaxy.

### 2.2.4 Growth modes in homoepitaxy

Homoepitaxial growth may proceed by either island growth (Fig. 2.10a,b), step-flow growth (Fig. 2.10c,d), or step-bunching growth (Fig. 2.10e,f). The different morphologies can be distinguished by surface diffusion processes, which were established by Burton, Cabrera, and Frank [114] (BCF-theory) in the 1960s. Key parameters are the adatom diffusion length (Chapter 2.2.3), the critical island nucleation density, and the Ehrlich-

Schwoebel barrier (Chapter 2.2.2). If the adatom density is larger than the critical island nucleation density, two-dimensional island nucleation will occur [113] leading to island growth. This is typically obtained at very low growth temperatures with low desorption rates and low adatom diffusivity, or at very high growth rates with very high material supply.

For step-flow growth, the width of vicinal terraces is very important. To maintain a layer-by-layer growth, the adatom diffusion length should be in the order of the terrace width with an adatom density lower than the critical island nucleation density. Due to the terrace steps, adatoms can incorporate from the lower or upper side of the step edge. In general, both incorporation probabilities do not have to be equal. In fact, Ehrlich et al. [115] observed for tungsten an adatom reflection on the upper side of the edge, which could be explained by Schwoebel et al. [110] with an incorporation energy barrier at the upper side of the step edge, the so called Ehrlich-Schoebel barrier (Chapter 2.2.2). If adatoms are mainly incorporated from the lower side, the Ehrlich-Schoebel barrier is positive. This will lead to a self stabilizing growth yielding step-flow growth. If, on the other hand, adatoms are mainly incorporated from the upper side, the Ehrlich-Schoebel barrier is inverse. In this case, large terraces will amplify their growth speed and the growth is unstable yielding step-bunching growth. A detailed investigation by a Monte-Carlo approach and a comparison to experiment is presented in Chapter 4.

### 2.2.5 Growth modes in heteroepitaxy

Heteroepitaxial growth may proceed by either smooth two-dimensional growth (Frank-van-der-Merve, Fig. 2.11a), coherently strained island growth with a wetting layer (Stranski-Krastanow, Fig. 2.11b), or island growth without a wetting layer (Volmer-Weber, Fig. 2.11c) [42, 116]. In contrast to the homoepitaxial growth, a potential lattice mismatch between the two materials introduces strain, which can inhibit the favored layer-by-layer growth. Heteroepitaxial growth is typically associated with biaxial strain, which is caused by matching the lateral lattice constants of the epitaxial grown material to the substrate. For epitaxial growth of GaN on AlN with respective lateral lattice constants of $a_{\mathrm{AlN}} = 0.3112\,\mathrm{nm}$ and $a_{\mathrm{GaN}} = 0.3189\,\mathrm{nm}$ at room temperature [80, 81], a lattice mismatch of $\epsilon_{\mathrm{GaN/AlN}} = \frac{a_{\mathrm{AlN}} - a_{\mathrm{GaN}}}{a_{\mathrm{GaN}}} = -2.4\%$ is obtained. This is close to the minimum lattice mismatch of Stranski-Krastanow growth reported for several material systems [41].

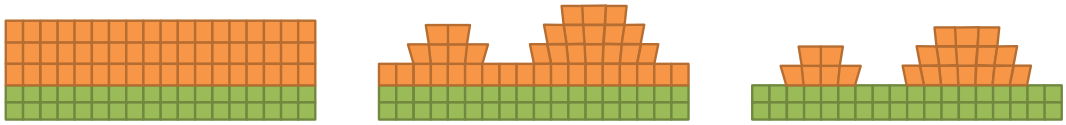

(a) Frank-van-der-Merve (b) Stranski-Krastanow (c) Volmer-Weber

Figure 2.11: Three major surface morphologies of heteroepitaxy.

If the strain energy is rather small compared to the surface energy, the system may proceed by two-dimensional layer-by-layer growth. Eventually, the accumulated strain energy is relieved by defect formation. If the strain energy is on the order of the surface energy or the projected surface energy density of side facets is much lower than the surface energy density of the basal plane, Stranski-Krastanow growth is obtained. In this case, the typically larger surface energy of the substrate material is reduced by a wetting layer of the deposited material. Additional material will then proceed three-dimensionally to minimize the strain energy by relaxing into the surrounding void and increasing the surface area. After a certain material coverage further accumulated strain is again reduced by defect formation. For a very large lattice mismatch or a large difference of surface energy densities, the entire wetting of the substrate is inhibited yielding Volmer-Weber growth. In this case, each island nucleation is typically accompanied by the formation of defects to reduce the strain energy and no coherent islands are obtained. A detailed qualitative model and a comparison to experiment is presented in Chapter 6.

# 3 Experimental methods

Synthesizing GaN quantum dots for optoelectronic applications was already achieved in 1996 by employing silicon for selective area growth [32, 117]. However, they suffered from very poor optical quality [34, 35] due to potential defect generation by silicon. Therefore, studying structural properties has to be connected to optical investigations for potential optoelectronic applications.

In this chapter, the primary experimental methods are presented. First, the experimental setup of the sample synthesis, metalorganic vapor-phase epitaxy, is described. Second, atomic force microscopy is presented, which is used to probe the surface morphology. The discussion is focused on the data analysis for offcut determination and quantum dot ensemble investigation by Gwyddion [118]. For optical investigation of individual quantum dots, mesa structures are processed into the samples by electron beam lithography to reduce the optical excitation volume. This process is presented to access individual quantum dots for optical investigations. Finally, micro photoluminescence is described to characterize optical properties of GaN quantum dots.

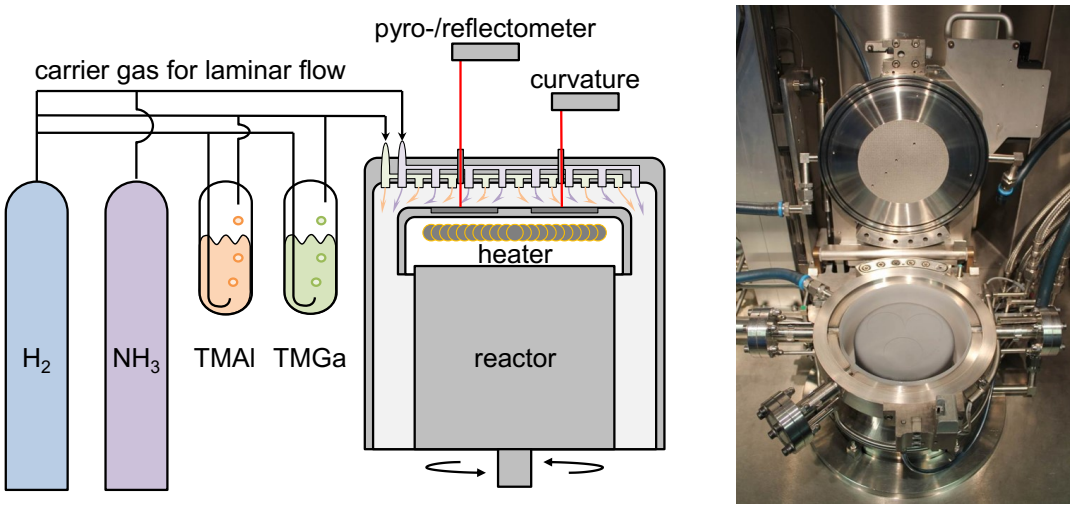


(a) MOVPE precursor flow diagram

(b) ThomasSwan reactor

Figure 3.1: Experimental metalorganic vapor-phase epitaxy setup

## 3.1 Metalorganic vapor-phase epitaxy

All samples are synthesized by metalorganic vapor-phase epitaxy. It is a specialized method of the chemical vapor deposition. Layer-by-layer epitaxy is maintained by a proper substrate with a suitable crystal structure and elevated temperatures allowing for decent adatom diffusion. The very simplified chemical reaction of a group-III element and a nitrogen precursor by the help of metalorganics is

$$(CH_3)_3(Ga, Al) + NH_3 \rightarrow (Ga, Al)N + 3CH_4, \tag{3.1}$$

with the educts being trimethylgallium $(CH_3)_3Ga$, trimethylaluminum $(CH_3)_3Al$, and ammonia $NH_3$, and the products being the group-III nitrides $(Ga, Al)N$, and methane $CH_4$. The metalorganic sources are liquids providing sufficient material supply by the control of the vapor-pressure inside a bubbler. The bubblers are kept within a stable environment to provide constant temperatures of 5°C and 18°C for trimethylgallium and trimethylaluminum, respectively. Ammonia under high pressure is kept liquid inside the gas supply bottle. With its vapor-pressure of 7 bar at room temperature, it is well above the pressure conditions inside the reactor chamber. A carrier gas allows maintaining the gas flow under laminar flow conditions. For the experiments of this thesis only hydrogen $H_2$ as a carrier gas is used. The gas flow is controlled via several mass-flow controllers and additional pressure controllers for the metalorganic bubblers. The relation between partial pressures, volume flows, and molar flows can be described by the ideal gas

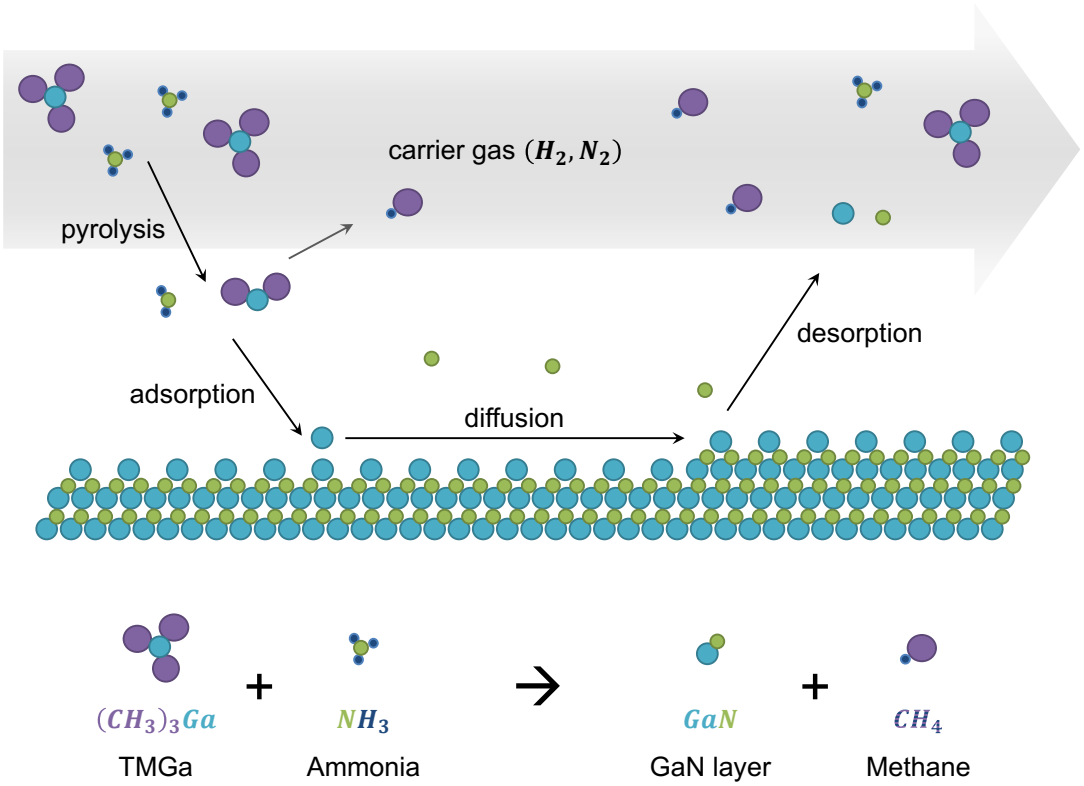


Figure 3.2: Simplified surface reactions inside a metalorganic vapor-phase epitaxy reactor with gallium adatoms diffusing on a 2x2 gallium reconstructed c-plane GaN surface.

equations [42]. The V/III ratio describes the ratio between the molar flows of ammonia $\phi_{\mathrm{NH_3}}$ and trimethylgallium $\phi_{\mathrm{TMAl}}$ or trimethylaluminum $\phi_{\mathrm{TMAl}}$:

$$\begin{aligned} V/III &= \frac{\phi_{\mathrm{NH_3}}}{\phi_{\mathrm{TMGa}} + \phi_{\mathrm{TMAl}}} \\ &= \frac{p_{\mathrm{N}}}{p_{\mathrm{III}}}, \end{aligned} \tag{3.2}$$

with the total partial pressures of the group-III elements $p_{\mathrm{III}}$ and of nitrogen $p_{\mathrm{N}}$ assuming complete pyrolysis of the educts.

A simplified gas flow diagram is shown in Fig. 3.1a. Two separated gas streams are injected into the shower head. One stream is related to the group-III educts and the other steam is related to the hydrides. A picture of the open ThomasSwan reactor is shown in Fig. 3.1b with the shower-head design and a susceptor with three 2 inch wafer pockets. Four larger openings inside the reactor lid allow for in-situ measurements with a Latec EpiTT and EpiCurve providing a pyrometric surface temperature $T_{\mathrm{pyro}}$, surface

| | | | |
|---|---|---|---|
| Reactor chamber height | $d_{\mathrm{gap}}$ | 6 | mm |
| Heat rate | $Q_{\mathrm{heat}}$ | 1.25 | K $\mathrm{s}^{-1}$ |
| Temperature stabilization | $t_{\mathrm{stabilize}}$ | 300 | s |
| Rotation speed | $r_{\mathrm{speed}}$ | 50 | rpm |
| | | 0.83 | Hz |
| Total gas flow | $\phi_{\mathrm{total}}$ | 8 | slm |
| | | 8000 | sccm |
| Reactor pressure | $p_{\mathrm{reactor}}$ | 200 | mbar |
| | | 20000 | Pa |

Table 3.1: General growth parameters for all of the growth studies.

reflectivity at 406 nm, 633 nm, and 951 nm, and the wafer curvature. A unique advantage of the ThomasSwan reactor design is the adjustable susceptor height. All experiments are operated with a gap of 6 mm between the reactor gas inlet and the susceptor minimizing vapor-phase pre-reactions often observed for Al related group-III nitride epitaxy [119].

The gaseous educts are guided over the susceptor providing a constant material supply, which is necessary for layer growth. A very simplified picture of the chemical reactions on the sample surface inside the reactor are sketched in Fig. 3.2. At first, the educts provided by the gas flow are pyrolytically dissociated close to the sample surface due to the elevated growth temperatures. Ammonia is a very stable molecule, which dissociates only partially even at elevated growth temperatures of 1000°C [100, 101]. Therefore, the supplied ammonia is typically very high leading to high vapor-phase V/III ratios. The dissociated educts are adsorbed on the surface and depending on the surface energy potential, they can diffuse on the surface. In the ideal case, only group-III atoms and nitrogen atoms are adsorbed. However, organic compounds interact with the surface as well [85–89]. The sample surface itself is also different to the bare bulk crystal by developing a surface reconstruction. One rather simple option is a 2x2 gallium surface reconstruction, as indicated in Fig. 3.2. For layer-by-layer growth the adatoms diffuse to the terrace edge and get incorporated at a kink position (Chapter 2.2.3). Additionally, adatoms can desorb from the surface back into the gas stream, where they flow into the exhaust together with the carrier gas, byproducts like methane, and unused educts.

The growth by metalorganic vapor-phase epitaxy is very complex. In order to investigate the influence of specific growth parameters, as many as possible have been kept constant. A detailed list is summarized in Table 3.1.

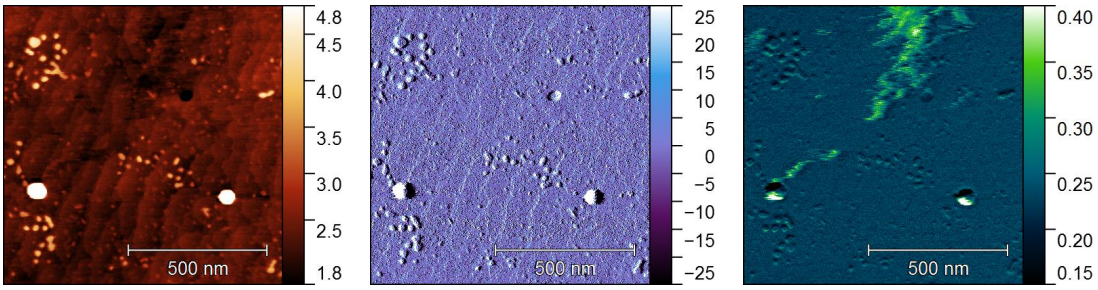


(a) Height signal by piezo voltage **[nm]** → surface morphology

(b) Error signal by cantilever deflection **[pm]** → vertical resolution limit

(c) Friction signal by cantilever torsion **[V]** → sensitive to organic adsorbates

Figure 3.3: Three measurement channels of an atomic force microscope in one scan direction providing independent surface information.

## 3.2 Atomic force microscopy

The surface morphologies are characterized by two different atomic force microscopes, which are a MultiMode$^{TM}$ SPM [120] and a DimensionIcon [121]. The used measurement mode is contact mode with constant force. Detailed descriptions can be found in the handbooks [120, 121]. After optimal cantilever adjustments, the height information is mainly related to the piezo voltage. A representative measurement is shown in Fig. 3.3. The achieved height resolution is limited by the deflection signal (Fig. 3.3b), which is less than 50 pm for 5 nm high structures after cantilever spring-constant calibration and constant-force feedback-loop optimization. This offers a characterization of surface features with an error of less than 1% in z-direction. The lateral resolution is limited by the measurement tip, which is in this case a Pyrex-Nitride Probe with a tip radius of less than 10 nm. The friction signal is a good indicator for organic adsorbates on the surface. It is directly related to the torsion of the cantilever. The bright green large spot in the upper part of Fig. 3.3c exhibits such adsorbates, which are hardly visible in the other signals. All three different signals can be monitored at the same time by the DimensionIcon [121], which is a great advantage over the older MultiMode$^{TM}$ SPM [120] with only two recorded live channels. Additionally, backward and forward scans can be recorded. Those interact differently with the organic adsorbates yielding two differently measured surface morphologies. Optimal tip quality and low noise signals without cantilever oscillations or organic contamination are necessary for image analysis with post-processing algorithms to select individual terrace facets or quantum dots.

In Chapter 4, AlN surfaces are characterized with different sample offcuts. Therefore, a

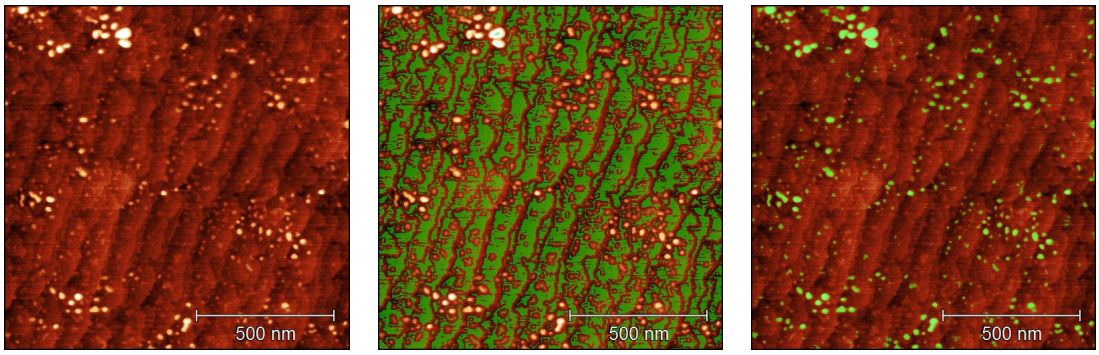


(a) Height signal **[2 nm]** → vicinal terraces covered with quantum dots

(b) Height signal **[2 nm]** → terraces masked $\alpha_{\text{offcut}} = (0.18 \pm 0.45)^\circ$

(c) Height signal **[2 nm]** → quantum dots masked

Figure 3.4: Determination of the sample offcut by statistical facet analysis ((a) → (b)). Quantum dot selection by height threshold after subtraction of background by low pass filter ((a) → (c)).

statistical facet analysis with Gwyddion [118] was performed. It determines the local gradient vector and plots the distribution as a function of polar angle coordinates. In the example of Fig. 3.4 with vicinal terraces of AlN covered by GaN quantum dots, the most common gradient of 0.18° is selected with a variation of ±0.45° to mask the area for facet contribution (Fig. 3.4b). If the overall measured area size determines the macroscopic surface, the obtained average gradient of the facets equals the offcut angle.

In the GaN quantum dot Chapters 5 and 6, a height threshold is employed to determine morphological properties of the quantum dot ensemble. In order to differentiate between the terraces and the quantum dots, a low-pass filter on the order of the terrace distance was applied. The obtained mask is used to read the morphological properties of each individual quantum dot. For the example shown in Fig. 3.4, the quantum dots are masked in green in Fig. 3.4c. The quantum dot ensemble can then be characterized in terms of height, diameter, aspect ratio, and density with the grain distribution function of Gwyddion [118]. Selecting three-dimensional structures on vicinal terraces is very challenging especially if they are only one monolayer high. Depending on the mask coverage, additional subjective errors have to be assumed.

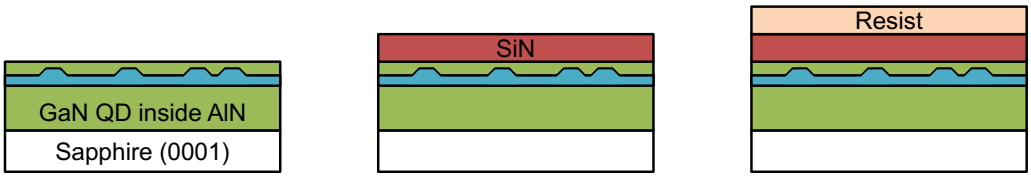


(a) GaN quantum dots embedded in AlN matrix by epitaxy

(b) SiN by chemical vapor deposition for hard mask process

(c) Resist by spin coating for soft mask process

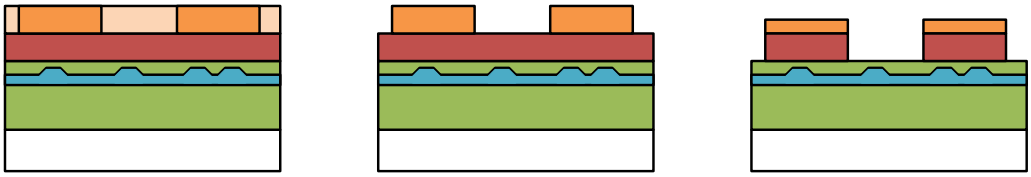

(d) Resist exposure with electron beam

(e) Development of resist

(f) Reactive-ion etching to transfer soft mask into hard mask

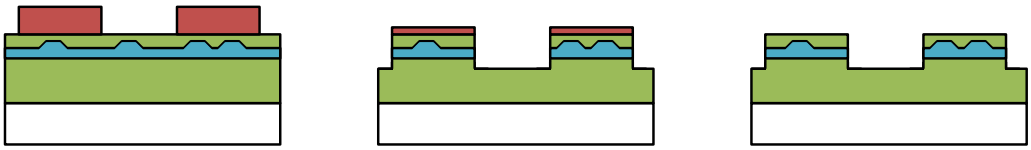

(g) Soft mask removal

(h) Inductively coupled plasma reactive-ion etching to transfer hard mask into mesa structures

(i) Hard mask removal by reactive-ion etching

Figure 3.5: Electron beam lithography process to realize mesa structures with only a few GaN quantum dots (QD) inside.

## 3.3 Electron beam lithography of mesa structures

In order to reduce the optical excitation volume below the Abbe-limit of photoluminescence measurements, planar GaN quantum dot samples were processed with mesa structures by electron beam lithography. Additional markers on the sample provide reproducible mesa measurements even after sample exchange. The process is based on a combination of a soft mask for electron beam lithography and a SiN hard mask for reactive-ion etching. All process steps are sketched in Fig. 3.5. The whole process starts with the epitaxial sample (Fig. 3.5a). AlN is a very stable material requiring very harsh etching conditions. Therefore, the sample needs to be covered by a hard mask made of SiN, which is deposited with chemical vapor deposition (Fig. 3.5b). The electron beam lithography on the other hand requires a soft mask, which is based on a spin coated resit AZ2070 (Fig. 3.5c). Applying an adhesive promoter (HMDS) before the spin coating of the resist helps to preserve small structures from floating during the development step. An additional conductive coating layer on the resist (SX AR-PC) reduces the charging of

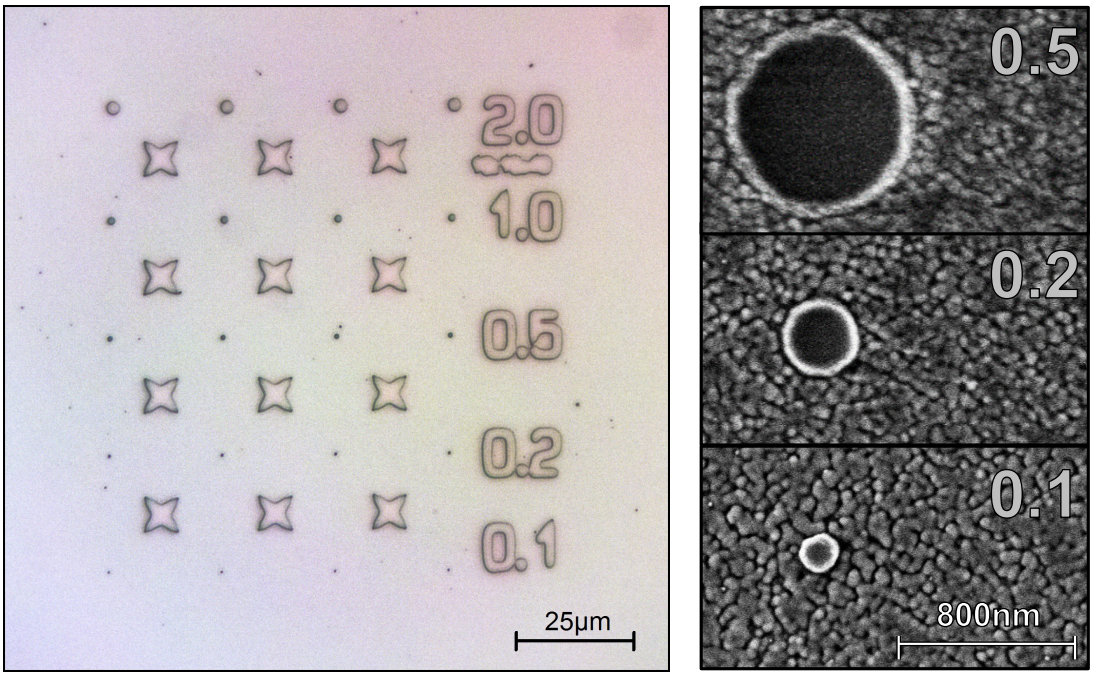


(a) Nomarski interference contrast microscope image of a 100x100 $\mu m^2$ mesa pattern with a mesa diameter gradient

(b) Scanning electron microscope image of different mesa structures

Figure 3.6: Light microscope image of a processed mesa pattern and electron microscope images with three different mesa diameters down to 150 nm for structure 0.1.

the isolating sample enabling patterns with very little drift during the electron beam exposure. The pattern is then written by a scanning electron microscope (Fig. 3.5d) with a bias voltage of $U_{\text{bias}} = 10\,\text{kV}$ and a single dot dose of about 40 aC corresponding to an area dose of about $40\,\mu\text{C}\,\text{cm}^{-2}$. The diameter size of the mesa structures is varied by the exposure time of single dots from 4 fC to 80 fC. After the exposure, the resist is developed by AZ726MiF for about 10 s and subsequently rinsed with water (Fig. 3.5e). The structures are transferred by reactive-ion etching into the hard mask (Fig. 3.5f) and cleaned by hot acetone to remove the remaining resist (Fig. 3.5g). The reactive-ion etching of SiN was performed with $SF_6$ under an argon atmosphere at about 3 Pa and 50 W. The etch rate is calibrated with a reference sample and an ellipsometer. Finally, the pattern is transferred into the sample by inductively coupled plasma reactive-ion etching (Fig. 3.5h) and the remaining SiN is removed with reactive-ion etching (Fig. 3.5i). The inductively coupled plasma reactive-ion etching of AlN was performed with chlorine under an argon atmosphere at about 5 Pa and 100 W.

Figure 3.6a exhibits a processed pattern with four similar mesa structures of an intended diameter variation from 0.1 $\mu$m up to 2 $\mu$m. Marker structures in between the mesas help

for better alignment during the optical measurements. In order to measure the mesa diameter, scanning electron microscopy images have been performed. The three smallest structures are shown in Fig. 3.6b, which exhibit diameters down to 150 nm. Profilometer measurements show a mesa height of about 200 nm, which is well above the 50 nm AlN cap thickness.

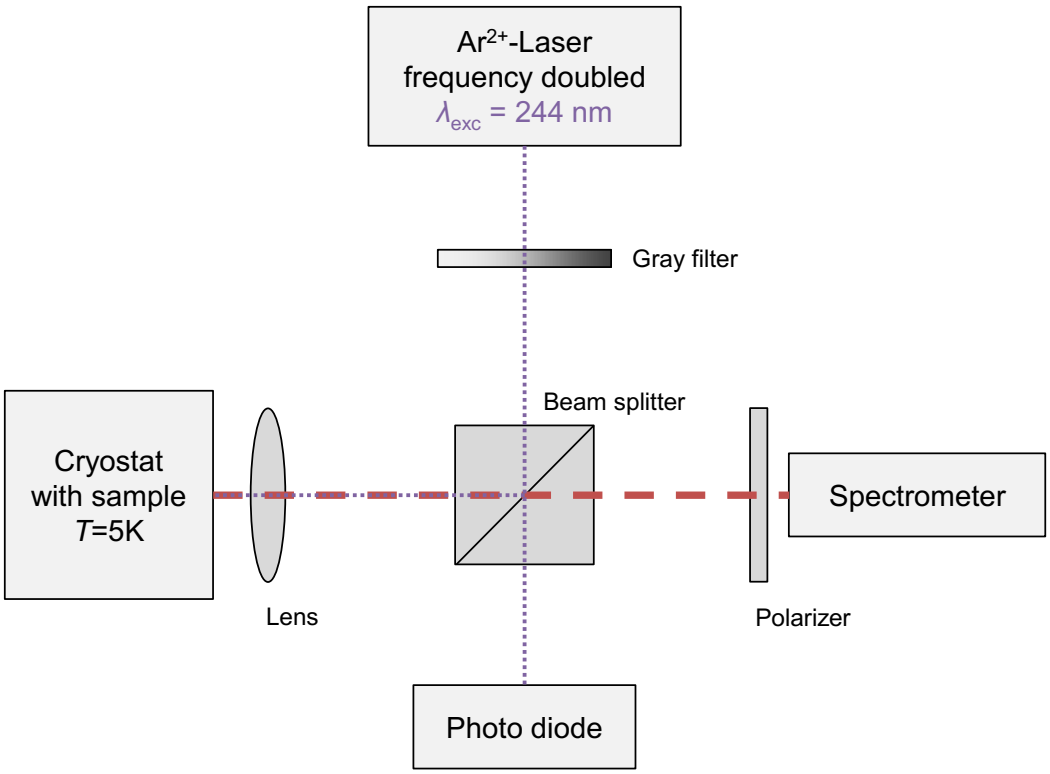


Figure 3.7: Schematic setup of micro photoluminescence.

## 3.4 Micro photoluminescence

The optical properties of GaN quantum dots are determined by photoluminescence, which measures the optical response of the sample after a high photon energy optical excitation. For a simple laser setup the probed volume is limited by the excitation wavelength, the numerical aperture of the lens, and the position of the focal point inside the sample. In a micro photoluminescence setup, high numerical aperture lenses are used offering excitation spot sizes on the order of 1 $\mu$m. For samples with quantum dot densities on the order of $10^{10}\,\mathrm{cm}^{-2}$, this would probe an ensemble of 100 quantum dots, which is not suitable for single quantum dot investigations. Therefore, mesa structures have been processed (Chapter 3.3) with diameters down to 150 nm. This allows studying 1 – 5 quantum dots per mesa structure. The optical setup was well developed and described by Kindel [105] and Callsen [106]. Figure 3.7 exhibits a schematic diagram of the micro photoluminescence setup. The sample is placed inside a helium-flow cryostat, which allows probing samples down to 5 K. A frequency doubled $Ar^{2+}$-ion laser with a wavelength of $\lambda_{\mathrm{exc}} = 244\,\mathrm{nm}$ is used for continuous wave excitation. The excitation

power can be varied via a continuous gray filter over at least three orders of magnitude and monitored via a photo diode. For higher spacial resolution, a microscopic lens is used with a 20x magnification and a numerical aperture of 0.4. An x-y-z piezo stage allows approaching and focusing individual mesa structures in a $100^3\,\mu\mathrm{m}^3$ range for detailed investigation. The spectrometer has a 1 m focal length and a liquid nitrogen cooled, 2048 pixel wide charge-coupled device. The spectral resolution is about 0.3 meV. A rotating half-wave plate in combination with a linear polarizer is used for polarization dependent measurements.

In order to differentiate between different types of exciton complexes (Chapter 2.1.4), power dependent and polarization dependent optical spectra are recorded. By analyzing the measured intensity of a peak $I$ as a function of the excitation power $P$, the number of exciton decay channels $n$ for the optical transition scales approximately with the exponent of the excitation power [30, 105, 106]. Below the saturation of the decay channels, it is simplified to

$$I \sim P^n. \tag{3.3}$$

This offers the identification of excitons or biexcitons with power dependent excitation measurements and a corresponding exponent of $n \simeq 1$ or $n \simeq 2$, respectively. Additionally, polarization dependent measurements allow identifying, if the optical features origin from the same quantum dot [104, 106]. Exciton transitions of the same quantum dot are separated by the fine-structure splitting $E_{\mathrm{FSS}}$ and exhibit an orthogonal optical polarization due to their electronic spin configuration (Chapter 2.1.4). On the other hand, biexcitons have a more complex spin configuration mainly depending on the lateral size of the quantum dot [104]. A classic biexciton with two electrons and holes in the opposite spin state emit a photon, which is parallel polarized to the exciton transition.

# 4 Achieving smooth step-flow AlN surfaces

GaN quantum dot growth is very sensitive to nucleation sites on the substrate. Especially, threading dislocations [69–71, 122] and step-bunches [31, 66–68] are very well known features leading to clustering and inhomogeneous growth. For many reported devices, the control of the surface morphology has a significant impact on the device efficiency [66, 123–125]. Due to the lack of native substrates, the AlN is grown on sapphire offering similar material properties necessary for epitaxy. Viola Küller [126] provided AlN templates for the presented study exhibiting step-bunching morphology unsuitable for homogeneous GaN quantum dot nucleation. In order to achieve smooth step-flow AlN surfaces, the pseudo-homoepitaxial growth of AlN is investigated in this chapter.

Three major growth morphologies can be distinguished for homoepitaxy: island growth, step-flow growth, and step-bunching growth (Chapter 2.2.4). The island nucleation of AlN on vicinal terraces has just recently been studied by Bryan et al. [127] and Pristovsek et al. [128]. They are able to control the transition between island growth and step-flow growth by changing the growth rate, V/III ratio, and temperature. The second growth morphology transition between step-flow growth and step-bunching growth has been observed in many optoelectronic material systems such as Si [129, 130], GaAs [131, 132], InP [133,134], GaN [135,136], and AlN [127,135]. The influence of the vicinal terrace width (substrate offcut, Chapter 2.2.1) is typically disregarded. It is an important technological parameter potentially allowing to control the growth morphology independent of selected growth conditions, which is investigated in this chapter.

In order to understand the physics leading to step-bunching, an analytical model of Schwoebel et al. [111] is presented. It is based on adatom surface diffusion theory

by Burton, Cabrera, and Frank [114]. Due to a fixed uniform terrace width, the analytical model reveals no direct indication of a growth morphology transition. Therefore, Schwoebel [111] and others [137–140] analyzed the growth speed stability of terrace edges yielding stable or unstable cases for extreme conditions. In this thesis, the analytical model is investigated by a Monte-Carlo approach, which allows studying the influence of a dynamic terrace width on the growth morphology. This approach is presented in the second section of the chapter, which explicitly allows differentiating between step-flow growth and step-bunching growth. Phase diagrams of the growth morphology are studied as a function of the terrace width, different surface diffusion rates, and the desorption rate. Additionally, the growth morphology transition is experimentally investigated by the pseudo-homoepitaxial growth of AlN, which is performed by metalorganic vapor-phase epitaxy. After presenting the sample structure and growth conditions in section three, surface morphologies are discussed as a function of the vicinal terrace width (substrate offcut, Chapter 2.2.1) and the V/III ratio, which are obtained by atomic force microscopy (Chapter 3.2). The theoretical and experimental results are finally combined in the conclusion.

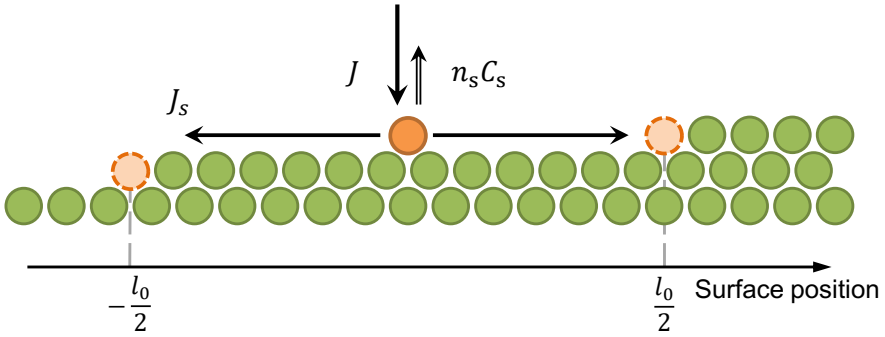


Figure 4.1: Schematic cross section of a surface with vicinal terraces (sketched by green circles). Adatoms (orange circles) with prominent incorporation positions at the upper and lower step-edge (dashed orange circles). The arrows illustrate all important participating atomic fluxes.

## 4.1 Analytical model

The non-equilibrium growth can be described by adatoms diffusing at the surface [114]. As explained in Chapter 2.2.3, the surface diffusion process includes adsorbed, desorbed, and incorporated adatoms. At steady state conditions a constant local adatom density on a vicinal terrace can be derived [111]. Due to a uniform terrace width of the model, no direct indication of a growth morphology transition is obtained, which might require a non-uniform terrace distribution like step-bunching growth. Still, the impact of the different surface rates will be discussed in the context of the different growth morphologies obtained by the Monte-Carlo approach (Chapter 4.2).

### 4.1.1 Derivation of equations

A cross section of the surface is illustrated in Fig. 4.1 for a one-dimensional case. All atoms of the solid crystal are sketched as green circles. The very complex surface reactions are simplified with a kinetic model by looking at only one adatom (solid orange circle), which is located on the terrace. The orange dashed circles show the only adatom incorporation sites defining the boundary conditions. According to the growth conditions, a material supply flux $J$ provides atoms for layer growth. At the same time atoms may desorb from the surface, which is proportional to the present adatom density times the desorption

rate $C_\mathrm{s}$. Both vertical contributions results in the vertical net flux $J_\mathrm{v}$

$$J_\mathrm{v} = J - n_\mathrm{s}(x)\, C_\mathrm{s}. \tag{4.1}$$

If the vertical net flux is negative, the surface morphology is determined by adatom desorption like in Chapter 5. If on the other hand the vertical net flux $J_\mathrm{v}$ is positive ($J > n_\mathrm{s}(x)\, C_\mathrm{s}$), layer growth is obtained. The local adatom density $n_\mathrm{s}(x)$ is correlated to the local lateral adatom flux $J_\mathrm{s}(x)$ by the Einstein diffusion relation

$$J_\mathrm{s}(x) = -D_\mathrm{s}\frac{\mathrm{d}n_\mathrm{s}(x)}{\mathrm{d}x}, \tag{4.2}$$

with the surface diffusion constant $D_\mathrm{s}$. If no nucleation is assumed, the fluxes have to obey the continuum equation

$$J_\mathrm{v} = \frac{\mathrm{d}J_\mathrm{s}(x)}{\mathrm{d}x}. \tag{4.3}$$

Combining Eq. 4.3 with Eq. 4.1 and 4.2, the surface diffusion is described by a linear second-order differential equation

$$J = C_\mathrm{s} n_\mathrm{s}(x) - D_\mathrm{s}\frac{\mathrm{d}^2 n_\mathrm{s}(x)}{\mathrm{d}x^2}, \tag{4.4}$$

which is solved by an exponential ansatz with the combination of the non-homogenous and the homogenous results:

$$n_\mathrm{s}\,(x) = \frac{J}{C_\mathrm{s}} + A\exp\left(-\frac{x}{\lambda_\mathrm{s}}\right) + B\exp\left(\frac{x}{\lambda_\mathrm{s}}\right), \tag{4.5}$$

with the diffusion length $\lambda_\mathrm{s}$ as a typical quantity for surface kinetics (Chapter 2.2.3). It is defined by the square root of the ratio between the surface diffusion constant $D_\mathrm{s}$ and the desorption rate $C_\mathrm{s}$

$$\lambda_\mathrm{s} = \sqrt{\frac{D_\mathrm{s}}{C_\mathrm{s}}}. \tag{4.6}$$

If no island nucleation is assumed and the surface is mainly characterized by vicinal terraces, adatom incorporation occurs only at the terrace step-edges. Therefore, boundary

conditions [111] are defined by

$$\begin{aligned} k_{-} n_{\mathrm{s}}\left(-\tfrac{l_0}{2}\right) - J_{-}^{\mathrm{des}} &= D_{\mathrm{s}} \frac{\mathrm{d}n_{\mathrm{s}}(x)}{\mathrm{d}x}\Big|_{x=-\frac{l_0}{2}} \\ k_{+} n_{\mathrm{s}}\left(\tfrac{l_0}{2}\right) - J_{+}^{\mathrm{des}} &= -D_{\mathrm{s}} \frac{\mathrm{d}n_{\mathrm{s}}(x)}{\mathrm{d}x}\Big|_{x=\frac{l_0}{2}}, \end{aligned} \tag{4.7}$$

with the adatom incorporation rates into the terrace step-edges $k_{-}$ and $k_{+}$, as well as the atom desorption fluxes from the terrace step-edges $J_{-}^{\mathrm{des}}$ and $J_{+}^{\mathrm{des}}$ at the lower (-) and upper (+) terrace step-edge, respectively.

The solution of the local adatom density $n_{\mathrm{s}}(x)$ can be described analytically by

$$\begin{aligned} n_{\mathrm{s}}(x) = \Big\{ & 2\tfrac{J}{C_{\mathrm{s}}}\Big[\left(\lambda_{\mathrm{s}}^2 + \lambda_{-}\lambda_{+}\right)\sinh\left(\tfrac{l_0}{\lambda_{\mathrm{s}}}\right) - \lambda_{+}\lambda_{-}\sinh\left(\tfrac{l_0-2x}{2\lambda_{\mathrm{s}}}\right) - \lambda_{-}\lambda_{+}\sinh\left(\tfrac{l_0+2x}{2\lambda_{\mathrm{s}}}\right) \\ & + \lambda_{\mathrm{s}}\left(\lambda_{-}+\lambda_{+}\right)\cosh\left(\tfrac{l_0}{\lambda_{\mathrm{s}}}\right) - \lambda_{\mathrm{s}}\lambda_{-}\cosh\left(\tfrac{l_0-2x}{2\lambda_{\mathrm{s}}}\right) - \lambda_{\mathrm{s}}\lambda_{+}\cosh\left(\tfrac{l_0+2x}{2\lambda_{\mathrm{s}}}\right)\Big] \\ & + 2\tfrac{J_{-}^{\mathrm{des}}}{C_{\mathrm{s}}}\left[\lambda_{\mathrm{s}}\cosh\left(\tfrac{l_0-2x}{2\lambda_{\mathrm{s}}}\right) + \lambda_{+}\sinh\left(\tfrac{l_0-2x}{2\lambda_{\mathrm{s}}}\right)\right] \\ & + 2\tfrac{J_{+}^{\mathrm{des}}}{C_{\mathrm{s}}}\left[\lambda_{\mathrm{s}}\cosh\left(\tfrac{l_0+2x}{2\lambda_{\mathrm{s}}}\right) + \lambda_{-}\sinh\left(\tfrac{l_0+2x}{2\lambda_{\mathrm{s}}}\right)\right] \Big\} \\ & \Big/ \left[ e^{\frac{l_0}{\lambda_{\mathrm{s}}}}\left(\lambda_{\mathrm{s}}+\lambda_{+}\right)\left(\lambda_{-}+\lambda_{\mathrm{s}}\right) - e^{\frac{-l_0}{\lambda_{\mathrm{s}}}}\left(\lambda_{\mathrm{s}}-\lambda_{+}\right)\left(\lambda_{-}-\lambda_{\mathrm{s}}\right)\right], \end{aligned} \tag{4.8}$$

where $\lambda_{-} = {}^{k_{-}}/_{C_{\mathrm{s}}}$ and $\lambda_{+} = {}^{k_{+}}/_{C_{\mathrm{s}}}$ describe characteristic capture lengths at the lower and upper terrace step-edges. In a simplified picture, the Ehrlich-Schwoebel barrier can be expressed by the ratio of the adatom incorporation rates ${}^{k_{-}}/_{k_{+}}$ with a positive Ehrlich-Schwoebel barrier for ${}^{k_{-}}/_{k_{+}} < 1$ and an inverse Ehrlich-Schwoebel barrier for ${}^{k_{-}}/_{k_{+}} > 1$.

### 4.1.2 Adatom density and adatom flux

For the growth of AlN with its very high binding energies [141, 142], the desorption from the terrace step-edges will be neglected assuming $\{J_{-}^{\mathrm{des}} = 0\} \wedge \{J_{+}^{\mathrm{des}} = 0\}$. Therefore, every following discussion will consider this fact and other interpretations can be related to this simplification. The model will be presented with its remaining five parameters, which are the terrace width $l_0$, the adatom incorporation rates at the terrace step-edges $k_{-}$ and $k_{+}$, the diffusion length $\lambda_{\mathrm{s}}$, and the desorption rate $C_{\mathrm{s}}$. It should be noted, that the diffusion length is correlated with the desorption rate by Eq. 4.4. Figure 4.2a exhibits the local adatom density $n_{\mathrm{s}}(x)$ in blue on a vicinal terrace width as a function of the

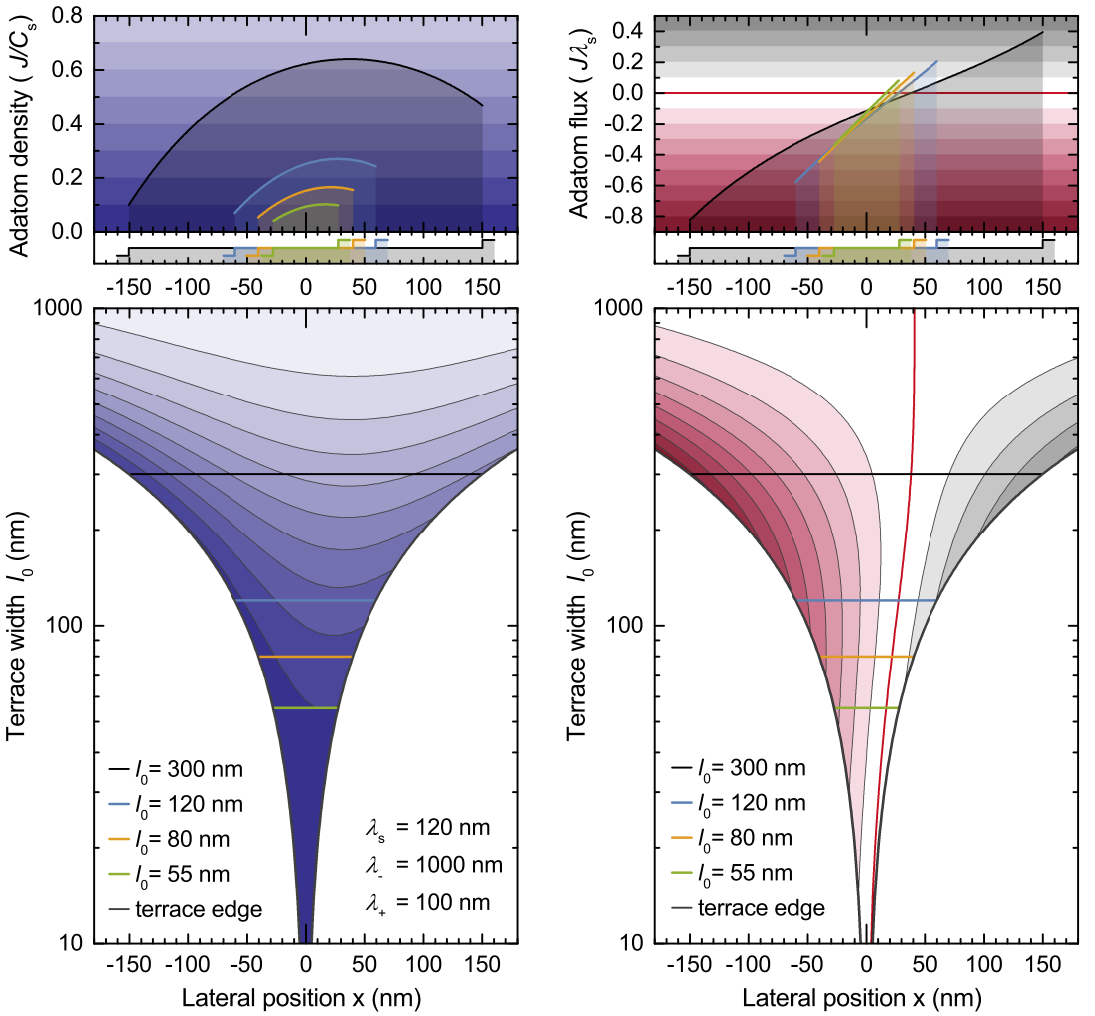


(a) Adatom density $n_s(x)$ [Eq. (4.8)]

(b) Adatom flux $J_s(x)$ [Eqs. (4.2),(4.8)]

Figure 4.2: Contour plots of (a) the adatom density in blue and (b) the adatom flux in pink/gray on a vicinal terrace as a function of the terrace width $l_0$ for a fixed diffusion length of $\lambda_s = 100\,\text{nm}$, desorption rate of $C_s = 10^{-2}\,\text{s}^{-1}$, and a dominant adatom incorporation at the lower terrace edge with the step-down incorporation rate $k_- = 10\,\text{nm/s}$ and a step-up incorporation rate $k_+ = 1\,\text{nm/s}$. Four representative profiles are selected in the upper plots for a terrace width of $l_0 = 300\,\text{nm}$ (black), $l_0 = 120\,\text{nm}$ (blue), $l_0 = 80\,\text{nm}$ (yellow), and $l_0 = 55\,\text{nm}$ (green) being much larger, larger, equal, and smaller than the step-flow/step-bunching transition terrace width (based on Monte-Carlo results Fig. 4.9), respectively.

terrace width $l_0$. The upper plot presents a cross section of the local adatom profile on a vicinal terrace for four selected terrace widths (black $l_0 = 300\,\text{nm}$, blue $l_0 = 120\,\text{nm}$, yellow $l_0 = 80\,\text{nm}$, green $l_0 = 55\,\text{nm}$). A simple sketch of the terrace profile is indicated in the narrow center plot underneath the selected adatom density profiles. The lower contour plot presents the influence of the terrace width on the local adatom density with

its color legend illustrated in the upper plot. The adatom diffusion on the terrace is described by the local adatom flux. Figure 4.2b exhibits the local adatom flux $J_s(x)$ on the terrace, which is plotted correspondingly to the local adatom density. The layer growth depends on the amount of incorporating atoms proportional to the adatom fluxes at the terrace step-edges. The conditions of Fig. 4.2 are chosen based on the Monte-Carlo simulation results of Chapter 4.2 leading to step-bunching growth for small terraces and step-flow growth for large terraces (step-flow/step-bunching transition at $l_0 = 80\,\mathrm{nm}$).

For steady state conditions the maximum of the local adatom density on the terrace is mainly defined by the ratio of the material supply $J$ and the desorption rate $C_s$ ($n_s^{max} = {}^{J}/_{C_s}$). If every incorporated atom is permanently bound and no desorption from the terrace step-edges is assumed, the obtained adatom density profile is independent of the material supply $J$. Hong et al. [140] reported a correlation of the material supply flux $J$ and the obtained growth morphology, which might be related to the neglected desorption at the step-edges $\{J_-^{des} \neq 0\} \vee \{J_+^{des} \neq 0\}$, a possible island nucleation limiting larger terrace width, or due to mutual parameter dependencies, where the material supply $J$ has an additional influence on the surface reconstruction and, therefore, on the surface diffusion coefficients $D_s$ (Chapter 2.1.3).

The influence of incorporation parameters can easily be seen for very large terrace widths, where the local adatom density (Eq.4.8) at the step-edges can be approximated by

$$n_s\left(\pm\frac{l_0}{2}\right)\Big|_{l_0 \gg \lambda_s} = \frac{J}{C_s}\,\frac{\lambda_s}{\lambda_\pm + \lambda_s}. \tag{4.9}$$

For very small capture lengths ($\lambda_\pm \ll \lambda_s$) with little adatom incorporation, the adatom density profile is mainly determined by the desorption and approaches a constant value $n_s(x) \approx {}^{J}/_{C_s}$. For very large capture lengths ($\lambda_\pm \gg \lambda_s$) with high adatom incorporation, the adatom density at the step-edges is pinned to zero and increases towards the center of the terrace. In the case of a large terrace width of $l_0 = 300\,\mathrm{nm}$ with $l_0 > \lambda_s$, the local adatom density maximum reaches just 65% of the adatom density limited by the desorption rate and the material supply flux ($n_s^{max} = {}^{J}/_{C_s}$). However, the local adatom density at the lower terrace step-edge with $n_s\left(-{}^{l_0}/_2\right)\Big|_{l_0=300\,\mathrm{nm}} = 10\%$ is still close to the limit of $n_s\left(-{}^{l_0}/_2\right)\Big|_{l_0 \gg \lambda_s} = 11\%$. At the upper terrace step-edge, the difference between the limit of $n_s\left({}^{l_0}/_2\right)\Big|_{l_0 \gg \lambda_s} = 55\%$ and $n_s\left({}^{l_0}/_2\right)\Big|_{l_0=300\,\mathrm{nm}} = 47\%$ is slightly larger. The increase of the adatom density from the terrace step-edges towards the center is characterized by the diffusion length $\lambda_s$ and the adatom capture lengths $\lambda_-$

and $\lambda_+$. For the chosen diffusion parameters ($\lambda_- > \lambda_+$), the adatom maximum is shifted towards the upper terrace edge, as also observed by Xie et al. [139]. They noticed that an incorporation energy barrier at the upper step-edge is necessary to obtain step-bunching growth. In the cases of Fig. 4.2, the ratio between the adatom flux at the upper and lower terrace edges increases for smaller terrace. However, no fundamental indication at the terrace width of $l_0 = 80\,\mathrm{nm}$ is found, which could yield a morphology transition similar to the Monte-Carlo investigation (Chapter 4.2) with step-flow growth at $l_0 = 120\,\mathrm{nm}$, step-bunching growth at $l_0 = 55\,\mathrm{nm}$, and with $l_0 = 80\,\mathrm{nm}$ being right at the transition of both surface morphologies.

In order to elaborate a deeper understanding of the influence of individual surface diffusion parameters, contour plots in Fig. 4.3 exhibit the local adatom density and the local adatom flux as a function of the step-down and step-up incorporation rates $k_-$ and $k_+$, the diffusion length $\lambda_\mathrm{s}$, and the desorption rate $C_\mathrm{s}$. All subfigures share the same color scales with the local adatom density in blue, the local adatom flux in pink/gray. Additionally, the surface morphology obtained by the Monte-Carlo approach is indicated in green for step-bunching growth and yellow for step-flow growth (Chapter 4.2). If incorporation energy barriers at the upper and lower terrace step-edge exist, the position of the local adatom density maximum with a zero net flux (red contour line) depends on the ratio of the two incorporation barriers [139], the diffusion length, and the desorption rate. By increasing the step-down incorporation $k_-$ (Fig. 4.3a), the local adatom density maximum shifts towards the upper terrace step-edge with a favored adatom incorporation at the lower terrace step-edge. A similar picture is obtained by reducing the step-up incorporation rate $k_+ < 2\,\mathrm{nm/s}$ (Fig. 4.3b) with a favored adatom incorporation at the lower terrace step-edge. For very low adatom diffusion on the surface (Fig. 4.3c, $\lambda_\mathrm{s} < 10\,\mathrm{nm}$), the local adatom density profile is flat in the center of the terrace and proportional to the material supply over the desorption rate. Few adatoms will reach the terrace edges and contribute to potential layer growth. At larger diffusion lengths ($10\,\mathrm{nm} < \lambda_\mathrm{s} < 100\,\mathrm{nm}$), adatoms from all over the terrace can reach the terrace edge lowering the local adatom density. This causes a shift of the adatom maximum away from zero. For very large diffusion lengths ($\lambda_\mathrm{s} > 100\,\mathrm{nm}$), all adatoms will reach the terrace edge and get incorporated resulting in very little adatom desorption. Due to the asymmetric incorporation rates $k_- > k_+$ and a sufficient diffusion length $\lambda_\mathrm{s} > l_0$, the local adatom density maximum shifts to the upper terrace step-edge leading to an asymmetric material incorporation. The influence of the desorption rate $C_\mathrm{s}$ on the local adatom density and the local adatom flux is shown in Fig. 4.3d. It shall be noted, that

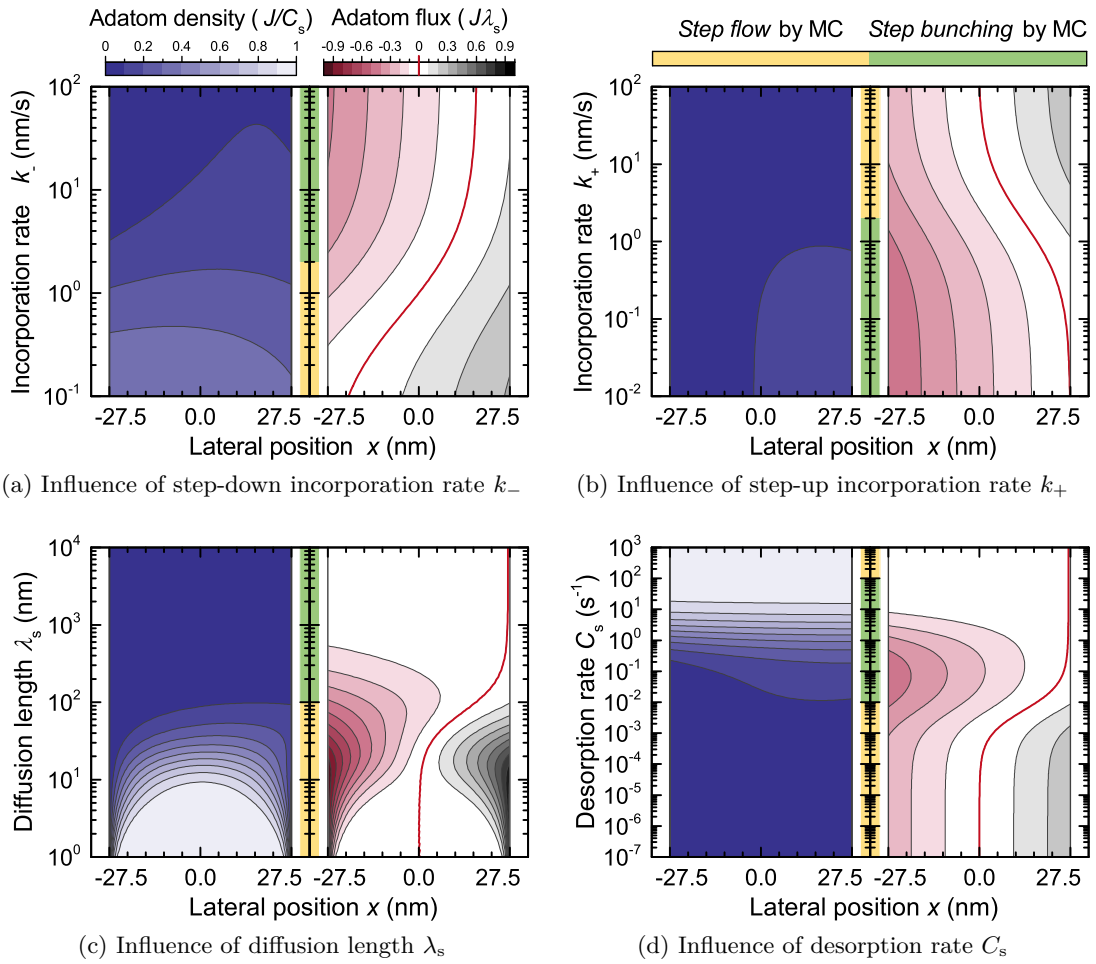


(a) Influence of step-down incorporation rate $k_-$

(b) Influence of step-up incorporation rate $k_+$

(c) Influence of diffusion length $\lambda_s$

(d) Influence of desorption rate $C_s$

Figure 4.3: Contour plots of the adatom density (blue, [Eq. 4.8]) and adatom flux (pink and gray, [Eqs. 4.2,4.8]) on a vicinal terrace with a width of $l_0 = 55\,\text{nm}$ as a function of (a) the step-down incorporation rate $k_-$, (b) the step-up incorporation rate $k_+$, (c) the diffusion length $\lambda_s$, and (d) the desorption rate $C_s$. For comparison, the surface morphology results obtained by the Monte-Carlo simulation (MC, Chapter 4.2) are indicated in between with step-flow growth (yellow) and step-bunching growth (green). Remaining fixed parameters are chosen to be similar to the Monte-Carlo simulation (Fig. 4.7 and 4.8) with the terrace width $l_0 = 55\,\text{nm}$, the diffusion length $\lambda_s$ =100 nm, the desorption rate $C_s = 10^{-2}\,\text{s}^{-1}$, the step-down incorporation rate $k_-$ =100 nm/s, and the step-up incorporation rate $k_+$ =1 nm/s.

the diffusion length is kept constant. For very low desorption rates ($C_s < 10^{-2}\,\text{s}^{-1}$), all adatoms have enough time to diffuse to the terrace step-edges reducing the local adatom density. A symmetric adatom flux profile is caused by the very large capture lengths ($\lambda_- \gg \lambda_s, \lambda_+ \gg \lambda_s$) pinning the adatom density at the terrace step-edge to zero (Eq. 4.9). For larger desorption rates ($C_s > 10^{-2}\,\text{s}^{-1}$), the adatom density increases all the way up to the maximum limit for very high desorption rates. It should be noticed, that the overall adatom density is in units of $\frac{J}{C_s}$ , which reduces the absolute adatom

density on the terrace with increasing desorption rate. At some point ($C_s > 10^2\,s^{-1}$) the adatom density is dominated by adatom desorption rather than adatom incorporation ($\lambda_- \approx 0, \lambda_+ \approx 0$) resulting in a constant adatom density (Eq. 4.9).

In order to look for an explicit transition feature in the analytical model, the conditions yielding step-flow growth (yellow) and step-bunching growth (green) by the Monte-Carlo approach (Chapter 4.2) are already indicated next to the adatom density and adatom flux in Fig. 4.3. Apparently, step-bunching growth is obtained for a favored adatom incorporation at the lower terrace step-edge combined with a sufficient adatom diffusion on the terrace, where the vast majority of the adatoms can reach the terrace step-edge. Low symmetric and high constant adatom densities yield step-flow growth. Despite these observations, no further explicit transition feature could be identified for the analytical model.

## 4.2 Monte-Carlo approach

In the literature, the diffusion model is typically investigated by analyzing the stability of a terrace edge growth speed [111, 137–140]. This offers only an indirect indication for the surface transition and no detailed description of the transition conditions. However, the developed Monte-Carlo approach simulates layer growth of 200 ML yielding direct surface morphologies, which allows distinguishing step-flow growth and step-bunching growth by evaluating the average step height. The layer growth is simulated by random atom incorporation at the terrace step-edge proportional to the adatom fluxes based on the analytical model in Chapter 4.1. This net adatom flux distribution at the terrace step-edges provides the incorporation probability distribution for the Monte-Carlo approach. First, the Monte-Carlo algorithm is described in general. Second, the evolution of obtained growth morphologies are presented, and finally, phase diagrams of the growth morphology as a function of surface diffusion rates are discussed.

### 4.2.1 Monte-Carlo algorithm

Layer growth is obtained for a positive vertical net flux $J_\mathrm{v}$ (Eq. 4.1). In this case, atoms are provided by the material supply $J$ to generate a local adatom density $n_\mathrm{s}\,(x)$ on each terrace. The adatom incorporation at the terrace step-edges is then based on the local adatom flux at the terrace step-edges. The combination of the lower $J_\mathrm{s}(l_i)$ and upper $-J_\mathrm{s}(-l_{i+1})$ adatom fluxes provides the local incorporation probability $p_i(t_1)$ at a terrace step $i$ by

$$p_i\,(t_1) = \frac{J_\mathrm{s}\Big(l_i(t_1)\Big) - J_\mathrm{s}\Big(-l_{i+1}(t_1)\Big)}{\sum_{i=1}^{N_\mathrm{steps}} \pm J_\mathrm{s}\Big(\pm\, l_i(t_1)\Big)}, \tag{4.10}$$

with the direction dependent $-J_\mathrm{s}(-l_{i+1})$ being a positive contribution.

The situation at the terrace step-edges is sketched in Fig. 4.4a. At the starting time $t_1$ all terraces have an equal terrace width of $l_i = l_0$. This corresponds to a uniform probability distribution. At $t_2$ after an adatom is incorporated at step $i$, the terrace width of $l'_i$ is reduced by one atom and the terrace width $l'_{i+1}$ is increased by one atom (Fig. 4.4b). Therefore, the adatom fluxes related to those terraces have to be recalculated for the next adatom incorporation. Depending on the surface diffusion rates the relative adatom incorporation probability will be different. Fig. 4.4c exhibits different conditions

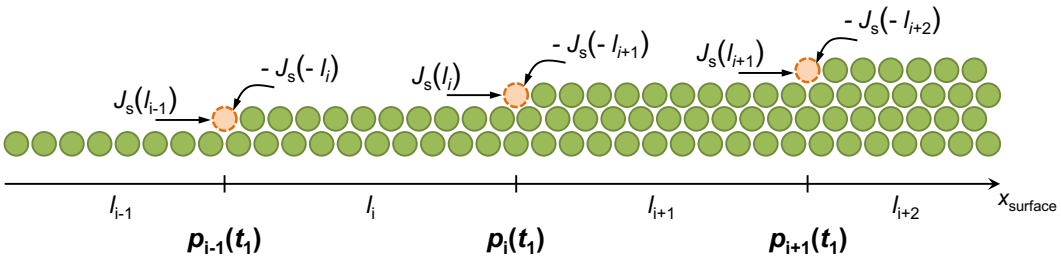


(a) Initial growth situation of uniform vicinal terraces.

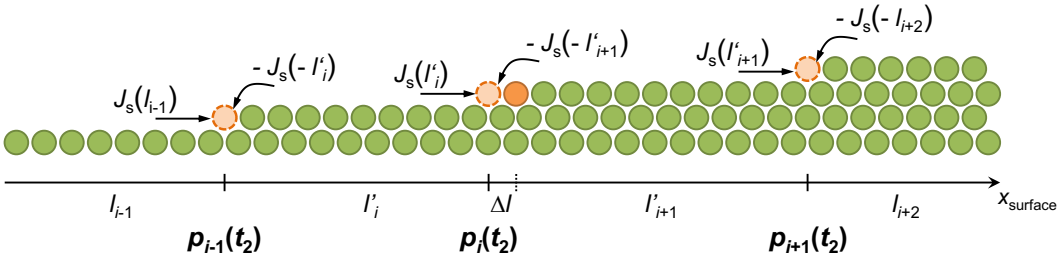


(b) Growth situation after one adatom incorporated at step $i$.

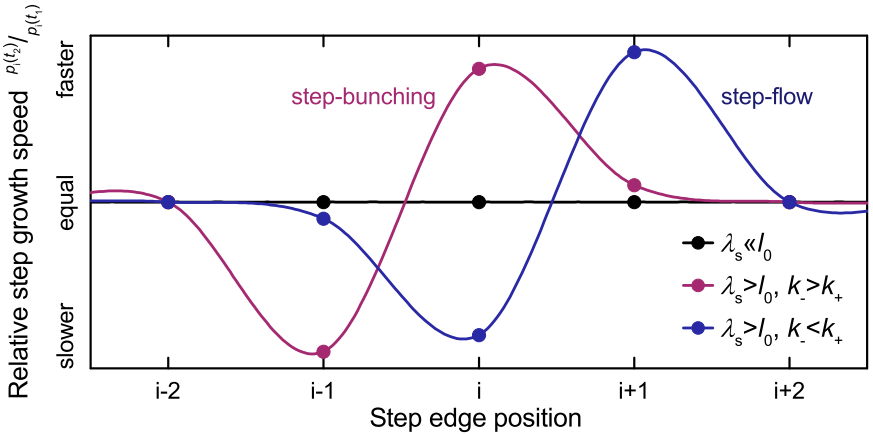


(c) Changed relative step growth speed after one adatom incorporated at step $i$.

Figure 4.4: Impact of different growth conditions on the incorporation probability distribution after an adatom incorporation at step $i$.

favoring the growth speed of different terraces. The adatom incorporation probability at the terrace step-edges is independent of the terrace width for very small diffusion length $\lambda_s \ll l_0$ (Fig. 4.4c, black), symmetric adatom incorporation rates $k_- = k_+$, or very high desorption rates as discussed in Chapter 4.1.2. This results in growth conditions promoting step-flow growth. If the amount of adatom incorporating at the terrace step-edges depends on the terrace width ($\lambda_s > l_0$), two different situations can be found. For the inverse Ehrlich-Schwoebel barrier $k_- > k_+$ (Fig. 4.4c, magenta) with a favored

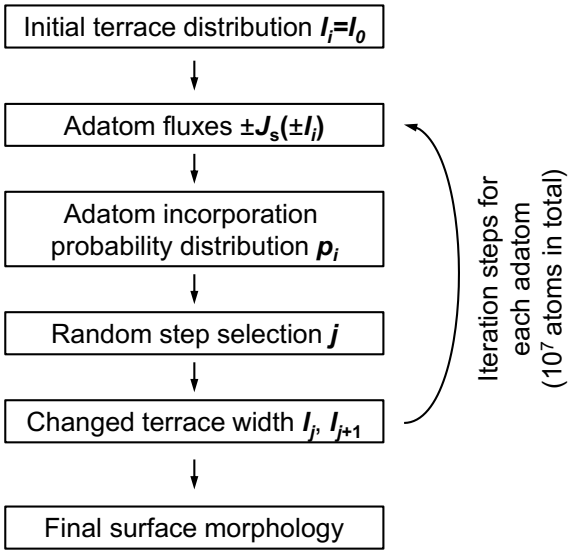


Figure 4.5: Schematic iteration chain of the Monte-Carlo algorithm.

adatom incorporation at the lower terrace step-edge, larger terraces have an increased growth speed yielding step-bunching growth. For the positive Ehrlich-Schwoebel barrier $k_- < k_+$ (Fig. 4.4c, blue) with a favored adatom incorporation at the upper terrace step-edge, larger terraces promote the growth of the adjacent upper terrace. This is a self-stabilizing process yielding highly regular step-flow growth.

In order to obtain surface morphologies for different growth conditions, layer growth is based on a Monte-Carlo approach. If no island nucleation on the terrace is assumed, adatoms incorporated at the terrace step-edge are the only contribution for layer growth. Therefore, the probability for adatom incorporation is based on the adatom fluxes at the terrace step-edges (Eq. 4.10). The iteration chain of the Monte-Carlo growth algorithm is illustrated in Fig. 4.5. Based on the terrace width distribution $l_i$, the adatom fluxes at the terrace edges $J_\mathrm{s}(l_i)$ are calculated correlating via Eq. 4.10 with an adatom incorporation probability at every terrace step-edge $p_i(t_1)$. Based on the probability distribution $p_i(t_1)$, a terrace step-edge $j$ is then randomly selected for adatom incorporation altering the adjacent terrace widths $l_j$ and $l_{j+1}$. Consequently, the depending adatom fluxes $J_\mathrm{s}(l_j)$ and $J_\mathrm{s}(l_{j+1})$ have to be updated and a new adatom incorporation probability distribution $p_i(t_2)$ is obtained for the following atom incorporation. The first iteration step is exemplarily illustrated in Fig. 4.4. A super cell of 100 vicinal terraces with periodic boundaries enables the investigation of layer growth with step-bunching heights up to about 20 ML. The algorithm has to iterate for all incorporated adatoms, which are about $10^5$ atoms per monolayer times 200 ML resulting in $10^7$ atoms per simulated

surface. One time step of the algorithm is associated with the incorporation of one adatom. Accordingly, simulated growth relates to different growth times depending on the provided net material supply $J_\mathrm{v}$. The layer growth can be described by Markov chains. This means, the adatom incorporation at each terrace step-edge only depends on the present vicinal terrace width distribution and is independent of the historic evolution [112]. To define proper starting conditions, every layer growth originates from equally spaced vicinal terraces on the surface. It should be noticed, that the finally obtained surface morphology is independent of the starting conditions and does only depend on the surface diffusion rates after enough material is deposited to develop or flatten a certain characteristic step-bunching height.

### 4.2.2 Morphology evolution for different growth conditions

Figure 4.6 exhibits the morphology evolution for positive and inverse Ehrlich-Schwoebel barriers and different diffusion lengths. The surface morphology is characterized by the cross section of the surface with different terrace step-heights in monolayers. Each simulated growth evolution starts with a homogeneous vicinal terrace width distribution with uniform terrace widths of $l_i(t_0) = l_0 = 55\,\mathrm{nm}$. The desorption rate $C_\mathrm{s} = 10^{-2}\,\mathrm{s}^{-1}$ and the step-up incorporation rate $k_+ = 1.0\,\mathrm{nm/s}$ are kept constant. Two different step-down incorporation rates at the lower terrace step-edge are selected with $k_- = 0.5\,\mathrm{nm/s}$ (Fig. 4.6, blue) and $k_- = 5.0\,\mathrm{nm/s}$ (Fig. 4.6, magenta) yielding a respective positive or inverse Ehrlich-Schwoebel barrier. Additionally, the diffusion length is varied from $\lambda_\mathrm{s} = 4\,\mathrm{nm}$ to $2500\,\mathrm{nm}$. Each row of plots exhibits the morphology after the growth of a certain layer thickness increasing exponentially from 1 ML to 64 ML. Depending on the growth conditions, stable morphologies are obtained after characteristic layer growth thicknesses. For a positive Ehrlich-Schwoebel barrier with $k_- < k_+$ and a sufficient diffusion length $\lambda_\mathrm{s} > 100\,\mathrm{nm}$ (Fig. 4.6, dark blue), the equally spaced vicinal terraces are maintained right from the start yielding highly stable step-flow growth. For diffusion lengths of $\lambda_\mathrm{s} < 100\,\mathrm{nm}$ and independent of the Ehrlich-Schwoebel barrier (Fig. 4.6, bright blue and bright magenta), the surface is dominated by terraces with monolayer steps yielding step-flow growth. In this case, the terrace widths are fluctuating due to the randomness of adatom incorporation at every terrace step-edge. The shortest terrace width is limited by the growth conditions, for which the homogenous equal adatom incorporation probability is redeemed. For the inverse Ehrlich-Schwoebel barrier with $k_- > k_+$ and a sufficient diffusion length $\lambda_\mathrm{s} > 100\,\mathrm{nm}$ (Fig. 4.6, dark magenta), step-bunching immediately starts to develop and stabilizes at a constant value. This

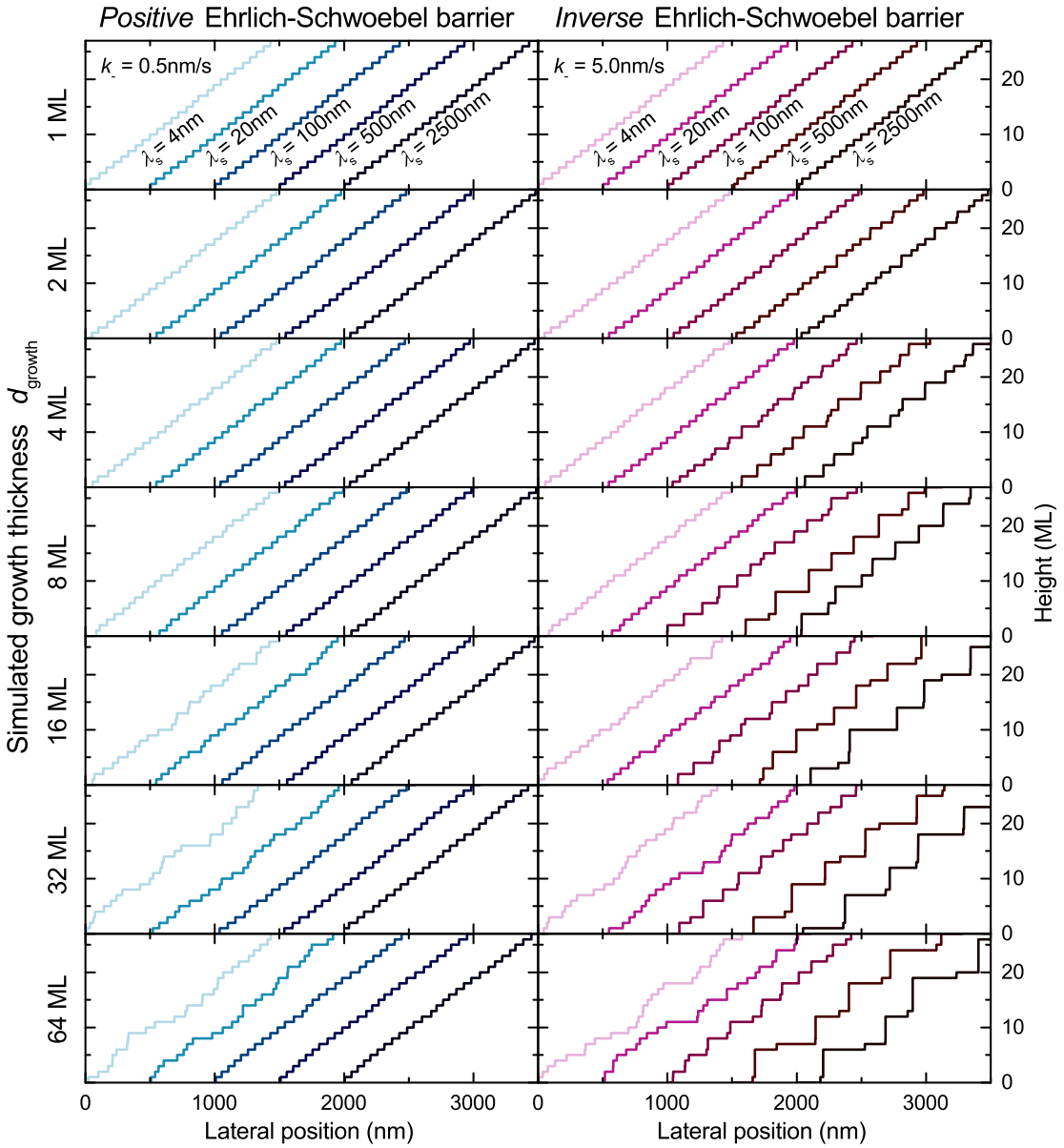


Figure 4.6: Simulated growth morphologies after the deposition of different layer thicknesses (rows, $d_{\mathrm{growth}} = 1\,\mathrm{ML}$, 2 ML, 4 ML, 8 ML, 16 ML, 32 ML, and 64 ML) at different diffusion lengths ($\lambda_{\mathrm{s}} = 4\,\mathrm{nm}$, 20 nm, 100 nm, 500 nm, 2500 nm) and step-down incorporation rates of $k_- = 0.5\,\mathrm{nm/s}$ and $k_- = 5.0\,\mathrm{nm/s}$ yielding a respective positive or inverse Ehrlich-Schwoebel barrier. The vicinal terrace width is $l_0 = 55\,\mathrm{nm}$, the desorption rate is $C_{\mathrm{s}} = 10^{-2}\,\mathrm{s}^{-1}$, and the step-up incorporation rate is $k_+ = 1.0\,\mathrm{nm/s}$.

is limited by the growth conditions, for which an asymmetric adatom incorporation is still promoted with a sufficient adatom diffusion. Finally, all obtained surfaces are compared by a characteristic average step-height. An applied Commonest filter [143] includes vicinal terraces with a width of $l_i < 5\,\mathrm{nm}$ close to the step-bunching region into

the average step-bunching height providing more robust and reliable results.

### 4.2.3 Homoepitaxial phase diagrams by the Monte-Carlo approach

In order to investigate the influence of different surface diffusion rates on the surface morphology, Monte-Carlo simulations are performed for different growth conditions. A layer thickness of 200 ML ($10^7$ incorporated atoms) ensures morphologies, which are independent of the starting conditions. Additionally, sound statistics are provided by analyzing 24 independent growth simulations for the same conditions.

Figure 4.7 exhibits phase diagrams of the surface morphology as a function of the incorporation rates at the upper $k_+$ and lower $k_-$ terrace step-edges, and the diffusion length $\lambda_s$ for a constant desorption rate $C_s = 10^{-2}\,s^{-1}$ and an average terrace width $l_0 = 55\,nm$. The characteristic step-bunching height is color coded in green with step-heights above 2 ML for step-bunching growth (green contours) and step-flow growth below 2 ML (white contour). Due to the complexity of the multi-dimensional parameter space, only a very narrow window can be presented. Figure 4.7a exhibits the morphology transition as a function of the step-up incorporation rate $k_+$ and the diffusion length $\lambda_s$ for a constant step-down incorporation rate $k_- = 100\,nm/s$, desorption rate $C_s = 10^{-2}\,s^{-1}$, and an average terrace width $l_0 = 55\,nm$. Figure 4.7b exhibits the morphology transition as a function of the step-down incorporation rate $k_-$ and the diffusion length $\lambda_s$ for a constant step-up incorporation rate $k_+ = 1\,nm/s$, desorption rate $C_s = 10^{-2}\,s^{-1}$, and an average terrace width $l_0 = 55\,nm$. Figure 4.7c exhibits the morphology transition as a function of the step-up incorporation rate $k_+$ and the step-down incorporation rate $k_-$ for a constant diffusion length $\lambda_s = 10^4\,nm$, desorption rate $C_s = 10^{-2}\,s^{-1}$, and an average terrace width $l_0 = 55\,nm$. The yellow dash-dotted lines represent plane cuts of the different section views. As discussed in Chapter 4.2.2, the step-bunching growth is obtained for sufficient diffusion lengths $\lambda_s \gtrsim 100\,nm$ and an inverse Ehrlich-Schwoebel barrier $k_- > k_+$ (indicated by a red dashed line in Fig. 4.7). The step-bunching height is increasing with larger diffusion length $\lambda_s$ and step-down incorporation rate $k_-$. For very large diffusion lengths $\lambda_s > 10^4\,nm$ the step-bunching height is limited by the ratio of the incorporation rates $^{k_-}/_{k_+}$, which is shown in Fig. 4.7c. It appears that an asymmetric adatom incorporation of $k_- > 2k_+$ is necessary to obtain step-bunching growth. This means that step-flow growth is obtained even for very small inverse Ehrlich-Schwoebel barriers. For very large step-down incorporation rates $k_- > 100\,nm/s$ the step-bunching height appears to be limited by step-up incorporation rate $k_+$ and the diffusion length

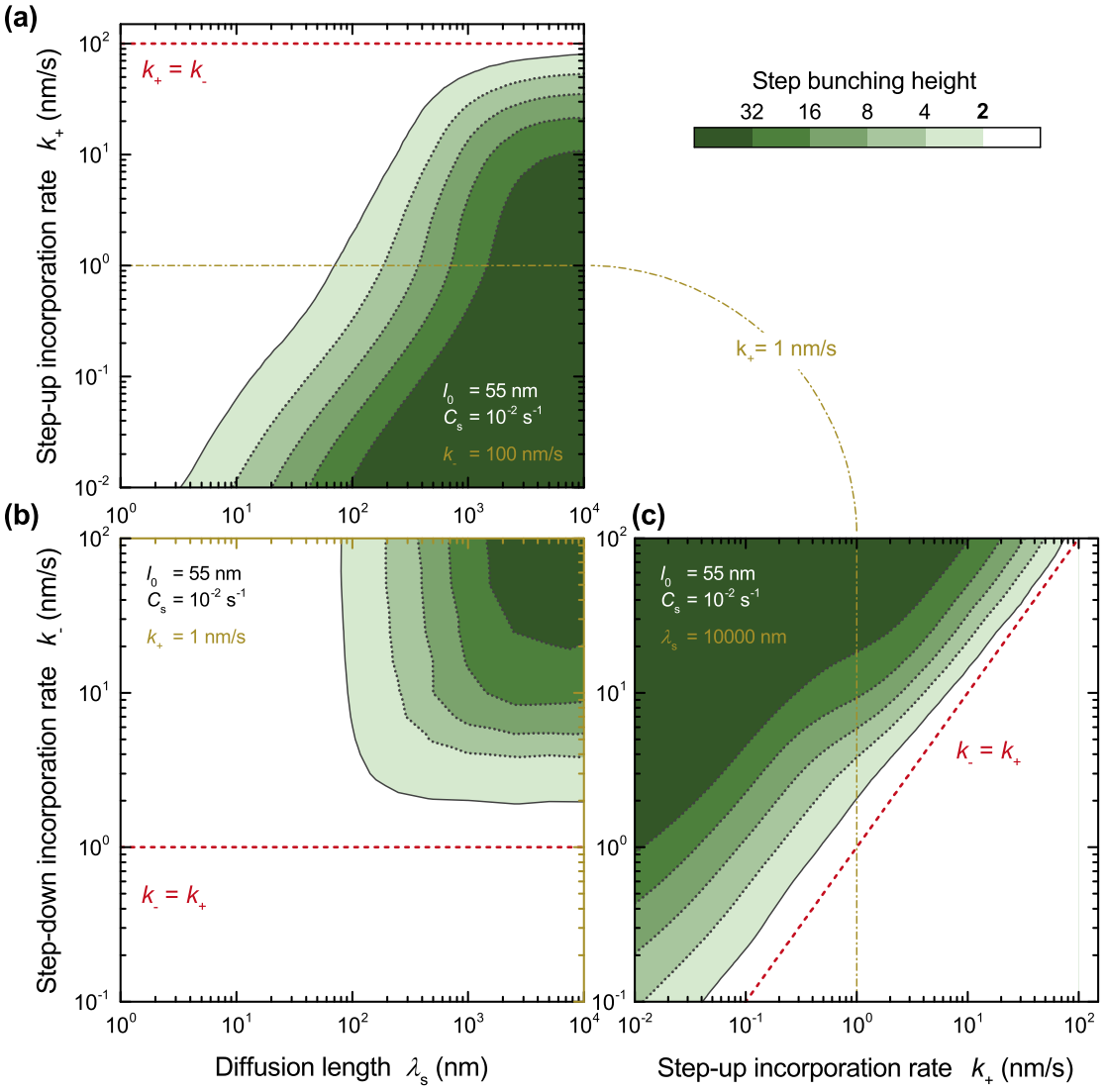


Figure 4.7: Contour plots of the step-bunching height dominating the surface morphology as a function of the diffusion length $\lambda_s$, and the incorporation rates $k_-$ and $k_+$ for a fixed terrace width $l_0 = 55\,\text{nm}$ and a fixed desorption rate $C_s = 10^{-2}\,\text{s}^{-1}$. White contours corresponds to step-flow growth with an average step height below 2 ML, and step-bunching with the step-bunching height color coded in green. The red dashed line highlights equal incoporation rates with $k_+ = k_-$. (a) growth morphology for a fixed step-down incorporation rate $k_- = 100\,\text{nm/s}$. (b) growth morphology for a fixed step-up incorporation rate $k_+ = 1\,\text{nm/s}$. (c) growth morphology for a fixed diffusion length $\lambda_s = 10^4\,\text{nm}$.

$\lambda_s$ as shown in Fig. 4.7a. Self stabilizing step-flow growth is either obtained for favored adatom incorporation at the upper terrace edge with $k_- < 2k_+$, or irregular step-flow growth is obtained for small diffusion lengths with an adatom incorporation independent of the terrace width.

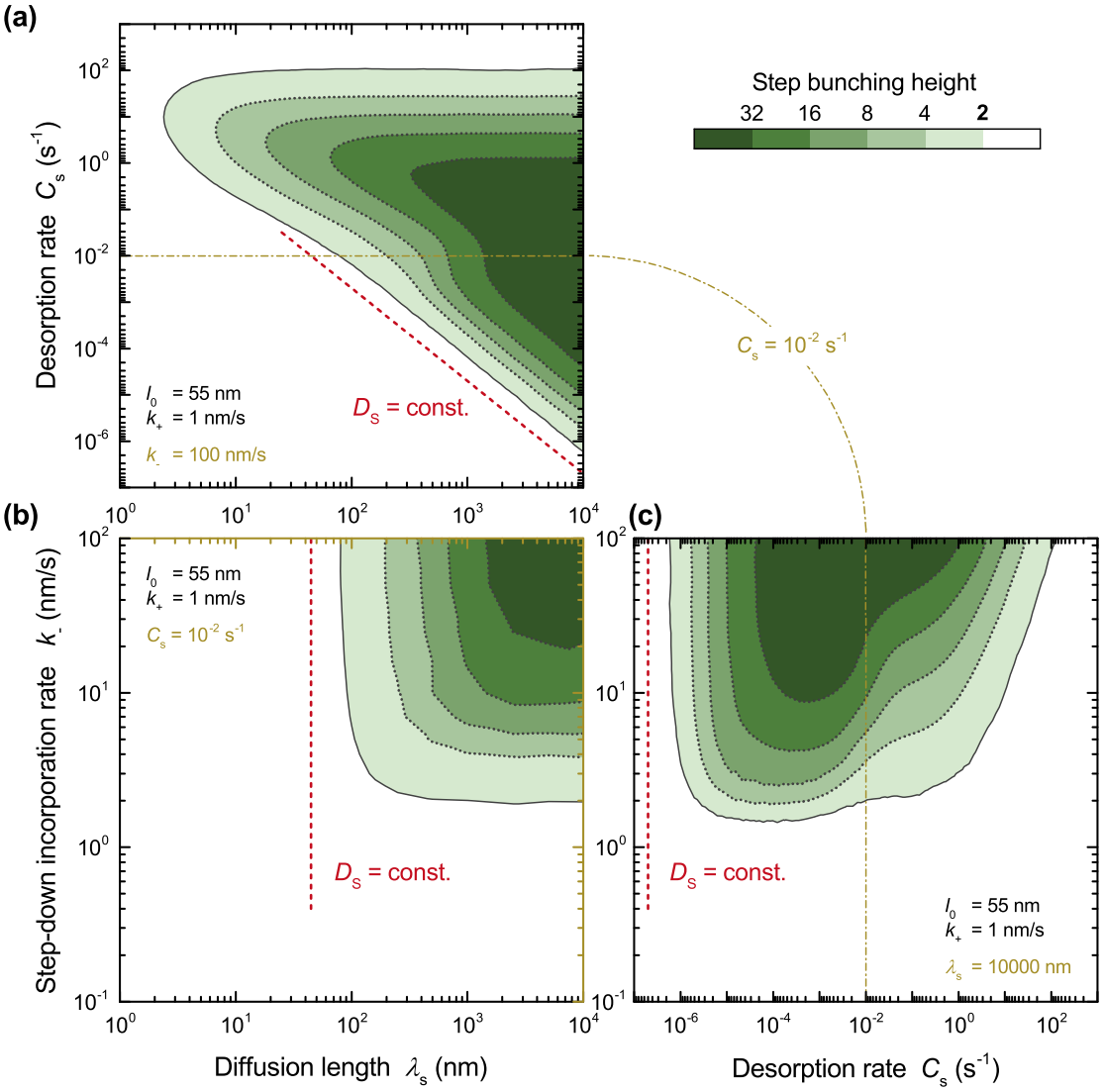


Figure 4.8: Contour plots of the step-bunching height dominating the surface morphology as a function of the diffusion length $\lambda_s$, the step-down incorporation rates $k_-$, and the desorption rate $C_s$ for a fixed terrace width $l_0 = 55\,\text{nm}$ and a fixed step-up incorporation rate $k_+ = 1\,\text{nm/s}$. White contours corresponds to step-flow growth with an average step height below 2 ML, and step-bunching with the step-bunching height color coded in green. The red dashed line highlights a constant diffusion coefficient $D_s$. (a) growth morphology for a fixed step-down incorporation rate $k_- = 100\,\text{nm/s}$. (b) growth morphology for a fixed desorption rate $C_s = 10^{-2}\,\text{s}^{-1}$. (c) growth morphology for a fixed diffusion length $\lambda_s = 10^4\,\text{nm}$.

Another crucial parameter is the desorption rate $C_s$ correlating with all characteristic length, i.e. the diffusion length $\lambda_s$ and the capture lengths $\lambda_\pm$. The influence of the desorption rate on the surface morphology is shown in Fig. 4.8. Again, two major morphology transition regions are investigated correlating with the diffusion length (Fig. 4.8a, $k_- = 100\,\text{nm/s}$) or the incorporation ratio (Fig. 4.8c, $\lambda_s = 10^4\,\text{nm}$). Figure 4.8b

is identical to Fig. 4.7b enabling a direct comparison between both plots. For the limit of a large asymmetric adatom incorporation ratio with $k_- \gg k_+$ (Fig. 4.8a, $k_- = 100\,\mathrm{nm/s}$) step-flow growth is obtained above a certain threshold desorption rate $C_\mathrm{s} > 10^2\,\mathrm{s}^{-1}$. In this case, the adatom density is dominated by the desorption process and the adatom incorporation is independent from the terrace width. For desorption rates below a threshold $C_\mathrm{s} < 10^2\,\mathrm{s}^{-1}$, the morphology transition appears to be controlled by the surface diffusion coefficient $D_\mathrm{s}$ (indicated by a red dashed line in Fig. 4.8). In this case with a low desorption rate enabling significant adatom incorporation, the adatom diffusion distance is limited by the nucleation sites, which are terrace step-edges. At a constant diffusion length, a reduction of the desorption rate is associated with an increase of the capture lengths $\lambda_\pm$. All adatoms are incorporated and the adatom density is pinned to zero at the upper and lower terrace step-edge (Eq. 4.7) leading to a symmetric adatom density profile and step-flow growth is obtained. This transition is independent of the desorption rate and step-down incorporation rate as long as all adatoms are incorporated ($C_\mathrm{s} < 10^{-2}\,\mathrm{s}^{-1}$) and a symmetric adatom density profile exist. A similar observation appears in the limit of a large diffusion length $\lambda_\mathrm{s} = 10^4\,\mathrm{nm}$ (Fig. 4.8c), where a threshold desorption rate $C_\mathrm{s} > 10^{-6}\,\mathrm{s}^{-1}$ is necessary to obtain an asymmetric adatom density profile (Eq. 4.7) yielding step-bunching growth. Above a certain desorption rate $C_\mathrm{s} > 10\,\mathrm{s}^{-1}$ and depending on the incorporation ratios, step-flow growth is obtained. This indicates a change of the dominating surface process from adatom incorporation to adatom desorption. For layer growth with a dominating atom incorporation, step-flow growth is obtained for low adatom diffusivity independent of the Ehrlich-Schwoebel barrier. If the adatom diffusivity is high and all adatoms are incorporated at the terrace edges, a positive or even a very small inverse Ehrlich-Schwoebel barrier ($k_- < 2k_+$) promotes step-flow growth.

Independent of the growth conditions, the vicinal terrace width $l_0$ can be varied by the substrate offcut angle $\alpha_\mathrm{offcut}$. This enables the grower to control the growth morphology by shifting the transition window. Figure 4.9 illustrates the influence of the vicinal terrace width on the phase transition between step-flow growth and step-bunching growth as a function of diffusion length $\lambda_\mathrm{s}$ and step-down incorporation rate $k_-$ for a constant step-up incorporation rate of $k_+ = 1\,\mathrm{nm/s}$ and desorption rate of $C_\mathrm{s} = 10^{-2}\,\mathrm{s}^{-1}$. The data of Fig. 4.7b and 4.8b with a terrace width of $l_0 = 55\,\mathrm{nm}$ is colored in green. In order to apply the theoretical data to the experimental observations in Chapter 4.4, the presented terrace widths are $l_0 = 55\,\mathrm{nm}$, $80\,\mathrm{nm}$, and $120\,\mathrm{nm}$ plotted in green, yellow, and blue, respectively. The growth morphology transition is again characterized by two

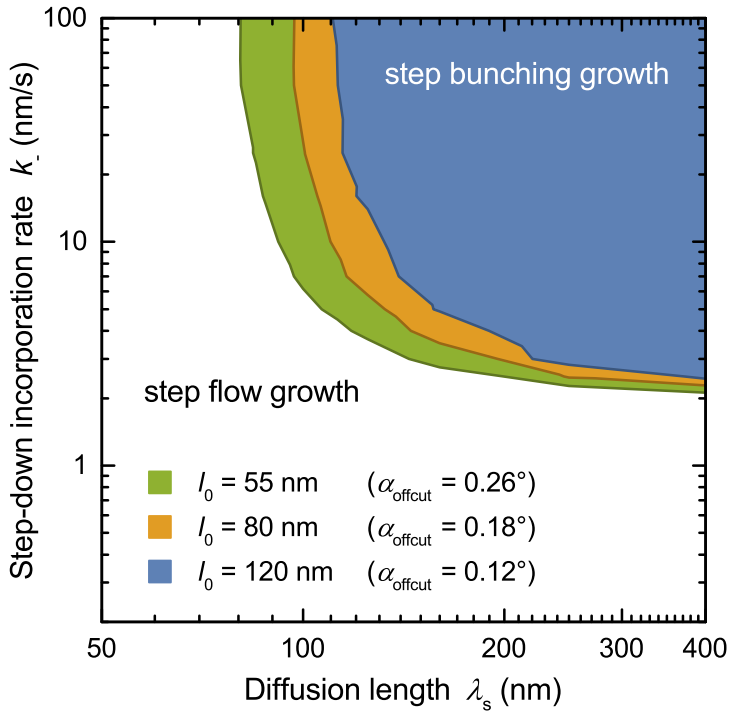


Figure 4.9: Contour plot of the step-flow growth to step-bunching growth transition for different average terrace widths ($l_0 = 55\,\text{nm}$ green, $l_0 = 80\,\text{nm}$ orange, and $l_0 = 120\,\text{nm}$ blue).

different regions. If the diffusion length is very large, all adatoms on the terrace are incorporated independent of the terrace width and the growth morphology transition is only limited by the incorporation ratio with $k_- < 2k_+$ for step-flow growth. For very large inverse Ehrlich-Schwoebel barriers with $k_- \gg k_+$, the growth morphology transition correlates with the adatom diffusivity $D_s$ as discussed for Fig. 4.8a. In this case, the asymmetry of adatom incorporation highly depends on the terrace width. Therefore, step-flow growth is maintained for large terraces (small substrate offcuts) even if an inverse Ehrlich-Schwoebel barrier exists, which is common for high temperature growth conditions of AlN growth [126].

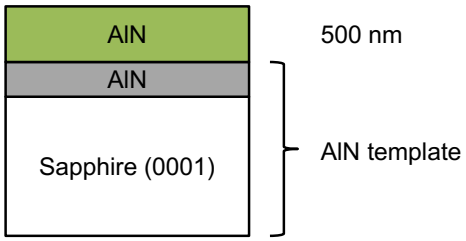


Figure 4.10: AlN sample structure

| | $\alpha_{\mathbf{offcut}}$ (°) | $T_{\mathbf{pyro}}$ (°C) | $\phi_{\mathbf{TMAl}}$ ($\mu$mol/min) | $p_{\mathbf{Al}}$ (Pa) | $\phi_{\mathbf{NH_3}}$ (sccm) | $p_{\mathbf{N}}$ (Pa) | $V/III$ |
|---|---|---|---|---|---|---|---|
| **AlN** | 0.12 – 0.26 | 1200 | 50.0 | 2.8 | 3 – 50 | 8 – 125 | 3 – 44 |

Table 4.1: Important growth parameters (For partial pressures $p_i$ complete pyrolysis is assumed)

## 4.3 Sample structure and growth conditions

The pseudo-homoepitaxial growth of AlN (0001) is investigated by metalorganic vapor-phase epitaxy on AlN templates. They are based on (0001) sapphire substrates and provided by Viola Küller [126]. The vicinal terrace width is controlled by the substrate offcut $\alpha_{\text{offcut}}$ varying between 0.1° and 0.3°. For AlN with a monolayer thickness of 0.25 nm, the vicinal terrace width varies from about 50 to 150 nm. The key growth parameters are shown in Table 4.1 and the layer stack is illustrated in Fig. 4.10. Further growth conditions are described in Chapter 3.1. By growing three one quarter wafers with different substrate offcuts at the same time, the influence of the substrate offcut can be studied for the same growth conditions. Changing the V/III ratio between 3 and 44 via the ammonia supply allows controlling surface diffusion rates for adatoms at a constant growth rate of 1 $\mu$m/h, i.e. with a constant material supply flux $J$. This allows changing the chemical potential of nitrogen by 0.35 eV (Fig. 2.5), which is about 10% of the entire range (Fig. 2.4). By growing AlN layers of about 500 nm in thickness, an influence of the template morphology can be excluded.

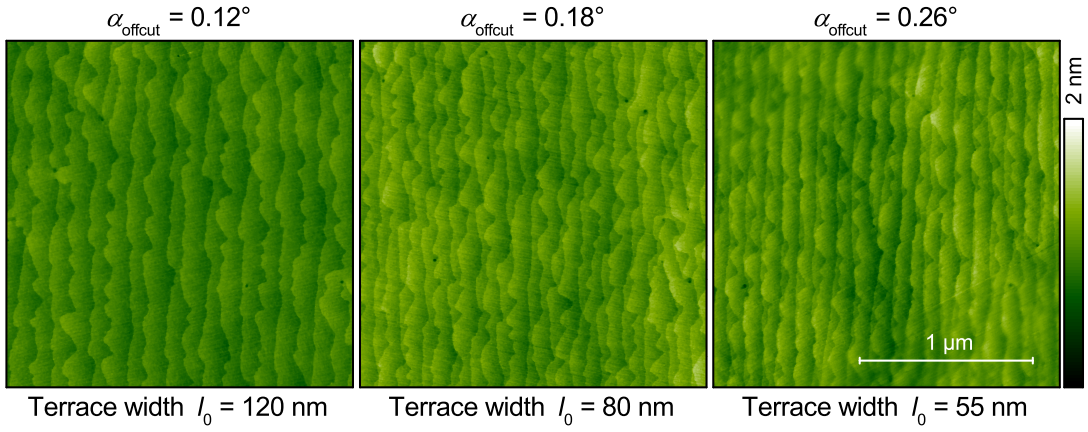


Figure 4.11: AlN (0001) surface morphologies of samples with different offcut values observed by atomic force microscopy.

## 4.4 Pseudo-homoepitaxial growth of AlN

Three different wafers with unique substrate offcut angles were selected to investigate the influence of the terrace width and the growth conditions on the obtained growth morphology. Figure 4.11 exhibits the surface morphology of AlN with step-flow growth for the three different offcut angles of interest. All of them are characterized by monolayer high terraces, which highlight the correlation between the terrace width and the substrate offcut (Chapter 2.2.1). The average vicinal terrace widths determined by atomic force microscopy of $l_0 = (113 \pm 11)$ nm, $(74 \pm 7)$ nm, and $(47 \pm 4)$ nm agree well with the values obtained with X-ray diffraction of respective $\alpha_{\text{offcut}} = (0.12 \pm 0.02)°$, $(0.18 \pm 0.02)°$, and $(0.26 \pm 0.02)°$. All samples show an alternating terrace edge sequence of a smooth and a rough terrace edge. This is related to the nature of the wurtzite crystal and its alternating dangling bond orientation of the tetrahedral nanostructure resulting in different growth speeds for one or two dangling bonds per atom [128, 144]. The different growth speeds of the terrace edges are highly pronounced for the highest substrate offcut with $\alpha_{\text{offcut}} = 0.26°$. In this case, even a partial formation of double monolayer steps can be obtained, which is independent to the discussed step-bunching.

The surface morphology obtained by atomic force microscopy of the homoepitaxial growth at various V/III ratios on three different wafers is shown in Fig. 4.12. Each column corresponds to the same substrate offcut and each row exhibits the surface morphology obtained at the same V/III ratio. All images are plotted with the same height scale of 5 nm highlighting the two different types of surface morphology with the strong contrast for step-bunching growth. The high resolution of individual surface steps in each image

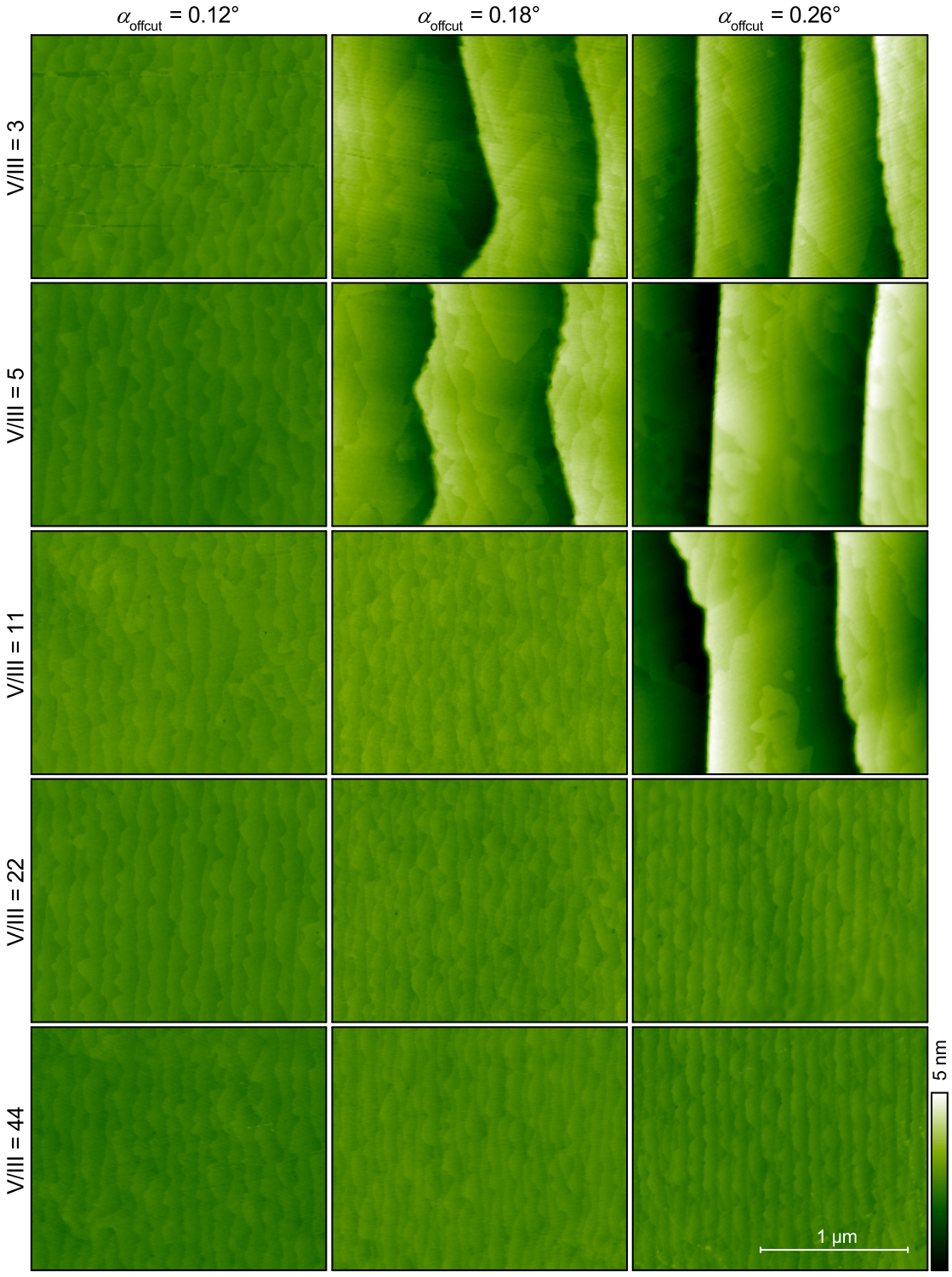


Figure 4.12: AlN (0001) surface morphologies observed by atomic force microscopy. Each row presents the growth at the same V/III ratio. The three columns exhibit the different substrate offcut values.

allows for detailed analysis. Step-flow growth is characterized by individual monolayer steps, whereas step-bunching growth contains macro steps as well. For V/III ratios above 11, all samples exhibit step-flow growth. It is even maintained for V/III ratios below 11 with a substrate offcut value of $\alpha_{\text{offcut}} = 0.12°$, which does not show any step-bunching growth in the entire investigated parameter range. Step-bunching growth is observed for large offcut values $\alpha_{\text{offcut}} > 0.12°$. Although the step-flow growth to step-bunching growth transition for V/III<11 is obtained between 0.12° and 0.18°, this transition is shifted to higher offcut angles between 0.18° and 0.26° for a V/III=11. For the step-bunching morphology with a macroscopic step-bunching height of about 5 nm, the macro steps are most likely formed by m-facets, even though they appear to be parallel for the highest offcut angle $\alpha_{\text{offcut}} = 0.26°$ and zigzag for the intermediate offcut angle $\alpha_{\text{offcut}} = 0.18°$. This can be explained by an additional unintended azimuthal offset of the lateral offcut direction. Indeed, XRD measurements of both samples show a difference of the intended lateral offcut direction of almost 30°, i.e. the horizontal axis of Fig. 4.12 is parallel to the $\vec{m}_{\text{AlN}}$-direction for $\alpha_{\text{offcut}} = 0.12°$ and 0.26°, and parallel to the $\vec{a}_{\text{AlN}}$-direction for $\alpha_{\text{offcut}} = 0.18°$. As theoretically demonstrated with the simulated growth morphologies by the Monte-Carlo approach (Chapter 4.2), the growth transition correlating with the V/III ratio could be explained by a change of the Ehrlich-Schwoebel barrier from positive for V/III>11 to inverse for V/III<11. Additionally, step-flow growth can be maintained for large terrace width ($l_0 = 120\,\text{nm}$) even if typical step-bunching conditions are selected. The growth transition correlating with the terrace width is apparently related to a finite adatom diffusivity on the terrace yielding step-flow growth for $l_0 = 120\,\text{nm}$ and step-bunching growth for $l_0 = 80\,\text{nm}$ and 55 nm. This explanation applies for all V/III<11 due to the limited range of the investigated substrate offcuts. As discussed for the Monte-Carlo results (Chapter 4.2), the morphology transitions are influenced by all surface diffusion rates, like the diffusion coefficient $D_{\text{s}}$ and the incorporation rates $k_{\pm}$. Therefore, it is impossible to derive explicit values for each. However, the data suggest a discrete change of the surface rates at about V/III=11.

According to density functional theory calculations by Northrup et al. [82], a change of the chemical potential of nitrogen can lead to a change of the surface reconstruction (Chapter 2.1.3). During the growth the chemical potential is controlled by the partial pressures of the educts. By keeping the growth rate constant, a group-III limited growth requires a constant group-III partial pressure. Therefore, the ammonia supply is varied and expressed by the V/III ratio. For the growth experiment, the V/III ratio is varied over more than one order of magnitude at a growth temperature of $T_{\text{growth}} = 1500\,\text{K}$ resulting

in a change of the chemical potential of $\Delta\mu = 0.35\,\mathrm{eV}$ (Chapter 2.2.2). This large change of the chemical potential may allow switching between a nitrogen-terminated surface, and an aluminum-terminated surface (Chapter 2.1.3). The diffusion coefficient $D_\mathrm{s}$ correlates with the surface reconstruction yielding a higher diffusion coefficient for an aluminum-terminated surface compared to a nitrogen-terminated surface reconstruction [98]. The lack of step-bunching growth for high V/III ratios V/III$>$ 11 (Fig. 4.12) is associated with a small diffusion constant correlating with a nitrogen-terminated surface. Likewise for the low V/III ratios V/III$<$ 11, an aluminum-terminated surface might be obtained. The V/III ratio of V/III=11 with a small shift of the step-flow growth to step-bunching growth transition, might be related to a rather smooth transition of the two surface reconstructions. Additionally, the incorporation rates at the upper and lower terrace step-edge will be correlated with the surface reconstruction as well. Therefore, no quantitative information about the surface rates ($D_\mathrm{s}$, $k_\pm$) can be extracted by comparing the Monte-Carlo simulations and the experiment.

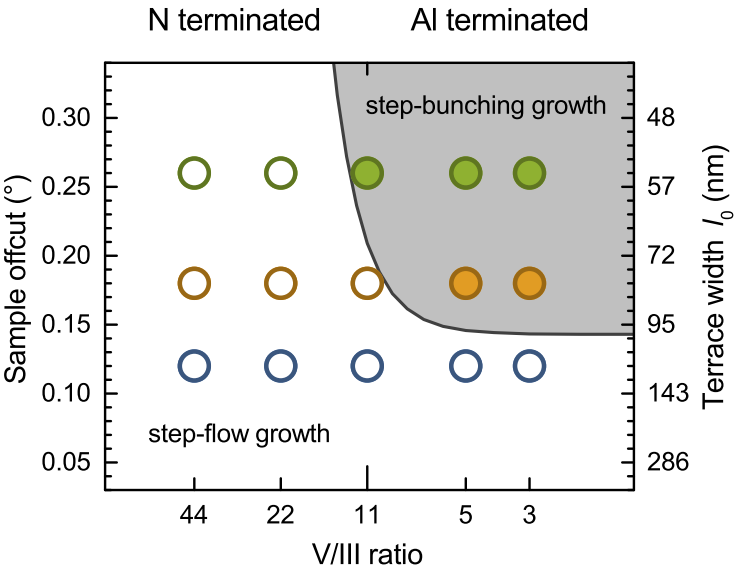


Figure 4.13: Phase diagram of the morphology transition between step-flow growth (open circles) and step-bunching growth (filled circles) of the AlN surfaces obtained from atomic force microscopy (colors correspond to Monte-Carlo results of Fig. 4.9). Two different surface reconstructions can be assigned.

## 4.5 Conclusion

In this chapter, smooth step-flow AlN (0001) surfaces are achieved by theoretically and experimentally investigating the homoepitaxial growth morphology transition between step-flow growth and step-bunching growth. The presented analytical model describes adatom densities with correlating adatom fluxes on uniform terraces. This does not allow deriving any straight indication for the developing growth morphology. Therefore, the influence of a dynamic terrace width is studied via a novel Monte-Carlo approach. This yields surface morphologies allowing to distinguish between step-flow growth and step-bunching growth. For layer growth with a dominating atom incorporation, step-flow growth is obtained for low adatom diffusivities independent of the Ehrlich-Schwoebel barrier. If the adatom diffusivity is high and all adatoms get incorporated at the terrace edges, a positive or even a very small inverse Ehrlich-Schwoebel barrier ($k_- < 2k_+$) promotes step-flow growth. Figure 4.13 summarizes the experimental and theoretical observations. The growth morphology can be controlled via the growth parameters, e.g. V/III ratio, to switch between different surface reconstructions promoting or inhibiting step-bunching growth. Additionally, the favored step-flow growth can be maintained by choosing a small substrate offcut angle even under conditions typically promoting step-bunching growth.

# 5 Desorption induced GaN quantum dot growth

In the literature, GaN quantum dot growth is often performed with a growth interruption, which allows approaching equilibrium conditions. For an approach with a stable energy minimum based on thermodynamical energy balance, the system is supposed to yield a stable morphology with pure adatom diffusion. The common modified Stranski-Krastanow growth employs a growth interruption to finally transform quantum dots out of a two-dimensional layer. This technique is reported for two major epitaxial growth methods of molecular beam epitaxy [43–57]. Typical quantum dots of gallium-rich plasma-assisted molecular beam epitaxy are about $(3-5)$ nm high and $(10-30)$ nm in diameter with a density of $(3-20)\cdot10^{10}\,\mathrm{cm}^{-2}$ [47–49]. Capped quantum dots luminesce at $(2.5-3.8)$ eV [51,53]. For ammonia-assisted molecular beam epitaxy, typical quantum dots are about $(1-3)$ nm high and $(10-20)$ nm in diameter with a density of $(10-50)\cdot10^{10}\,\mathrm{cm}^{-2}$ [54, 55, 57, 145]. Capped quantum dots luminesce at $(2.0-3.0)$ eV [55, 146]. In 2002, Miyamura et al. achieved GaN quantum dots with metalorganic vapor-phase epitaxy by a growth interruption of 30 s after the growth of GaN under a very high V/III ratio of 11500 at 975°C [58, 147]. Low density quantum dots of $10^8\,\mathrm{cm}^{-2}$ are achieved with large diameters of about 35 nm and small heights of about 1.6 nm yielding very small aspect ratios below 0.1. Many studies show a reduction of quantum dot size with increasing growth interruption time indicating desorption as a significant influence. This is a well known process for surface treatment [148–150]. Due to the stochastic adatom evaporation, the islands will end up with very different shapes and sizes. This large inhomogeneity makes controlling the desired properties difficult. Still, three-dimensional structures can be realized offering efficient exciton confinement necessary for quantum device properties.

In this chapter the formation of GaN quantum dots is studied by growing a two-

dimensional GaN layer on AlN with a subsequent growth interruption. In this case, desorption is one of the key driving forces of quantum dot formation. With a thickness of 2.5 nm, the GaN layer thickness is below the critical thickness for plastic relaxation ($l_{\mathrm{crit}}$ (GaN/AlN) = 3 nm [54, 151]) to prevent defect formation. The morphological evolution is studied for various desorption times at different temperatures allowing to determine an activation energy for the desorption process, which is compared to the literature. Additionally, optical properties of capped desorption induced GaN quantum dots are investigated via micro-photoluminescence to demonstrate the feasibility of the approach.

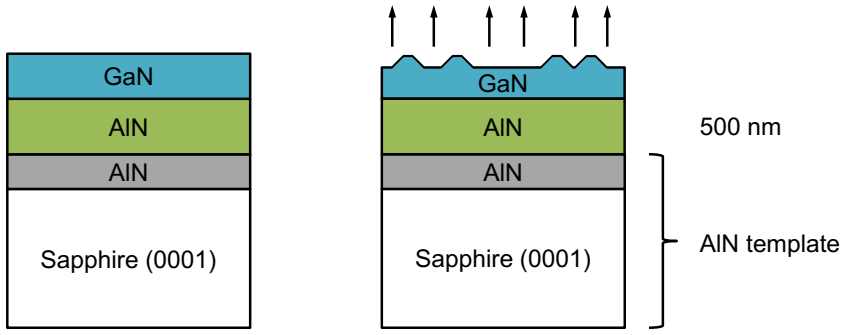


(a) GaN sample structure (b) Desorption step enabling 3D structures

Figure 5.1: Desorption induced GaN quantum dot sample structure

| | $T_{\mathbf{pyro}}$ (°C) | $\phi_{\mathbf{TMAl}}$ ($\mu$mol/min) | $p_{\mathbf{Al}}$ (Pa) | $\phi_{\mathbf{TMGa}}$ ($\mu$mol/min) | $p_{\mathbf{Ga}}$ (Pa) | $\phi_{\mathbf{NH_3}}$ (sccm) | $p_{\mathbf{N}}$ (Pa) | $V/III$ |
|---|---|---|---|---|---|---|---|---|
| **AlN** | 1050 | 35.5 | 2.0 | | | 100 | 250 | 125 |
| **GaN** | 750 – 850 | | | 3.7 | 0.2 | 100 | 250 | 1200 |

Table 5.1: Important growth parameters (For partial pressures $p_i$ complete pyrolysis is assumed.)

## 5.1 Sample structure and growth conditions

The heteroepitaxial growth of GaN on AlN was performed on (0001) AlN/sapphire templates provided by Viola Küller [126]. First, an AlN buffer layer is grown to provide a clean smooth AlN surface for GaN nucleation independent of any surface modifications of the AlN templates. The following GaN layer with 10 ML in thickness is used as a basis to study the desorption process. The key growth parameters are shown in Table 5.1 and the growth is illustrated in Fig. 5.1. Further growth conditions are described in Chapter 3.1. Right after the GaN growth the ammonia was switched off for different time frames and re-offered during the cool-down process of the sample to stabilize the surface. The growth interruption time $t_{\mathrm{GRI}}$ is varied between 0 s and 240 s at different temperatures $T_{\mathrm{pyro}} = (750 - 850)$°C, which are in-situ measured with a pyrometer.

## 5.2 Morphological results of uncapped samples

The growth of GaN was performed with a relatively high V/III ratio of 1200 yielding two-dimensional layer-by-layer growth. A detailed growth study of the GaN evolution with time can be found in Chapter 6. Figure 5.2 ($t_{\mathrm{GRI}} = 0\,\mathrm{s}$) shows the surface morphology of the initial GaN layer. It exhibits a terraced surface with very rough terrace edges, which might be related to the high threading-dislocation density on the order of $10^{10}\,\mathrm{cm}^{-2}$. The layer thickness of 10 ML GaN is estimated by a growth rate calibration of a thick reference sample and later on evaluated by the desorption process itself. Different growth rates and growth temperatures in the presented range yield very similar surface morphologies to Fig. 5.2 ($t_{\mathrm{GRI}} = 0\,\mathrm{s}$). Additionally, no change of the surface morphology could be observed for the case when the samples were exposed to a growth interruption maintaining ammonia flow. This allows to neglect any influences of the cool-down process if ammonia is applied. The desorption of GaN is in the following investigated in the absence of ammonia as a function of growth interruption time and temperature.

### 5.2.1 Influence of growth interruption time

Right after the growth of a 10 ML thin GaN layer ($t_{\mathrm{growth}}$=35 s) a growth interruption of $t_{\mathrm{GRI}} = (0-240)\,\mathrm{s}$ is applied with no ammonia in the surrounding vapor-phase. The surface morphology of an area of 1x1 $\mu\mathrm{m}^2$ is shown in Fig. 5.2 which is measured by atomic force microscopy. Right after $t_{\mathrm{GRI}} = 10\,\mathrm{s}$ the surface is mainly covered by hexagonally shaped islands. For longer interruption times, the size of the structures becomes smaller and smaller (Fig. 5.2, $t_{\mathrm{GRI}} = (30-120)\,\mathrm{s}$) until they eventually disappear. At $t_{\mathrm{GRI}} = 240\,\mathrm{s}$ no islands are observed and the surface morphology has changed to smooth step-flow, which is typical for the underlying AlN layer. It appears that large irregular islands (Fig. 5.2, $t_{\mathrm{GRI}} = 30\,\mathrm{s}$) split up over time yielding multiple smaller islands (Fig. 5.2, $t_{\mathrm{GRI}} = 60\,\mathrm{s}$). Additionally, the remaining islands appear to be attached to the underlying terrace step (Fig. 5.2, $t_{\mathrm{GRI}} = 120\,\mathrm{s}$) offering a favored energetic situation with slight strain relaxation. This can be realized due to additional surface bonds at the terrace edge or even at kink positions.

For further understanding, the islands have been characterized quantitatively. The height and diameter distribution as a function of the growth interruption time is shown in Fig. 5.3a. In general, all samples exhibit a very large inhomogeneity in height and diameter with standard deviations of $\Delta h = \pm 2\,\mathrm{nm}$ and $\Delta d = \pm 80\,\mathrm{nm}$, respectively.

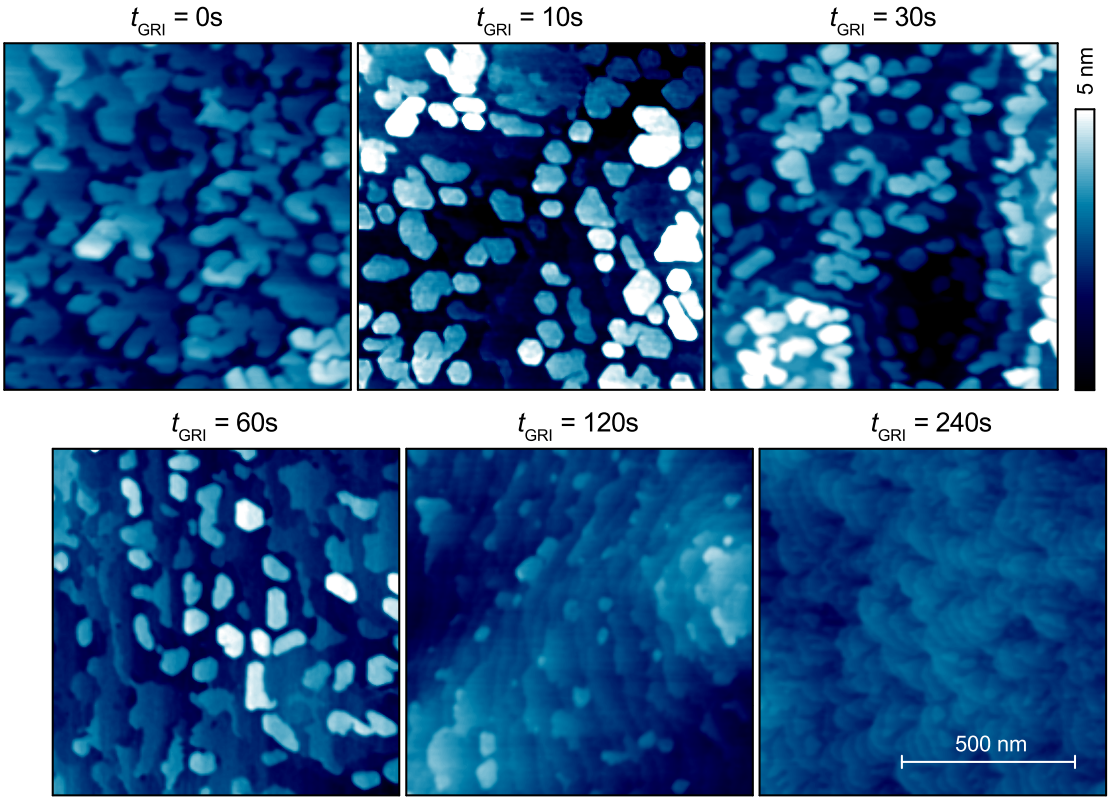


Figure 5.2: GaN surface morphologies observed by atomic force microscopy of samples grown at $T_{\mathrm{pyro}} = 789°\mathrm{C}$ after different growth interruption times $t_{\mathrm{GRI}}$.

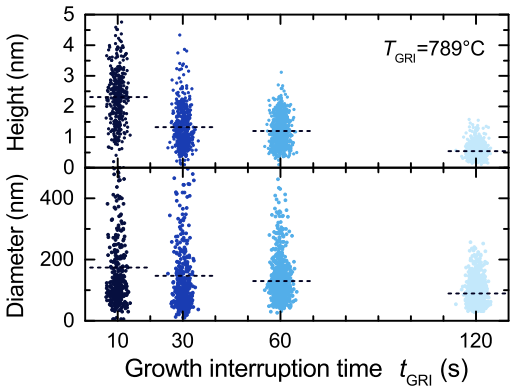


(a) Height and diameter distribution of 3D structures as function of growth interruption time $t_{\mathrm{GRI}}$. Dashed lines mark mean value.

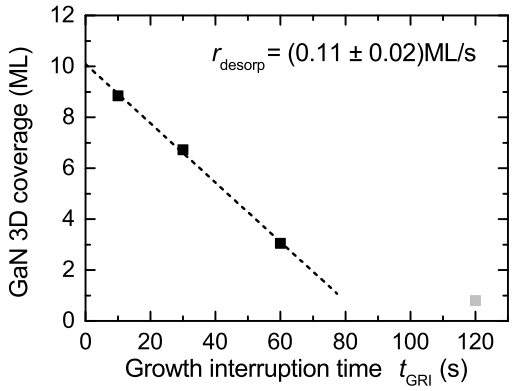


(b) Linear fit of equivalent GaN layer coverage as function of growth interruption time $t_{\mathrm{GRI}}$ illustrate material desorption.

Figure 5.3: Detailed quantitative analysis for growth interruption time $t_{\mathrm{GRI}}$ with no ammonia present at a temperature of $T_{\mathrm{GRI}} = 789°\mathrm{C}$.

Especially, the sample with a growth interruption of only $t_{\mathrm{GRI}} = 10\,\mathrm{s}$ yields islands which are almost 5 nm high. This suggests that at the early stage of the growth interruption

GaN material is redistributed over the sample. This might be again due to a favored energetic situations on top of the islands, where GaN is able to relax into the surrounding vapor-phase reducing the internal strain. The average height and diameter is decreasing with further growth interruption time evidencing desorption as a significant influence. By evaluating the overall three-dimensional coverage as a function of growth interruption time (Fig. 5.3b), a linear decrease of surface coverage can be observed until $t_{\mathrm{GRI}} = 80\,\mathrm{s}$. The desorption rate is $r_{\mathrm{desorp}} = (0.11 \pm 0.02)\,\mathrm{ML/s}$. It shall be noted, that the last point with $t_{\mathrm{GRI}} = 120\,\mathrm{s}$ (Fig. 5.3b gray dot) was excluded due to the difference of the surface energies of GaN and AlN, which will reduce the desorption rate of the very last monolayers. The desorption induced GaN quantum dots can be tailored for common quantum dot sizes. However, they share very low aspect ratios of $< 0.1$ and the size distribution is more inhomogeneous than typical Stranski-Krastanow quantum dots (Chapter 6).

### 5.2.2 Influence of temperature

Even though a small material redistribution during the very early seconds could be found, the GaN morphology is primarily influenced by desorption. This process is a thermally activated process and, therefore, highly temperature dependent. The activation energy of this process can be determined by investigating the surface coverage as a function of the desorption temperature. Therefore, the surface morphology after 10 s of desorption is investigated at six different temperatures and shown at Fig. 5.4. For temperatures below $T_{\mathrm{pyro}} = 780°\mathrm{C}$, no or very little island formation could be observed. The surface morphology is very close to the original GaN morphology shown in Fig. 5.2 ($t_{\mathrm{GRI}} = 0\,\mathrm{s}$). For temperatures above $T_{\mathrm{pyro}} = 780°\mathrm{C}$, a clear island formation can be observed with smaller islands for higher temperatures. Typical for temperature activated processes, higher temperatures increase the speed of reaction kinetics. Thus, the surface morphology influenced by temperature yields a similar picture compared to the influence of the desorption time at one specific temperature. In order to determine the activation energy for the GaN desorption without ammonia present, a quantitative analysis of the GaN coverage is necessary. Figure 5.5a exhibits the height and diameter distribution as a function of desorption temperature after a growth interruption of $t_{\mathrm{GRI}} = 10\,\mathrm{s}$. The GaN coverage on the surface is determined by counting the total volume of all nanostructures. With an initial nominal thickness of 10 ML and after 10 s of desorption, an overall material reduction can be observed with increasing temperature leading to an increase in desorption rate with increasing temperature. A typical Arrhenius fit is

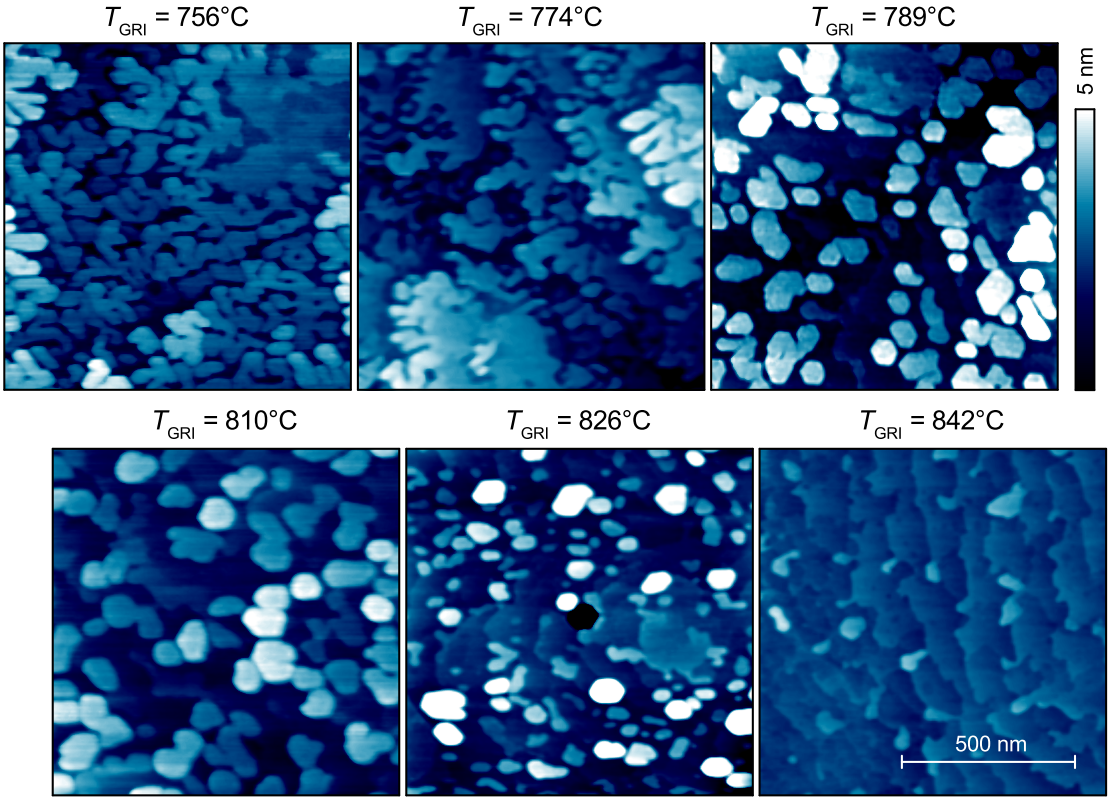


Figure 5.4: GaN surface morphologies for different desorption temperatures $T_{\mathrm{GRI}}$ after a growth interruption of $t_{\mathrm{GRI}} = 10\,\mathrm{s}$ observed by atomic force microscopy.

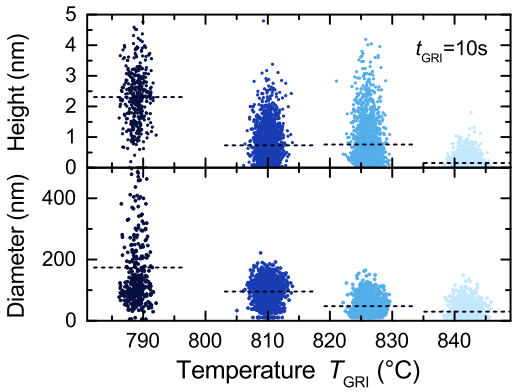


(a) Height and diameter distribution of 3D structures for different desorption temperatures $T_{\mathrm{GRI}}$. Dashed lines mark mean value.

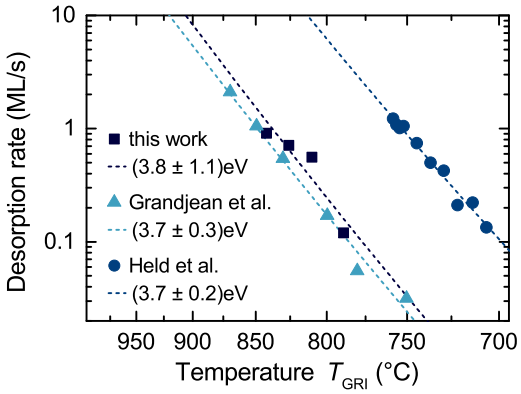


(b) Arrhenius fits of GaN desorption. (Grandjean et al. [149], Held et al. [152])

Figure 5.5: Determination of the activation energy for GaN desorption with no ammonia present.

applied and plotted in Fig. 5.5b. The determined activation energy for GaN desorption of $E_{\mathrm{desorp}} = (3.8 \pm 1.1)\,\mathrm{eV}$ is in good agreement with the literature [149, 152–154].

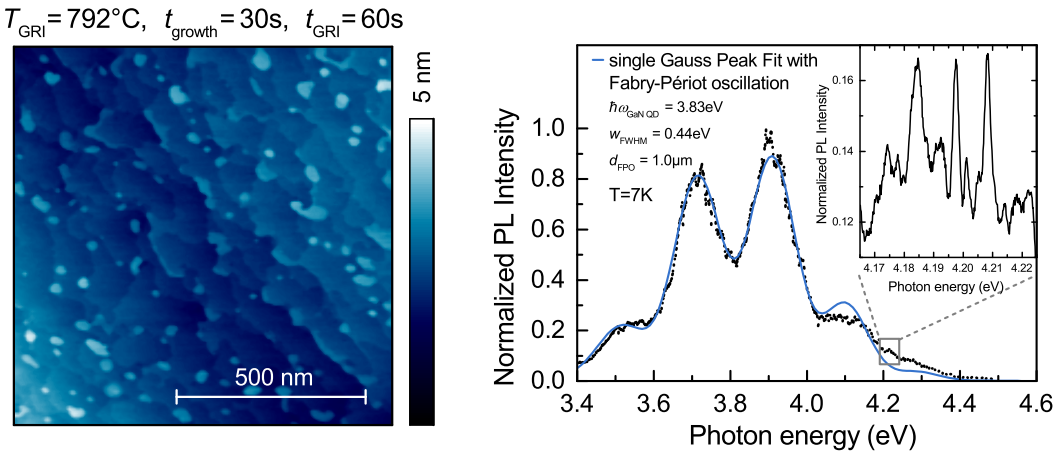


(a) Surface morphology of uncapped GaN quantum dots by desorption.

(b) Ensemble photoluminescence of capped GaN quantum dots at $T = 7\,\mathrm{K}$. Blow up exhibits individual luminescence lines.

Figure 5.6: Structural and optical properties of ensemble GaN quantum dots realized by desorption.

## 5.3 Optical properties of capped samples

A sample containing typical GaN quantum dot structures has been grown at $T_{\mathrm{pyro}} = 792°\mathrm{C}$, $t_{\mathrm{growth}} = 30\,\mathrm{s}$, and $t_{\mathrm{GRI}} = 60\,\mathrm{s}$. Fig. 5.6a exhibits the surface morphology of an uncapped sample. GaN quantum dots with $(1.2 \pm 0.4)\,\mathrm{nm}$ in height and $(30 \pm 15)\,\mathrm{nm}$ in diameter with a density of $1.6 \cdot 10^{10}\,\mathrm{cm}^{-2}$ are observed. The optical properties are investigated of a capped GaN quantum dot sample which is nominally identical to the sample shown in Fig. 5.6a. In order to maintain the desired GaN quantum dot features, the sample was immediately capped after the desorption step with 10 nm AlN grown at the same temperature. Additionally, a 40 nm thick AlN layer was grown at elevated temperatures ($T_{\mathrm{pyro}} = 1040°\mathrm{C}$) to improve structural and optical AlN properties.

An ensemble photoluminescence spectrum measured at a low temperature of $T = 7\,\mathrm{K}$ is shown in Fig. 5.6b. It exhibits a broad luminescence peak at about $\hbar\omega_{\mathrm{GaN\ QD}} = (3.8 \pm 0.2)\,\mathrm{eV}$, which is modulated by a Fabry-Pérot oscillation. The associated Fabry-Pérot oscillation thickness is $d_{\mathrm{FPO}} = 1.0\,\mu\mathrm{m}$ being the total AlN thickness between the two interfaces AlN/sapphire and AlN/air. A different origin of the multiple peaks could be a finite quantum dot height, as done by Simeonov [155]. However, the multiple peaks are almost equally spaced and the peak width fit very well with the Fabry-Pérot oscillation. The peak position of the ensemble luminescence is highly influenced by the quantum confined Stark effect. In the literature, a broad GaN quantum dot emission is

reported from 600 nm (2 eV) [54,146] up to 250 nm (5 eV) [29,156] mainly correlating with the height of the quantum dot. According to Hönig [104], quantum dots with an aspect ratio of 0.1 and a height of about 1.5 nm luminesce at 3.8 eV, which fits to the average quantum dot height and an additional wetting layer. A higher magnification of the ensemble spectrum does already reveal sharp individual luminescence lines well above the noise level (inset of Fig. 5.6b) promising for individual quantum dot excitation. Isolated mesa structures have been processed with diameters down to 150 nm. By applying this technique, the amount of quantum dots inside the mesa is reduced to 1 – 5 quantum dots.

An advanced micro photoluminescence measurement of a representative mesa structure is shown in Fig. 5.7. By combining power and polarization dependent measurements, typical quantum dot excitonic-luminescence features can be observed. Figure 5.7a presents one representative spectrum at 1 mW excitation power without polarization filter. A polarization dependent measurement with an excitation power of 1 mW is shown in Fig. 5.7b. Furthermore, the power dependence of the luminescence features is plotted in Fig. 5.7c without polarization filter. Several distinct luminescence lines with line-widths of about 2 meV can be observed, which are typical for group-III nitride quantum dot samples [105, 106]. All luminescence features exhibit a unique polarization dependence appearing uncorrelated with the sample orientation. During the long integration time of almost 1 h, the luminescence position of one feature is shifting from 4.368 eV to 4.376 eV. This could be related to charge transfers in the vicinity of the luminescence origin [104]. Three different luminescence lines are selected for detailed power and polarization analysis. All three of them exhibit a linear excitation power dependence over at least two orders of magnitude (Fig. 5.7e) associated with single exciton emission. No saturation of the emission power with increasing excitation power could be observed. This indicates too low excitation densities for potential biexciton emission. The two luminescence features at 4.335 eV ($X_1$) and 4.343 eV ($X_2$) exhibit approximately an orthogonal polarization dependence (Fig. 5.7d) which is an indication for originating from the same quantum dot separated by fine-structure splitting (chapter 2.1.4). The energy difference of $\Delta E_{\mathrm{FSS}} = (8.0 \pm 0.4)$ meV is in the range for reported GaN quantum dots [27, 104, 106]. Similar optical results could be obtained on a different mesa structure of the same sample [157]. In this case, an exciton pair at a similar emission energy has a fine-structure splitting of about $\Delta E_{\mathrm{FSS}} = (7.0 \pm 0.4)$ meV. In order to investigate single photon emission, a photon auto-correlation measurement with a Hanbury-Brown & Twiss setup has to be done [106], which is reserved for future experiments.

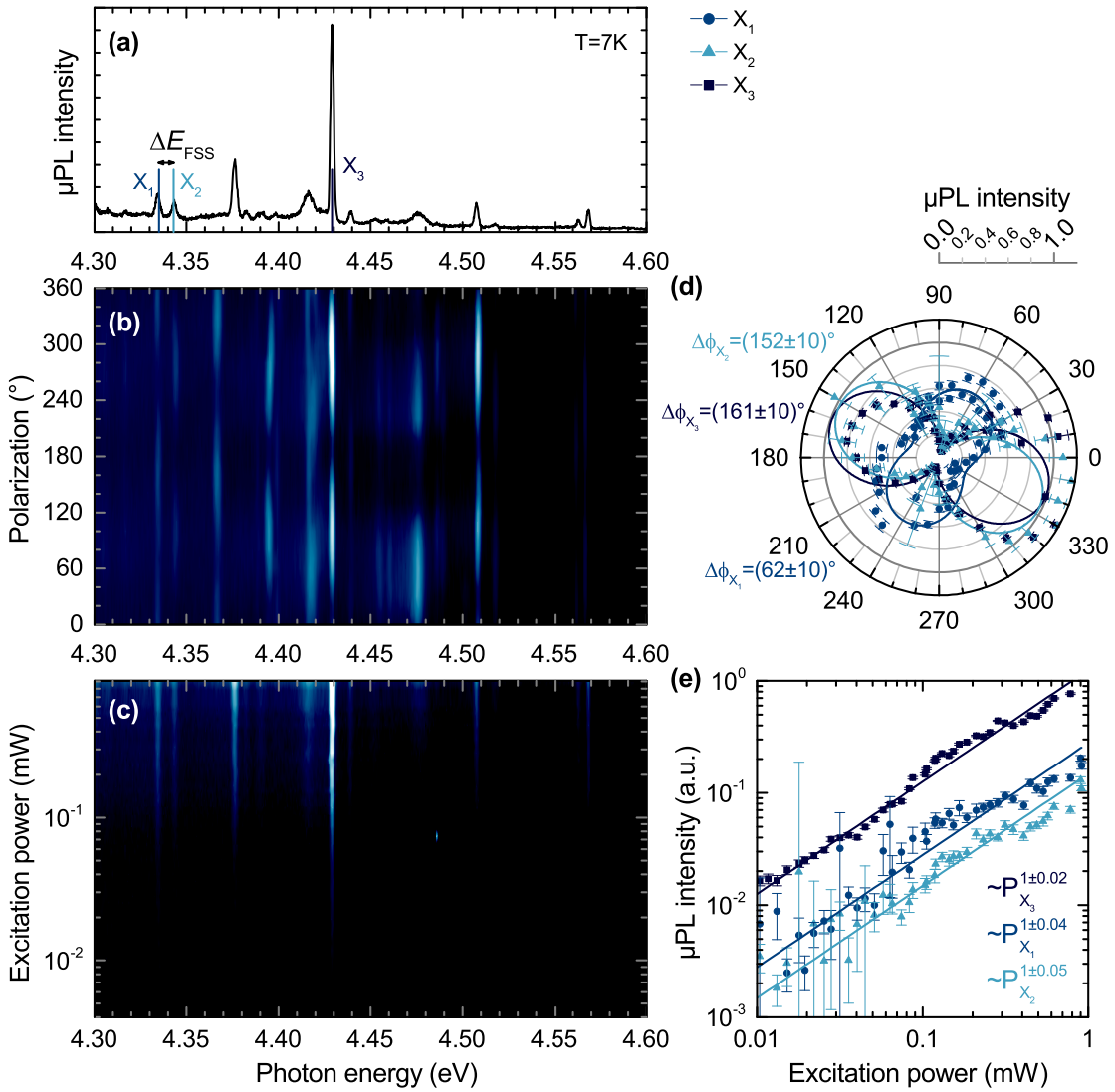


Figure 5.7: Optical properties of desorption induced individually excited GaN quantum dots by micro photoluminescence measurements ($\mu$PL) at $T = 7\,\mathrm{K}$ with frequency-doubled $Ar^{2+}$-ion excitation at $\lambda_{exc} = 244\,\mathrm{nm}$. (a) Representative spectrum at 1 mW without polarizer and marked investigated peaks at 4.335 eV ($X_1$), 4.343 eV ($X_2$), and 4.429 eV ($X_3$). (b) Contour plot of the intensity as a function of photon energy and polarization angle. (c) Contour plot of the intensity as a function of photon energy and excitation power. (d) Polar plot of the intensity as a function of the polarization angle of the investigated peaks. (e) Intensity as a function of the excitation power of the investigated peaks.

## 5.4 Conclusion

It could be demonstrated that GaN quantum dots can be achieved by employing material desorption of a thin two-dimensional GaN layer. The morphology evolution of the desorption process was analyzed as a function of desorption time at different temperatures. The determined desorption energy for GaN is similar to the literature. Typical GaN quantum dot structures are achieved by optimizing the desorption temperature, the initial GaN layer thickness, and the growth interruption time. Due to the stochastic desorption process, quantum dots exhibit a very inhomogeneous size distribution with very small aspect ratios of $< 0.1$. The obtained optical properties of capped desorption induces GaN quantum dots are similar to reported flat elongated GaN quantum dot emission.

# 6 Surface energy induced 2D to 3D transition in GaN

Stranski-Krastanow growth can provide homogeneous defect-free quantum dot structures with excellent optical properties as demonstrated for other material systems [15–17]. The heteroepitaxial growth of GaN on relaxed AlN is an excellent material system to study the growth transition between two-dimensional Frank-van-der-Merve growth and three-dimensional Stranski-Krastanow growth. This transition is typically described by an energy balance between the strain energy and the surface energy. For a large number of material systems, the growth transition is observed at a minimal lattice mismatch of about $\epsilon = 2.5\%$ [41] being very similar to the lattice mismatch between GaN and AlN with $\epsilon_{\mathrm{GaN/AlN}} = 2.4\%$. Consequently, the strain energy is very small and three-dimensional growth of GaN on AlN is very sensitive to changes of the surface energy.

For Frank-van-der-Merve growth, the surface energy dominates the epitaxial process. Therefore, the growth proceeds two-dimensionally to minimize the total surface area. After a certain pseudomorphic layer thickness, the accumulated strain energy is relieved by plastic relaxation, which is accomplished by defect formation. Stranski-Krastanow growth, on the other hand, is characterized by two different stages. At first, the growth is mainly dominated by the interface energy of the heterojunction causing a wetting of the substrate. After a certain wetting layer thickness distinct from the interface, the surface energy is reduced and strain is elastically relieved by the formation of three-dimensional islands at the expense of an increased surface area. This strain relief mechanism limits the island size yielding a uniform size distribution. Therefore, Stranski-Krastanow growth is often desired for optoelectronic devices based on quantum dots. Beyond a maximum island size and density, growth proceeds by plastic relaxation, which is again accomplished by defect formation.

In this chapter, a review of GaN Stranski-Krastanow quantum dot growth is presented. Then, the influence of the surface energy on the growth morphology is studied via a qualitative growth model by Daruka et al. [158] and presented to illustrate the interaction of the surface energy and the strain energy. The model is able to describe the phenomenological observation of three different growth morphologies: pseudomorphic two-dimensional growth, coherently strained islands, and relaxed islands allowing further insights to the physics of quantum dot formation. After the theoretical discussion, the growth morphology is investigated by metalorganic vapor-phase epitaxy changing the V/III ratio, which correlates with the surface energy. First, the sample structure and the growth conditions are presented. Then, the evolution of the surface morphology for high and low V/III ratios are discussed, which yield two-dimensional and three-dimensional growth, respectively. At low V/III ratios, a detailed investigation of the wetting layer thickness as well as the quantum dot shape are performed by analyzing morphological data obtained by atomic force microscopy and transmission electron microscopy. Additionally, the obtained morphology transition in correlation with the surface energy is analyzed in the context of all three common growth techniques and an estimation of the energy budget is presented. Furthermore, capped GaN quantum dots are investigated by the help of mesa structures to present principle optical properties.

## 6.1 Review of GaN quantum dot epitaxy

In the literature, GaN Strankski-Krastanow quantum dot epitaxy on AlN has been studied by three major epitaxial growth methods: plasma-assisted molecular beam epitaxy, ammonia-assisted molecular beam epitaxy, and metalorganic vapor-phase epitaxy. For each growth method, appropriate procedures have been explored to achieve quantum dot growth.

For plasma-assisted molecular beam epitaxy, Daudin et al. [43,44] reported already in 1997 Stranski-Krastanow quantum dot formation at a crucial growth temperature of 720°C [43, 45, 46] and under nitrogen-rich growth conditions [39, 159]. Typical quantum dots are about $(1-4)$ nm high and $(10-20)$ nm in diameter with a density of $(2-5)\cdot 10^{11}\,\mathrm{cm}^{-2}$, and wetting layer thicknesses of about 2.5 ML. Capped quantum dots luminesce at $(2.8-3.8)$ eV. At nitrogen-rich conditions, quantum dot formation is accompanied by an early cluster formation [50], which is interpreted by a kinetically limited adatom diffusion [160]. In order to provide better control of the quantum dot formation, GaN quantum dots have been grown under gallium-rich conditions by employing a Ga bilayer [47–49]. This Ga bilayer inhibits the island formation during deposition. However, applying a proper growth interruption leads to the desired morphology transition with GaN quantum dots and a surrounding wetting layer similar to nitrogen-rich growth conditions. Therefore, this process has been called modified Stranski-Krastanow growth in the literature. Typical quantum dots are about $(3-5)$ nm high and $(10-30)$ nm in diameter with a density of $(3-20)\cdot 10^{10}\,\mathrm{cm}^{-2}$. Capped quantum dots luminesce at $(2.5-3.8)$ eV [51, 53]. Although wetting layer thicknesses of about 2.5 ML have been reported [48], it appears that this wetting layer depends on the growth interruption time. Even no wetting layer may be observed in transmission electron microscopy measurements [52] due to unwetting by possible material desorption.

The growth of GaN quantum dots on AlN by ammonia-assisted molecular beam epitaxy was first studied by Damilano et al. [54, 145] in 1999. The growth temperature of 800°C is certainly higher compared to the quantum dot growth by plasma-assisted molecular beam epitaxy. This might be related to an insufficient ammonia decomposition [101], and may result in different surface conditions for different pyrolytic products. The ammonia-assisted growth proceeds two-dimensionally and pseudomorphically up to 12 ML followed by plastic relaxation [54, 161]. Similar to the Ga bilayer assisted growth, a morphology transition is obtained by the use of a growth interruption. The lack of gallium and

ammonia [57, 162] changes the surface conditions to shift the balance between strain energy and surface energies towards island formation. This transition occurs rather quickly in about 2 s. Additionally, adatom desorption is highly correlated with the ammonia supply at this growth temperature [152, 163]. GaN quantum dots have been achieved at even lower temperatures down to 650°C by adjusting the growth interruption time up to almost 600 s [57]. The presented quantum dot formation via the growth interruption time and the growth temperature yields an activation energy of about 2.4 eV. This value is very close to the formation of a single Ga adlayer associated with the transition between nitrogen-rich and gallium-rich conditions observed for plasma-assisted molecular beam epitaxy $(2.3 \pm 0.1)$ eV [39, 148]. Such change of the surface reconstruction shifts the balance between the strain energy and the surface energies. Typical quantum dots are about $(1-3)$ nm high and $(10-20)$ nm in diameter with a density of $(1-5)\cdot 10^{11}\,\mathrm{cm}^{-2}$. Capped quantum dots luminesce at $(2.0-3.0)$ eV [55, 146]. With ammonia-assisted molecular beam epitaxy, GaN quantum dots have been reported even on $Al_{0.5}Ga_{0.5}N$ [164–166]. In this case, the strain energy is much smaller compared to GaN quantum dots on AlN. This indicates, in addition to the high growth temperature of 800°C, that those structures are realized by material desorption.

The growth of GaN quantum dots on AlN by metalorganic vapor-phase epitaxy was first reported by Miyamura et al. [58, 60, 61] in 2002. Two different approaches have been used. In one approach, the growth of GaN under a very high V/III ratio of 11500 at 975°C is followed by a growth interruption of 30 s to allow for quantum dot formation. Low density GaN quantum dots of $10^8\,\mathrm{cm}^{-2}$ could be achieved with a diameter of about 35 nm and a height of about 1.6 nm [58]. Although a wetting layer thickness of about 1 ML was determined and Stranski-Krastanow growth was claimed, quantum dot formation is most likely dominated by material desorption at those conditions (Chapter 5). In the other approach, GaN quantum dot growth was performed under a very low V/III ratio of 26 at about 965°C leading to quantum dot formation without a growth interruption. Typical quantum dots are about $(2-5)$ nm high and $(10-25)$ nm in diameter with a density of $(3-50)\cdot 10^9\,\mathrm{cm}^{-2}$ and a wetting layer thickness of about 4 ML. Capped quantum dots luminesce at $(2.5-5.0)$ eV [60, 61, 167–169]. A temperature-dependent investigation showed smaller quantum dots at 960°C compared to 975°C, which was interpreted to be surface diffusion dependent. A subsequent growth interruption under high ammonia supply can lead to a ripening of the quantum dots, while a growth interruption under low ammonia supply leads to desorption [147]. Besides the growth temperature, GaN quantum dot growth is very sensitive to the V/III ratio [62, 63, 65].

## 6.2 Qualitative heteroepitaxial growth model

In order to describe the observation of the three main growth morphologies of heteroepitaxy (Frank-van-der-Merve, Stranski-Krastanow, and Volmer-Weber growth), Daruka et al. [158] developed an empirically motivated qualitative growth model. The total energy $u\left(H, n_1, n_2, \epsilon, \gamma\right)$ of a grown layer is characterized by three different energy contributions, which are a two-dimensional fully strained layer $E_{\mathrm{wl}}$ with the material contribution $n_1$, an island term $E_{\mathrm{isl}}$ with the material contribution $n_2$, and a plastically relaxed layer $E_{\mathrm{relaxed}}$ with the material contribution $n_3$:

$$u\left(H, n_1, n_2, \epsilon, \gamma\right) = n_1 E_{\mathrm{wl}}\left(n_1, \epsilon\right) + n_2 E_{\mathrm{isl}}\left(n_2, \epsilon, \gamma\right) + n_3 E_{\mathrm{relaxed}}\left(\epsilon\right) \tag{6.1}$$

with the total deposited material $H = n_1 + n_2 + n_3$, the strain $\epsilon$, and the surface energy $\gamma$. Each contribution is based on the formation energy of chemical bonds $E_{\mathrm{bonds}} = -\Phi_{\mathrm{AA}}$ of the layer atoms A and the strain energy $E_{\mathrm{strain}} = C\epsilon^2$ with $C$ as a material constant considering the elastic modulus and the Poisson ratio. For the two-dimensional case, the simple sum of the formation energy $-\Phi_{\mathrm{AA}}$ and the strain energy $C\epsilon^2$ is extended by a formation energy at the interface $E_{\mathrm{interface}} = -\Phi_{\mathrm{AB}}$ of the substrate material B and the epitaxially grown material A:

$$\begin{aligned} n_1 E_{\mathrm{wl}}\left(n_1, \epsilon\right) = \quad & n_1(C\epsilon^2 - \Phi_{\mathrm{AA}}) \\ + \quad & \int_0^{n_1} \left(\Phi_{\mathrm{AA}} - \Phi_{\mathrm{AB}}\right) \left[\Theta(1-n) + \Theta(n-1)\mathrm{e}^{-\frac{n-1}{a}}\right] \mathrm{d}n \end{aligned} \tag{6.2}$$

with a Heaviside step function $\Theta$ and a decay factor $a$ to describe the interaction width of the interface region. Due to the Heaviside step function $\Theta$, the energy gain for the very first monolayer is defined by the interface bond formation energy $-\Phi_{\mathrm{AB}}$ and will gradually change to the formation energy $-\Phi_{\mathrm{AA}}$. This offers a transition with a wetting layer thickness of at least one monolayer.

The coherently strained island term $E_{\mathrm{isl}}$ again considers the formation energy $-\Phi_{\mathrm{AA}}$ and the strain energy $C\epsilon^2$. However, islands can elastically relax by a relaxation factor $g$. Additionally, an island-specific term considers geometrical changes to a two-dimensional layer:

$$\begin{aligned} n_2 E_{\mathrm{isl}}\left(n_2, \epsilon\right) = \quad & n_2(gC\epsilon^2 - \Phi_{\mathrm{AA}}) \\ + \quad & n_2 E_0 \left(-\frac{2}{x^2} \ln\left(\mathrm{e}^{\frac{1}{2}} x\right) + \frac{\gamma - p\epsilon}{x} + \frac{b\epsilon^2 n^{\frac{3}{2}}}{x^{\frac{3}{2}}}\right) \end{aligned} \tag{6.3}$$

with the energy contribution of the island edges $-\frac{2}{x^2}\left(\ln \mathrm{e}^{\frac{1}{2}}x\right)$ with $x$ as a reduced island size, the contribution of the facets $\frac{\gamma - p\epsilon}{x}$ relieving strain $\epsilon$ at the expense of the formation of additional surface energy $\gamma$ with a coupling factor $p$, and the island interaction $\frac{b\epsilon^2 n^{\frac{3}{2}}}{x^{\frac{3}{2}}}$ considering a strain field in the vicinity of all islands with a coupling factor $b$ in between adjacent islands. In order to match the units of the formation energies and the strain energy with the geometrical part of the island term, all of the quantities ($\Phi_{\mathrm{AA}}$, $\Phi_{\mathrm{AB}}$, $C$) are in units of a characteristic energy $E_0$.

The last possible contribution is a plastically relaxed layer $E_{\mathrm{relaxed}}$. It is only related to the formation energy $-\Phi_{\mathrm{AA}}$ and the strain energy $C\epsilon^2$, which can be partially relaxed by a relaxation factor $g$

$$n_3 E_{\mathrm{relaxed}}(\epsilon) \quad = \quad n_3(gC\epsilon^2 - \Phi_{\mathrm{AA}}). \tag{6.4}$$

The model includes the major contributions to describe the heteroepitaxial growth modes: Frank-van-der-Merve, Stranski-Krastanow, and Volmer-Weber growth. However, many assumptions seem questionable, like only the two-dimensional contribution $E_{\mathrm{wl}}$ considers an interface energy $\Phi_{\mathrm{AB}}$, the same relaxation factor for elastic and plastic relaxation $g$, the partial relaxation of coherent islands, a linear relation between surface energy increase and strain relieve of coherent islands, and the lack of a physical dislocation formation energy. Nevertheless, this model is able to illustrate the very complex situation of the heteroepitaxial growth modes with intuitive phase diagrams.

### 6.2.1 Heteroepitaxial growth as a function of strain

In order to derive a phase diagram containing different growth modes, the total energy of the system has to be minimized for a given parameter set. Each energy contribution of Eq. 6.1 scales differently with the total layer thickness $H$ and the strain $\epsilon$. Therefore, the growth model of Daruka et al. with its ten parameters provides a lot of flexibility to obtain a desired phase diagram (parameter variation in two publications of Daruka et al. [158,170]). Many of the parameters are only physically motivated and no quantitative prediction can be made. However, by choosing all parameters carefully, as Daruka et al. [158,170] presented, a proper phase diagram of all three different growth modes can be obtained as shown in Fig. 6.1a. For small strain values of $\epsilon < 0.05$, two-dimensional Frank-van-der-Merve growth is obtained. After a critical layer thickness, the accumulated strain is plastically reduced by defect generation. For strain values of $0.05 < \epsilon < 0.15$,

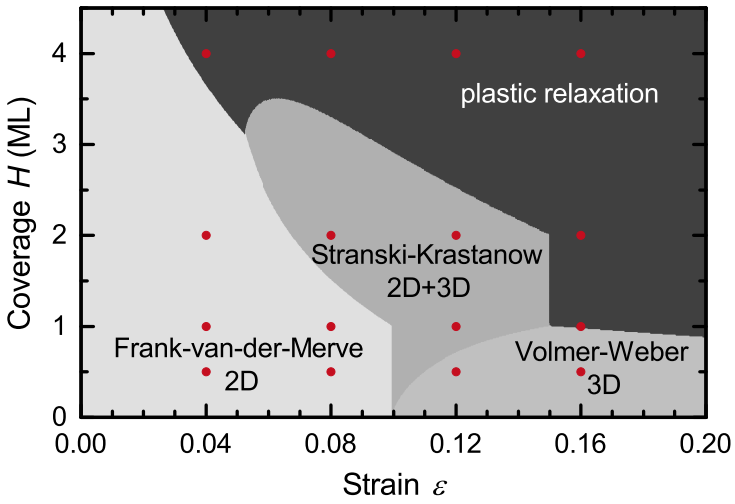


(a) Heteroepitaxial growth modes as a function of strain $\epsilon$ and material coverage $H$ similar to Daruka et al. [158]. Red dots mark ternary diagrams of (b).

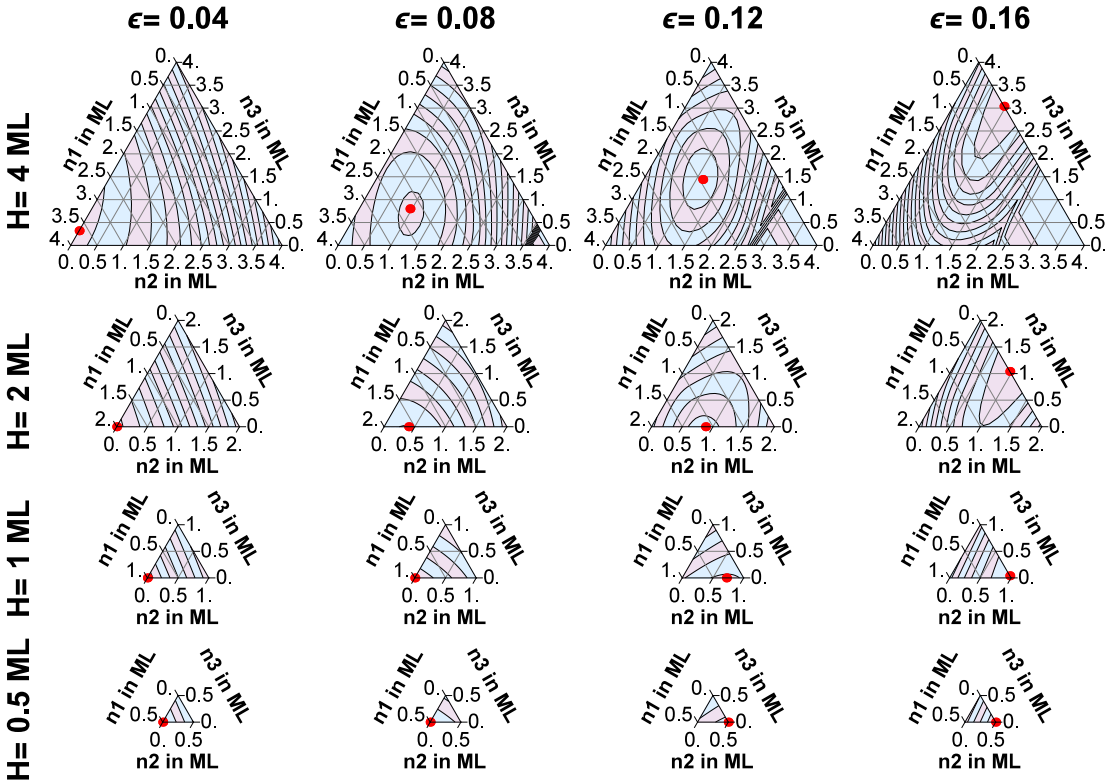


(b) Ternary diagrams of the total energy $u$ as a function of the material distribution $\{n_1, n_2, n_3\}$ at selected material coverage $H$ and strain $\epsilon$ configurations of (a). The red dots mark the energy minima.

Figure 6.1: Phase diagram of heteroepitaxial growth. Parameters: $a = 1$, $C = 40E_0$, $\Phi_{\mathrm{AA}} = E_0$, $\Phi_{\mathrm{AB}} = 1.27E_0$, $g = 0.7$, $p = 4.9$, $\gamma = 1.47$, and $b = 10$ similar to Daruka et al. [158,170].

two different types of three-dimensional Stranski-Krastanow growth are obtained. On one side with $0.05 < \epsilon < 0.10$, coherent island growth is obtained after the growth of a two-dimensional layer, which is the common Stranski-Krastanow growth. On the other side with $0.10 < \epsilon < 0.15$, the growth initiates with coherent islands followed by a mixture of two-dimensional growth and coherent island growth. In both cases, plastic relaxation is again obtained after a critical layer thickness. For large strain values of $\epsilon > 0.15$, only three-dimensional Volmer-Weber growth is obtained proceeding with plastic relaxation after a critical layer thickness of coherent island growth.

In order to generate such a phase diagram, the material distribution has to be calculated for each tuple of material coverage $H$ and strain $\epsilon$ based on the minimization of the total energy. Figure 6.1b illustrates the minimization process of the total energy for 16 different examples. Each ternary contour plot exhibits the total energy as a function of the material distribution with equipotential lines and the energy minimum marked with a red dot.

For a relatively low strain value of $\epsilon = 0.04$ and low material coverage, the energy minimum is obtained at the lower left in the ternary plots of Fig. 6.1b ($\epsilon = 0.04$, $H = 0.5\,\mathrm{ML}$, $n_1 = 0.5\,\mathrm{ML}$, $n_2 = 0\,\mathrm{ML}$, $n_3 = 0\,\mathrm{ML}$), where the total energy $u$ is completely characterized by $n_1 E_{\mathrm{wl}}$ and any contributions of $n_2$ and $n_3$ would increase the total energy. After a certain layer thickness of about $H > 3.7\,\mathrm{ML}$ ($\epsilon = 0.04$, $H = 4.0\,\mathrm{ML}$, $n_1 = 3.7\,\mathrm{ML}$, $n_2 = 0\,\mathrm{ML}$, $n_3 = 0.3\,\mathrm{ML}$), plastic relaxation is favored, which is typically associated with defect formation. This transition is highly correlated with the choice of the amount of plastic relaxation $g$, the decay factor $a$ and the interface bond formation energy $E_{\mathrm{interface}} = -\Phi_{\mathrm{AB}}$ in respect to the bond formation energy $E_{\mathrm{bond}} = -\Phi_{\mathrm{AA}}$.

For a higher strain value of $\epsilon = 0.08$ ($H = 0.5\,\mathrm{ML}$, $n_1 = 0.5\,\mathrm{ML}$, $n_2 = 0\,\mathrm{ML}$, $n_3 = 0\,\mathrm{ML}$), the energy minimum for the first monolayer is again characterized by a two-dimensional wetting layer with $n_1 E_{\mathrm{wl}}$. After a certain layer thickness of about $H > 1.5\,\mathrm{ML}$ ($\epsilon = 0.08$, $H = 2.0\,\mathrm{ML}$, $n_1 = 1.6\,\mathrm{ML}$, $n_2 = 0.4\,\mathrm{ML}$, $n_3 = 0\,\mathrm{ML}$), additional material is distributed into coherently strained islands with $n_2 E_{\mathrm{isl}}$. This transition is typically associated with the Stranski-Krastanow growth mode and in the model mainly correlated with the interface parameters $\Phi_{\mathrm{AB}}$ and $a$ as well as the surface energy $\gamma$ and the coupling factor $p$ between the surface energy $\gamma$ and the strain $\epsilon$. After a deposition of additional 2 ML ($\epsilon = 0.08$, $H = 4.0\,\mathrm{ML}$, $n_1 = 2.3\,\mathrm{ML}$, $n_2 = 0.9\,\mathrm{ML}$, $n_3 = 0.8\,\mathrm{ML}$), plastic relaxation occurs and all three morphological contributions are obtained. The key parameter of this transition are the island interaction factor $b$ as well as the amount of plastic relaxation $g$.

This is typically associated with the growth of large islands, which contain defects and show Ostwald ripening.

For the layer nucleation with a strain value of $\epsilon = 0.12$ ($H = 0.5\,\mathrm{ML}$, $n_1 = 0\,\mathrm{ML}$, $n_2 = 0.5\,\mathrm{ML}$, $n_3 = 0\,\mathrm{ML}$), the energy minimum is obtained for coherent island formation. After a certain thickness of $< 1\,\mathrm{ML}$ ($\epsilon = 0.12$, $H = 1.0\,\mathrm{ML}$, $n_1 = 0.3\,\mathrm{ML}$, $n_2 = 0.7\,\mathrm{ML}$, $n_3 = 0\,\mathrm{ML}$), a two-dimensional layer formation occurs and after one monolayer of $E_{\mathrm{wl}}$ the coherent island growth proceeds [158]. This part seems very questionable due to the lack of interface interaction $\Phi_{\mathrm{AB}}$ in the coherently strained island contribution $E_{\mathrm{isl}}$. Finally, plastic relaxation occurs at a layer thickness of about $H = 2.6\,\mathrm{ML}$ ($\epsilon = 0.12$, $H = 4.0\,\mathrm{ML}$, $n_1 = 1.4\,\mathrm{ML}$, $n_2 = 1.2\,\mathrm{ML}$, $n_3 = 1.4\,\mathrm{ML}$) and again all three morphological contributions are obtained. Due to the high strain, the first transition between the coherent island growth and the two-dimensional growth is highly correlated with the elastic relaxation $g$ inside the coherent islands and the interface bond formation energy $\Phi_{\mathrm{AB}}$. The plastic formation again depends on the island interaction factor $b$ as well as the amount of plastic relaxation $g$.

For a relatively high strain value of $\epsilon = 0.16$ ($H = 0.5\,\mathrm{ML}$, $n_1 = 0\,\mathrm{ML}$, $n_2 = 0.5\,\mathrm{ML}$, $n_3 = 0\,\mathrm{ML}$), the growth starts with coherently strained islands with $n_2 E_{\mathrm{isl}}$. After a certain layer thickness of about $H = 0.9\,\mathrm{ML}$ ($\epsilon = 0.16$, $H = 1.0\,\mathrm{ML}$, $n_1 = 0\,\mathrm{ML}$, $n_2 = 0.9\,\mathrm{ML}$, $n_3 = 0.1\,\mathrm{ML}$), plastic relaxation occurs without the formation of a two-dimensional layer. This transition is related to the Volmer-Weber growth with an inhibited wetting layer formation due to the large strain energy. The critical layer thickness is mainly correlated with the island interaction factor $b$ and the plastic relaxation $g$.

Additionally to the transitions introduced by the material coverage $H$, the transitions correlated with strain $\epsilon$ depend on the material constant $C$ for strain in relation to the formation energies $\Phi_{\mathrm{AA}}$ and $\Phi_{\mathrm{AB}}$. Although the model does not allow for quantitative description, the transitions of the model are qualitatively in good agreement with experimental observations [41].

### 6.2.2 Heteroepitaxial growth as a function of surface energy

In the original paper of Daruka et al. [158], the growth transition between two-dimensional Frank-van-der-Merve growth and three-dimensional Stranski-Krastanow growth occurs at a lattice mismatch of about $\epsilon = 5\%$. For heteroepitaxial growth of GaN on relaxed AlN, the lattice mismatch is fixed to $\epsilon = 2.4\%$. Seifert et al. [41] reported for several

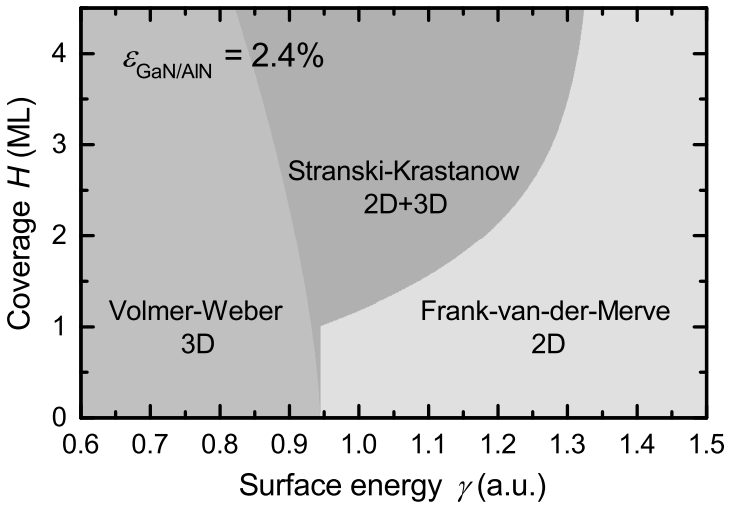


Figure 6.2: Heteroepitaxial growth modes as a function of surface energy $\gamma$ and material coverage $H$ similar to Fig. 6.1. Remaining parameter: $a = 1$, $C = 40E_0$, $\Phi_{AA} = E_0$, $\Phi_{AB} = 1.27E_0$, $g = 0.7$, $p = 4.9$, $\epsilon = 0.024$, and $b = 10$.

heteroepitaxial material systems, that the transition between Frank-van-der-Merve and Stranski-Krastanow growth is experimentally observed at about $\epsilon = 2.5\%$. By adjusting the surface energy [170], the transition can be shifted to lower strain values. Therefore, a phase diagram of the different growth modes as a function of the material coverage $H$ and the surface energy $\gamma$ is presented in Fig. 6.2. In contrast to Fig. 6.1, at a given strain value of $\epsilon_{GaN/AlN} = 2.4\%$ different growth modes may be observed by lowering the surface energy $\gamma$. Even three-dimensional Volmer-Weber growth is obtained below a surface energy of $\gamma < 0.94$ for the given parameter set. In between a surface energy of $0.94 < \gamma < 1.33$, three-dimensional Stranski-Krastanow growth is obtained, and above a surface energy of $\gamma > 1.33$, two-dimensional Frank-van-der-Merve growth is obtained. This exhibits, that controlling the surface energy at the critical strain of $\epsilon_{GaN/AlN} = 2.4\%$ allows controlling the growth morphology.

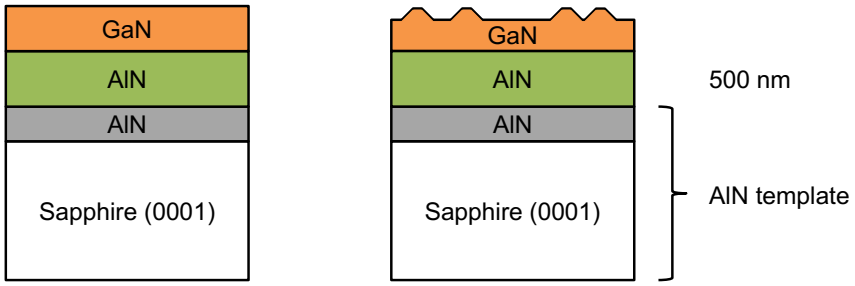


(a) 2D GaN sample structure at high V/III ratio

(b) 3D GaN sample structure at low V/III ratio

Figure 6.3: GaN growth sample structure controlled by V/III ratio

| | $T_{\mathbf{pyro}}$ (°C) | $\phi_{\mathbf{TMAl}}$ ($\mu$mol/min) | $p_{\mathbf{Al}}$ (Pa) | $\phi_{\mathbf{TMGa}}$ ($\mu$mol/min) | $p_{\mathbf{Ga}}$ (Pa) | $\phi_{\mathbf{NH_3}}$ (sccm) | $p_{\mathbf{N}}$ (Pa) | $V/III$ |
|---|---|---|---|---|---|---|---|---|
| **AlN** | 1080 | 35.5 | 2.0 | | | 12 | 30 | 15 |
| **GaN** | 840 | | | 3.7 | 0.2 | 6 – 100 | 15 – 250 | 75 – 1200 |

Table 6.1: Important growth parameters (For partial pressures $p_i$ complete pyrolysis is assumed.)

## 6.3 Sample structure and growth conditions

The heteroepitaxial growth of GaN on AlN is investigated by metalorganic vapor-phase epitaxy on AlN (0001) templates, which are provided by Viola Küller [126]. An AlN buffer layer is grown to generate a clean smooth AlN surface for GaN nucleation independent of any surface modifications of the AlN templates. It is grown under smooth two-dimensional layer-by-layer growth conditions. The following GaN growth evolution is investigated for different V/III ratios at a growth temperature of $T_{\mathrm{pyro}} = 840°\mathrm{C}$ and with hydrogen as carrier gas. The layer stacks at different V/III ratios are shown in Fig. 6.3. At first, a growth time series at a high V/III ratio of $V/III = 1200$ with different growth times of $t_{\mathrm{GaN}} = 10\,\mathrm{s}$, $20\,\mathrm{s}$, $30\,\mathrm{s}$, and $40\,\mathrm{s}$ is studied. Next, the V/III ratio is varied at a growth time of $t_{\mathrm{GaN}} = 30\,\mathrm{s}$ between $V/III = 75$ and 1200. Finally, a second growth time series at a low V/III ratio of $V/III = 75$ with different growth times of $t_{\mathrm{GaN}} = 10\,\mathrm{s}$, $20\,\mathrm{s}$, $22\,\mathrm{s}$, $24\,\mathrm{s}$, $26\,\mathrm{s}$, $28\,\mathrm{s}$, $30\,\mathrm{s}$, and $40\,\mathrm{s}$ is discussed. All important growth parameters are collected in Table 6.1 and further details can be found in Chapter 3.1.

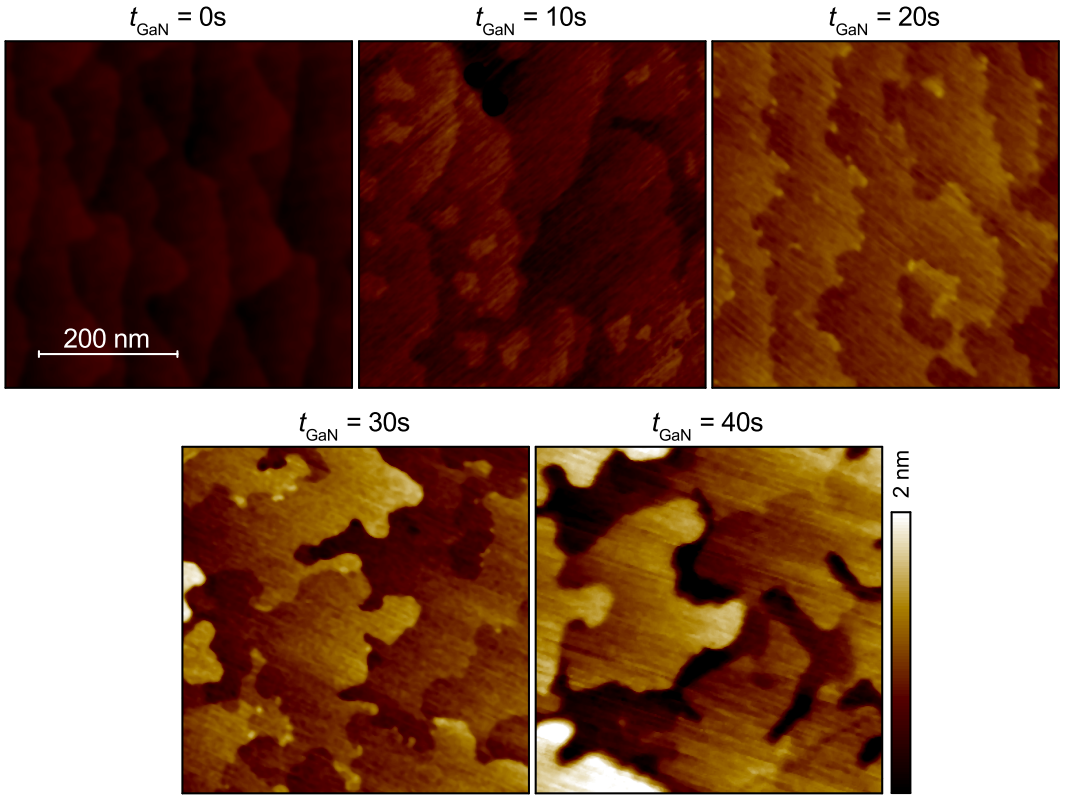


Figure 6.4: GaN surface morphology obtained by atomic force microscopy after certain GaN deposition times grown at high $V/III = 1200$.

## 6.4 Morphological results of uncapped samples

### 6.4.1 High V/III ratio – 2D growth

For a high V/III ratio of $V/III = 1200$, Fig. 6.4 exhibits the surface morphologies obtained for different growth times of GaN. All samples show rather smooth surfaces dominated by terraces. The reference surface of AlN (Fig. 6.4, $t_{\mathrm{GaN}} = 0\,\mathrm{s}$) exhibits individual monolayer high terrace steps sharing rather smooth edges. The GaN nucleation on the AlN substrate (Fig. 6.4, $t_{\mathrm{GaN}} = 10\,\mathrm{s}$) is first obtained on the terrace and not at the step edges forming sub-monolayer islands, which are islands of just one monolayer height and finite diameters. Even though GaN could generate more chemical bonds at the step edge, the deformation of those chemical bonds by the strain situation might inhibit the GaN nucleation on AlN monolayer steps. In some cases isolated pits can occur, which are related to the AlN buffer growth and, therefore, excluded from the GaN growth discussion. After $t_{\mathrm{GaN}} = 20\,\mathrm{s}$, the AlN substrate appears to be completely covered by GaN and subsequent growth occurs at the step edges with many little nucleation sites,

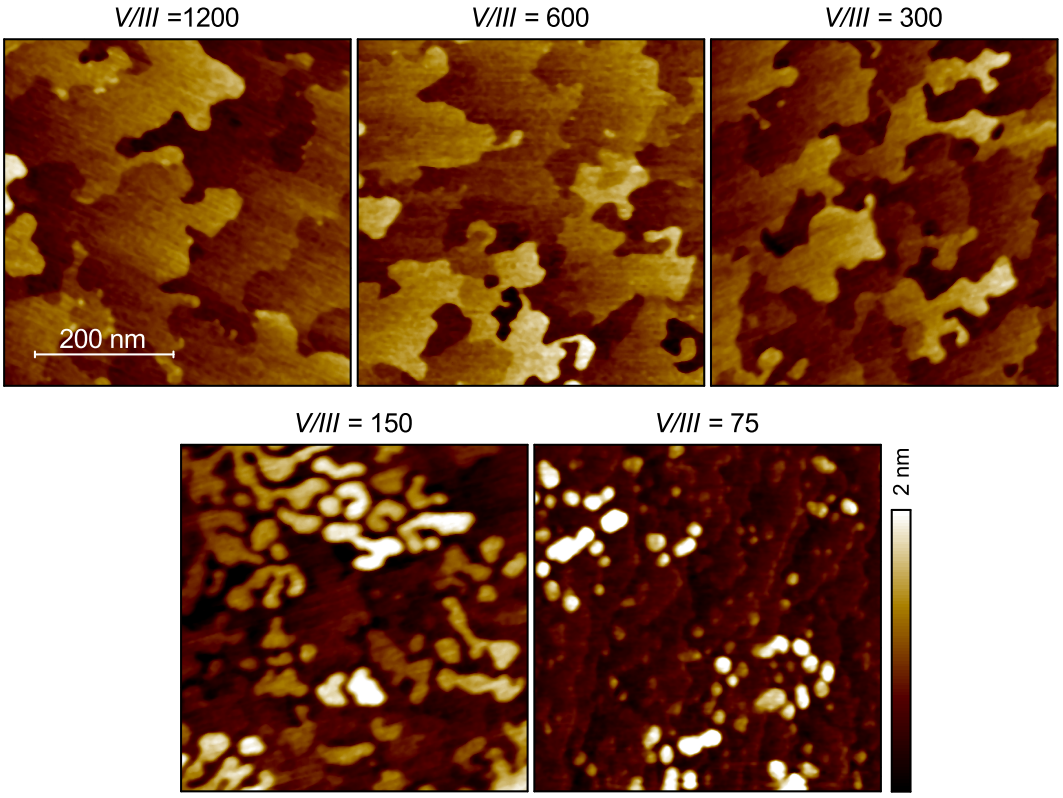


Figure 6.5: GaN surface morphology obtained by atomic force microscopy for different V/III ratios after GaN growth of $t_{\mathrm{GaN}} = 30\,\mathrm{s}$.

visible by the tear-like terrace edge morphology. Due to an entire GaN wetting layer on the AlN surface, the strain situation at the terrace steps has most likely changed. Even dislocations could promote GaN nucleation, which might be the origin of the tear-like terrace edge morphology. From this stage, GaN appears to grow laterally at the terrace edges yielding two-dimensional Frank-van-der-Merve growth with rather rough, irregular terrace edges (Fig. 6.4, $t_{\mathrm{GaN}} = 30\,\mathrm{s}$). When the growth proceeds (Fig. 6.4, $t_{\mathrm{GaN}} = 40\,\mathrm{s}$), the irregular shape of the terrace edges is accompanied by a suppressed layer coalescence resulting in very rough step edges and even multi-layer steps. It appears, that GaN is able to reduce its strain energy at the step edges by relaxing into the surrounding void limiting further coalescence.

### 6.4.2 Influence of V/III ratio – 2D/3D transition

To investigate the influence of the V/III ratio on the growth morphology, a growth series above the critical wetting layer thickness is performed with $t_{\mathrm{GaN}} = 30\,\mathrm{s}$. Fig. 6.5

exhibits the obtained surface morphologies for different V/III ratios. For large V/III ratios $V/III \geq 300$, the surfaces are characterized by smooth terraces with monolayer steps. For small V/III ratios $V/III \leq 150$, the surfaces are characterized by individually separated islands on terraced surfaces. Even though this appears to be a discontinuous transition, a closer look at the terrace edges and the island shapes exhibit a continuous change. For the two-dimensionally grown GaN a correlation between the V/III ratio and the edge shape exhibit straighter terrace edges for large V/III ratios (Fig. 6.5, $V/III = 1200$) and much more curved terrace edges closer to the morphology transition (Fig. 6.5, $V/III = 300$). The island growth with a V/III ratio of $V/III = 150$ exhibits large flat islands. For the lowest V/III ratio of $V/III = 75$, small isolated islands are obtained. This suggests, that lowering the V/III ratio is correlated with a continuous reduction of the surface energy. After the complete wetting of the AlN surface with no sub-monolayer islands left on the surface, the material system is aiming for minimizing the strain energy. For large V/III ratios, the strain appears to be reduced at the expense of an increasing terrace edge length, which can be larger for lower surface energies. At a V/III ratio of $V/III = 150$, the surface energy density is apparently small enough for isolated island formation on the terraces away from the terrace edges. This enables further strain minimization by increasing the surface area allowing surface atoms to elastically relax into the surrounding void. At a V/III ratio of $V/III = 75$, even smaller islands are formed indicating a further reduction of the surface energy. This continuous change of the surface energy is most likely not explained by a sudden change of the surface reconstruction. It might rather be related to a single type of surface reconstruction with a surface energy depending on the surrounding vapor-phase (Chapter 2.1.2). Due to a change of the surface energy with different V/III ratios, it is most likely gallium-terminated. In the literature, the morphology transition between two-dimensional and three-dimensional growth is observed at $V/III = 2500$ [63]. However, typical Stranski-Krastanow growth is presented by several groups to be below $V/III < 100$ [60, 62, 63, 65]. This observation might be related to the correlation with additional growth parameters like temperature and growth speed.

### 6.4.3 Low V/III ratio – 2D/3D transition

The growth of GaN under low V/III ratio of $V/III = 75$ is shown in Fig. 6.6. The AlN morphology exhibits a smooth surface with monolayer terraces (Fig. 6.6, $t_{\mathrm{GaN}} = 0\,\mathrm{s}$). GaN starts to nucleate on top of the AlN terraces forming sub-monolayer islands (Fig. 6.6, $t_{\mathrm{GaN}} = 10\,\mathrm{s}$) similar to the growth under high V/III ratio of $V/III = 1200$. They grow laterally and coalesces to a complete two-dimensional layer. After about $t_{\mathrm{GaN}} = 22\,\mathrm{s}$, the

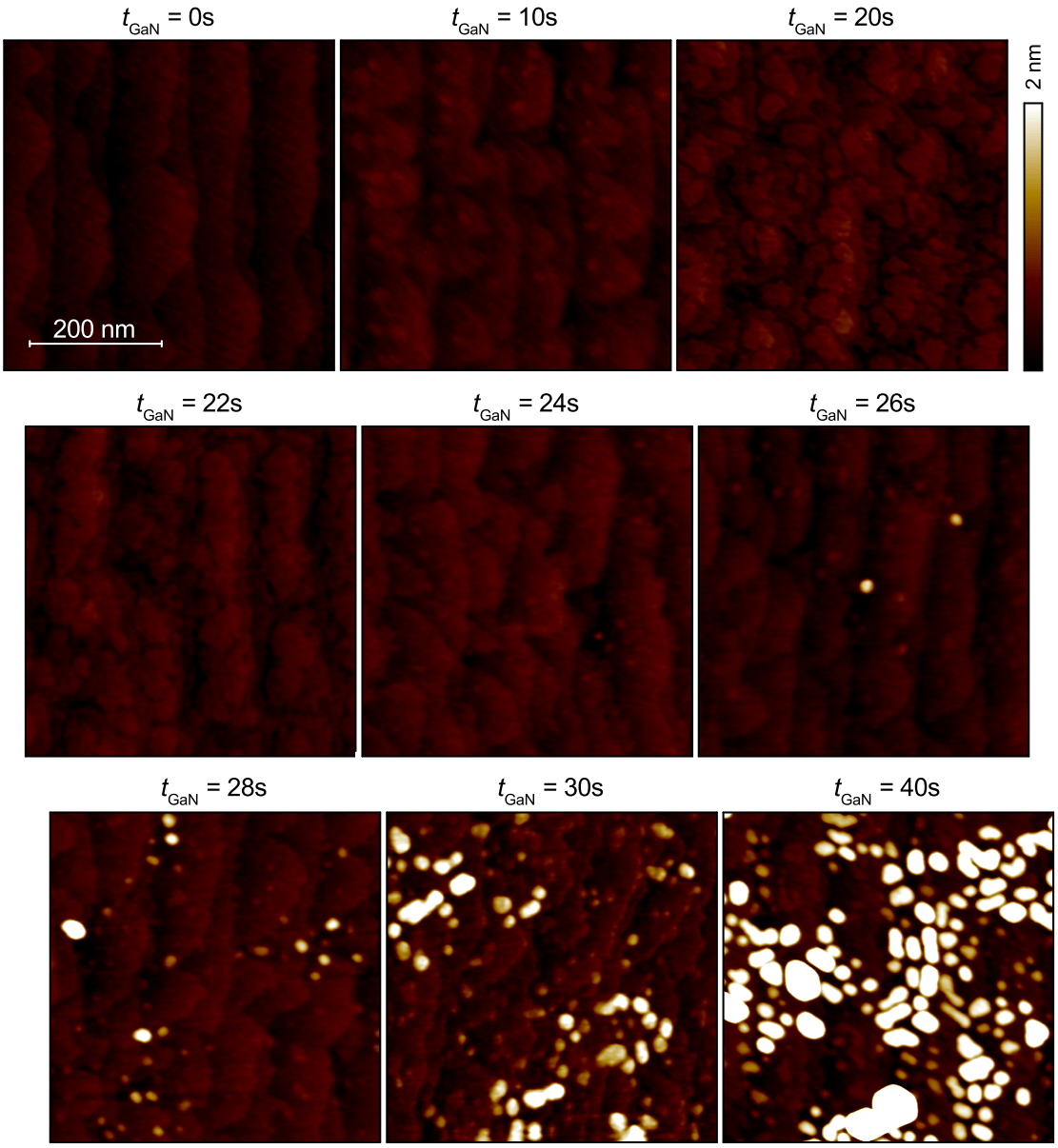


Figure 6.6: GaN surface morphology obtained by atomic force microscopy after certain GaN deposition times grown at low $V/III = 75$.

AlN substrate appears to be completely wetted by GaN. Due to the very large surface energy of AlN [171], the surface is completely covered by a GaN wetting layer to lower the surface energy of the heterostructure. In contrast to the GaN growth under high V/III ratio, any additional GaN keeps on growing three-dimensionally on the terraces forming quantum dot structures. Due to a potentially lower surface energy of GaN under vapor-phase conditions with low V/III ratio, the system is able to increase the surface area for elastic strain relaxation into the surrounding void. Therefore, three-dimensional

structures are formed, which yield lower total energy with a reduction of the strain energy at the expense of a slightly increased surface energy. Representative quantum dots are about $(25 \pm 10)$ nm in diameter and about $(1.5 \pm 0.5)$ nm in height (Fig. 6.6, $t_{\mathrm{GaN}} = 26\,\mathrm{s}$), which are similar to reported values [45, 48, 52, 58, 148, 155, 172]. With further material supply, the islands grow in size and density. At a GaN growth of about $t_{\mathrm{GaN}} = 30\,\mathrm{s}$, the islands start to coalesce forming larger clusters (Fig. 6.6, $t_{\mathrm{GaN}} = 30\,\mathrm{s}$). This is most likely associated with defect formation at the island boundaries of the quantum dots for plastic strain relaxation. Further GaN growth promotes cluster formation with increasing size (Fig. 6.6, $t_{\mathrm{GaN}} = 40\,\mathrm{s}$). The formation of large clusters should be avoided for optoelectronic applications due to the non-radiative exciton recombination at defects, which is further enhanced by small confinement energies trapping excitons in the vicinity.

This growth study illustrates the very tiny growth window for GaN quantum dots. Especially metalorganic vapor-phase epitaxy without a proper in-situ tool like reflective high-energy electron-diffraction, requires very stable growth conditions to offer reproducible and reliable results.

### 6.4.4 Analysis of the wetting layer thickness

The Stranski-Krastanow growth is defined by a two-dimensional wetting layer formation followed by three-dimensional islands growth. The transition is characterized by the critical wetting layer thickness $\theta_{\mathrm{c}}$. This can be determined by atomic force microscopy, if the amount of deposited material $\theta$ and the quantum dot density $\rho$ is well known. In order to determine the amount of deposited material $\theta$, a detailed analysis of the three-dimensional structures is performed (Chapter 3.2). The solid green and yellow symbols of Fig. 6.7a exhibit the determined three-dimensional coverage by atomic force microscopy as a function of different growth times. The sub-monolayer growth at $t_{\mathrm{GaN}} = 10, 20, 22\,\mathrm{s}$ consists of respective 0.1, 0.9, 0.95 ML and is marked by the gray area. The three-dimensional island growth beyond $t_{\mathrm{GaN}} \leq 24\,\mathrm{s}$ is marked with the white area and is equal to the green solid data points. Due to an unknown two-dimensional contribution, the data is shifted up by one, two, or three possible monolayers (marked by arrow, open symbols of Fig. 6.7a). Apparently, simple linear fits of the growth rate $r$ yield the best agreement (smallest Chi-square) for a shift of two possible monolayers with a growth rate of $r = (0.09 \pm 0.01)$ML/s (magenta, Fig. 6.7a). The measured nanostructure density $\rho$ is plotted as a function of the various possible material coverages $\theta$ in Fig. 6.7b. In contrast to Leonard et al. [173], who describe the quantum dot density evolution by a simple

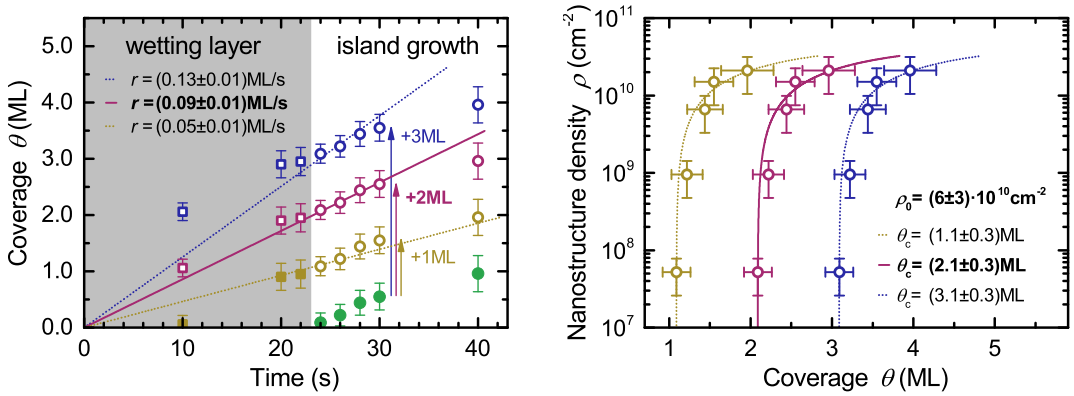


(a) 3D structure coverage $\theta$ by atomic force microscopy (raw data corresponds to solid symbols) shifted by several monolayers (open symbols). Linear fit yields growth rate $r$.

(b) 3D nanostructure density $\rho$ as a function of several possible coverages $\theta$ fitted by an exponential saturation function (Eq. 6.5).

Figure 6.7: Determination of the critical wetting layer thickness by atomic force microscopy. Squares represent sub-monolayer islands, and circles represent quantum dots. Unknown two-dimensional material below the nanostructures is presented for three possible cases (yellow +1ML, magenta +2ML, blue +3ML).

power low, an exponential description offers a saturation quantum dot density $\rho_0$ with

$$\rho = \rho_0 \left[1 - \mathrm{e}^{-\alpha(\theta-\theta_\mathrm{c})}\right], \tag{6.5}$$

a converging factor $\alpha$, and the critical wetting layer thickness $\theta_\mathrm{c}$. In the range of the first monolayer, the saturation quantum dot density $\rho_0$ and the converging factor $\alpha$ are highly correlated yielding large errors for the determined saturation quantum dot density $\rho_0 = (6 \pm 3) \cdot 10^{10}\,\mathrm{cm}^{-2}$. This correlates with a maximum quantum dot size of $d = (40 \pm 15)\,\mathrm{nm}$, which would be obtained at the saturation density if no lateral gap between quantum dots is assumed. The determined critical wetting layer thickness highly depends on the assumed growth rate. For the most plausible case of Fig. 6.7b (magenta), a critical wetting layer thickness of $\theta_\mathrm{c} = (2.1 \pm 0.3)\,\mathrm{ML}$ is obtained.

In order to verify the wetting layer thickness, high-resolution scanning transmission electron microscopy is performed on the sample with a high quantum dot density and low cluster density at $t_\mathrm{GaN} = 28\,\mathrm{s}$. A cross-section of the sample in $\vec{a}$-direction with a high-angle annular dark field detection is shown in Fig. 6.8. In the ensemble image of Fig. 6.8a, three different quantum dots are visible with a diameter of about $d = (17 \pm 5)\,\mathrm{nm}$ and a height of about $h = (2.8 \pm 0.5)\,\mathrm{nm}$. This is in good agreement with the atomic force microscopy data yielding slightly larger diameters and smaller heights due to respective

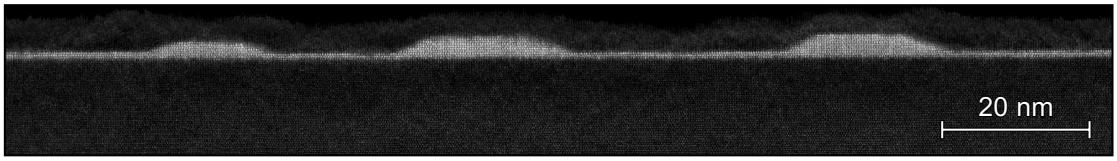


(a) Cross-section scanning transmission electron microscopy image of a GaN quantum dot ensemble.

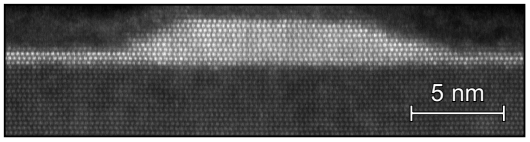


(b) Magnification of GaN quantum dot.

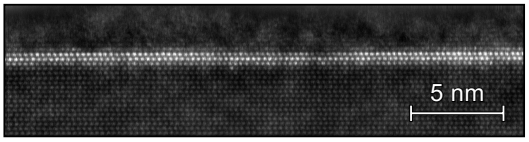


(c) Magnification of GaN wetting layer.

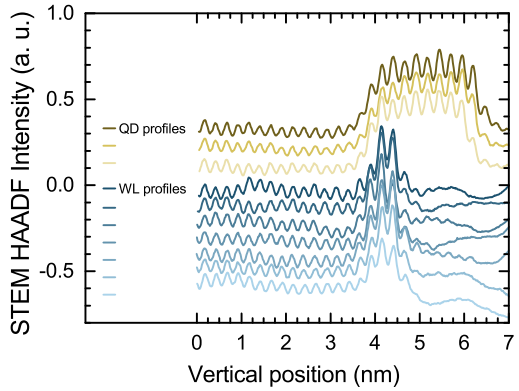


(d) Three vertical intensity profiles of the GaN quantum dot (QD) and seven profiles of the GaN wetting layer (WL).

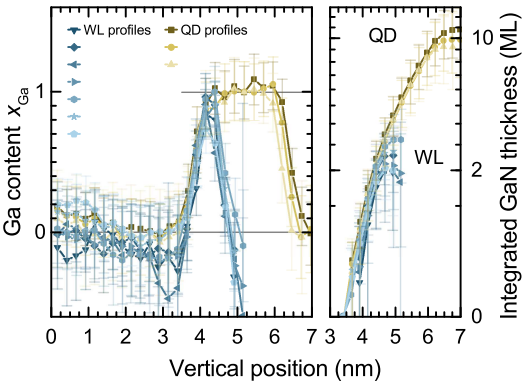


(e) (left) Ga content of layers by normalizing to the underlying AlN and to the GaN quantum dot region. (right) GaN wetting layer thickness by integrated Ga content of layers.

Figure 6.8: Cross-section scanning transmission electron microscopy (STEM) images of GaN quantum dots ($t_{\mathrm{GaN}} = 28\,\mathrm{s}$) with high-angle annular dark field (HAADF) detection in $\vec{a}$-direction (by Toni Markurt). Quantitative GaN wetting layer (WL) by correlating the intensity with the gallium content $x_{\mathrm{Ga}}$.

tip broadening and an unknown two-dimensional wetting layer contribution by atomic force microscopy.

A higher magnification of a quantum dot region and a region containing only a wetting layer are exhibited in Fig. 6.8b and Fig. 6.8c, respectively. Each bright spot is associated with a column of metal atoms scattering electrons much stronger than nitrogen atoms. The intensity of an atomic column depends on the amount of gallium and aluminum atoms, which both scatter electrons differently. The annular detector is more sensitive to elements with high atomic numbers. Figure 6.8d exhibits ten selected vertical intensity profiles with three profiles at the quantum dot and seven profiles at the wetting layer, one on the left and one on the right side of the quantum dot in Fig. 6.8b and five from the

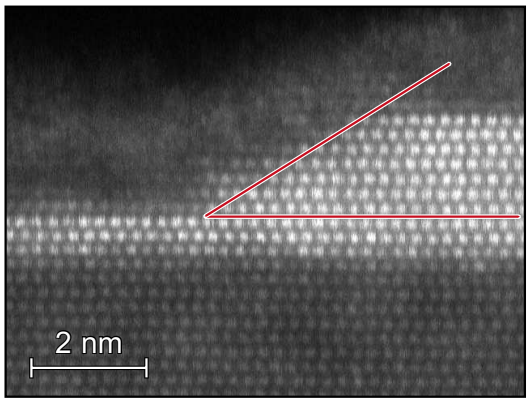


(a) Magnification of a GaN quantum dot of Fig. 6.8. The angle between the side facet and the basal plane is about $(33 \pm 2)^\circ$ and marked in red.

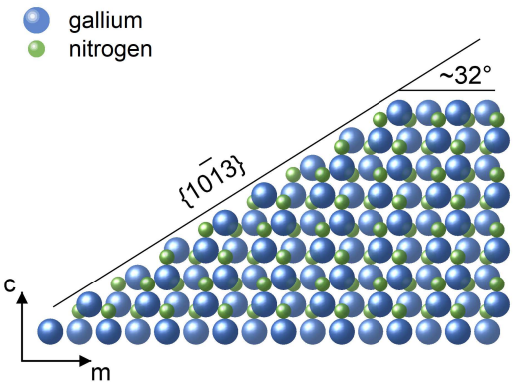


(b) Sketch of the GaN crystal structure in $\vec{a}$-direction with the $\{10\bar{1}3\}$-facet and the $c$-facet with an angle of 32°.

Figure 6.9: Side facet of GaN quantum dot compared to theoretical crystal orientation.

wetting layer region in Fig. 6.8c. Each profile shows clear peaks for individual monolayers, which are averaged over five adjacent lateral atomic columns. Although only binary materials were grown, intermediate values are obtained at interfaces. By normalizing the intensity profile of AlN to zero gallium content and the GaN quantum dot to pure GaN, the gallium content inside an atomic column can be calculated and is shown in Fig. 6.8e on the left. Due to very rough interfaces of the specimen visible in the intensity fluctuations of the AlN area in Fig. 6.8c, a large error is obtained for the determined composition of absolute $\Delta x = \pm 0.2$. Integrating the GaN layers provides the critical wetting layer thickness of about $\theta_c = (2.5 \pm 1)\,\mathrm{ML}$. Even though the error by the specimen thickness fluctuations is very large, a wetting layer thickness of $(2-3)\,\mathrm{ML}$ appears qualitatively convincing.

Both wetting layer thicknesses determined by atomic force microscopy with $\theta_c^{\mathrm{AFM}} = (2.1 \pm 0.3)\,\mathrm{ML}$ and by scanning transmission electron microscopy with $\theta_c^{\mathrm{TEM}} = (2.5 \pm 1)\,\mathrm{ML}$ are in very good agreement. Similar wetting layer thicknesses of $\theta_c = (1.5 - 2.5)\,\mathrm{ML}$ are reported for GaN quantum dots grown by molecular beam epitaxy [49, 50, 174, 175], which are measured in-situ by reflective high-energy electron-diffraction or scanning transmission electron microscopy. However, for metalorganic vapor-phase epitaxy a wide range of $\theta_c = (1 - 10)\,\mathrm{ML}$ is reported [58, 61, 62]. This might be mainly related to unprecise growth rate determinations.

### 6.4.5 Surface energy balance

In order to analyze the surface energy contributions, a high magnification scanning transmission electron microscopy image of the cross section of a GaN quantum dot in $\vec{a}$-direction is shown in Fig. 6.9a. The obtained angle between the side facet and the basal plane is about $(33 \pm 2)^\circ$ and marked in red. This corresponds to $\{10\bar{1}3\}$ facets, which is in agreement with the literature [49, 52, 63]. A sketch of a GaN quantum dot in $\vec{a}$-direction with $\{10\bar{1}3\}$ side facets is exhibit in Fig. 6.9b. The theoretical angle of 32° between the (0001) basal plane and the $\{10\bar{1}3\}$ side facet is highlighted.

In order to understand the differences between the three major growth techniques, a closer look on the surface energy budget is necessary. Additional to the quantum dot formation discussed in Chapter 6.2, a morphology transition between two-dimensional and three-dimensional growth may occur if the surface energy of the side facets is much smaller than the two-dimensional basal plane. In this case, three-dimensional growth is favored despite the larger surface area. As discussed, the shape of GaN quantum dots is described by truncated pyramids with bottom and top facets of (0001) basal planes and $\{10\bar{1}3\}$ side facets with an angle of about 32°. The GaN quantum dot formation of AlN is characterized by the delicate balance between the surface energy and the strain energy. The difference of the surface energy $\Delta E_{\text{surface}}$ to two-dimensional growth is related to the amount of side-facets, which is described by

$$\Delta E_{\text{surface}} = \frac{\gamma_{10\bar{1}3}}{\cos 32^\circ} - \gamma_{0001} \tag{6.6}$$

with the surface energy of the basal plane $\gamma_{0001}$ and the surface energy of the side facet $\gamma_{10\bar{1}3}$ [49]. Most of the theoretical publications about the surface energy under various growth conditions are associated with molecular beam epitaxial growth conditions [83,176,177] and very few are considering hydrogen as a surface termination source [85,89]. Figure 6.10 exhibits the morphology transition between two-dimensional growth (bright area) and three-dimensional growth (dark area) as a function of the two important surface energies $\gamma_{0001}$ and $\gamma_{10\bar{1}3}$. If the surface energy of the (0001) basal plane is much smaller than that of the $\{10\bar{1}3\}$ side facet, two-dimensional growth is obtained (bright area), and if the surface energy of the (0001) basal plane is much larger than the $\{10\bar{1}3\}$ side facet, three-dimensional growth is obtained (dark area). If no strain relief inside the quantum dots is assumed, a morphology transition would occur at $\Delta E_{\text{surface}} = 0$ (black line, Fig. 6.10). To estimate an additional strain relieve, a detailed knowledge of uncapped quantum dots would be required. Even capped quantum dots show rather complicated

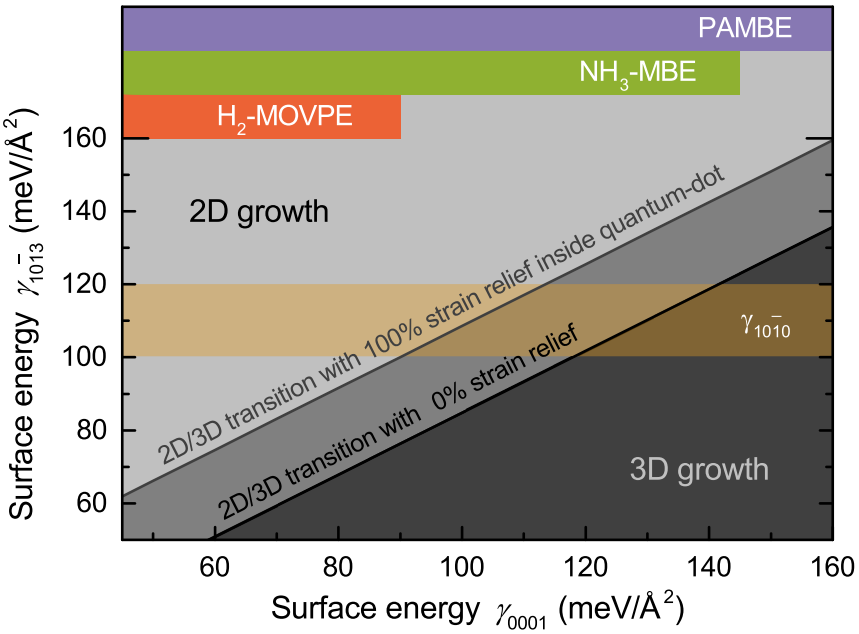


Figure 6.10: Phase diagram of the two-dimensional growth (light gray) and the three-dimensional growth (dark gray) as a function of the surface energy of the quantum dot side-facets $\{10\bar{1}3\}$, the basal plane (0001), and the amount of elastic relaxation inside the quantum dots. Possible surface energies of $\gamma_{0001}$ are highlighted for plasma-assisted molecular beam epitaxy (PAMBE, purple), ammonia-assisted molecular beam epitaxy ($NH_3$-MBE, green), and metalorganic vapor-phase epitaxy with hydrogen ($H_2$-MOVPE, orange). Due to unknown theoretical predictions of the surface energy $\gamma_{10\bar{1}3}$, $\gamma_{10\bar{1}0}$ is marked in yellow as a guide for the eye.

strain profiles [175, 178–180]. Therefore, an additional transition line is plotted for a 2 nm high quantum dot with an elastic strain relieve of 16 meV per atom, which was calculated to be the case for a GaN wetting layer biaxially strained to AlN [181] (gray line 100% strain relieve, Fig. 6.10).

The energy ranges of the basal plane $\gamma_{0001}$ for different growth methodes are based on Dreyer et al. [89]. Plasma-assisted molecular beam epitaxy is marked in purple, ammonia-assisted molecular beam epitaxy with very low hydrogen pressure is marked in green, and metalorganic vapor-phase epitaxy with very high hydrogen pressure is marked in orange. No theoretical information about the surface energy of a $\{10\bar{1}3\}$ side facet could be found. For an estimated energy range of the side facet $\gamma_{10\bar{1}3}$, the surface energy range of the m-plane $\gamma_{10\bar{1}0}$ is marked in yellow as a guide for the eye. Due to the nitrogen-terminated surface reconstruction of the (0001) basal plane in plasma-assisted molecular beam epitaxy and the very low hydrogen pressure in ammonia-assisted molecular beam epitaxy, a surface transition into three-dimensional growth is much more likely even at surface

energies of the $\{10\bar{1}3\}$ side facet with $\gamma_{10\bar{1}3} \leq 160\,\mathrm{meV/\AA^2}$ and $\gamma_{10\bar{1}3} \leq 140\,\mathrm{meV/\AA^2}$, respectively. However, hydrogen-assisted metalorganic vapor-phase epitaxy requires $\{10\bar{1}3\}$ side facets with even lower surface energies of $\gamma_{10\bar{1}3} \leq 100\,\mathrm{meV/\AA^2}$.

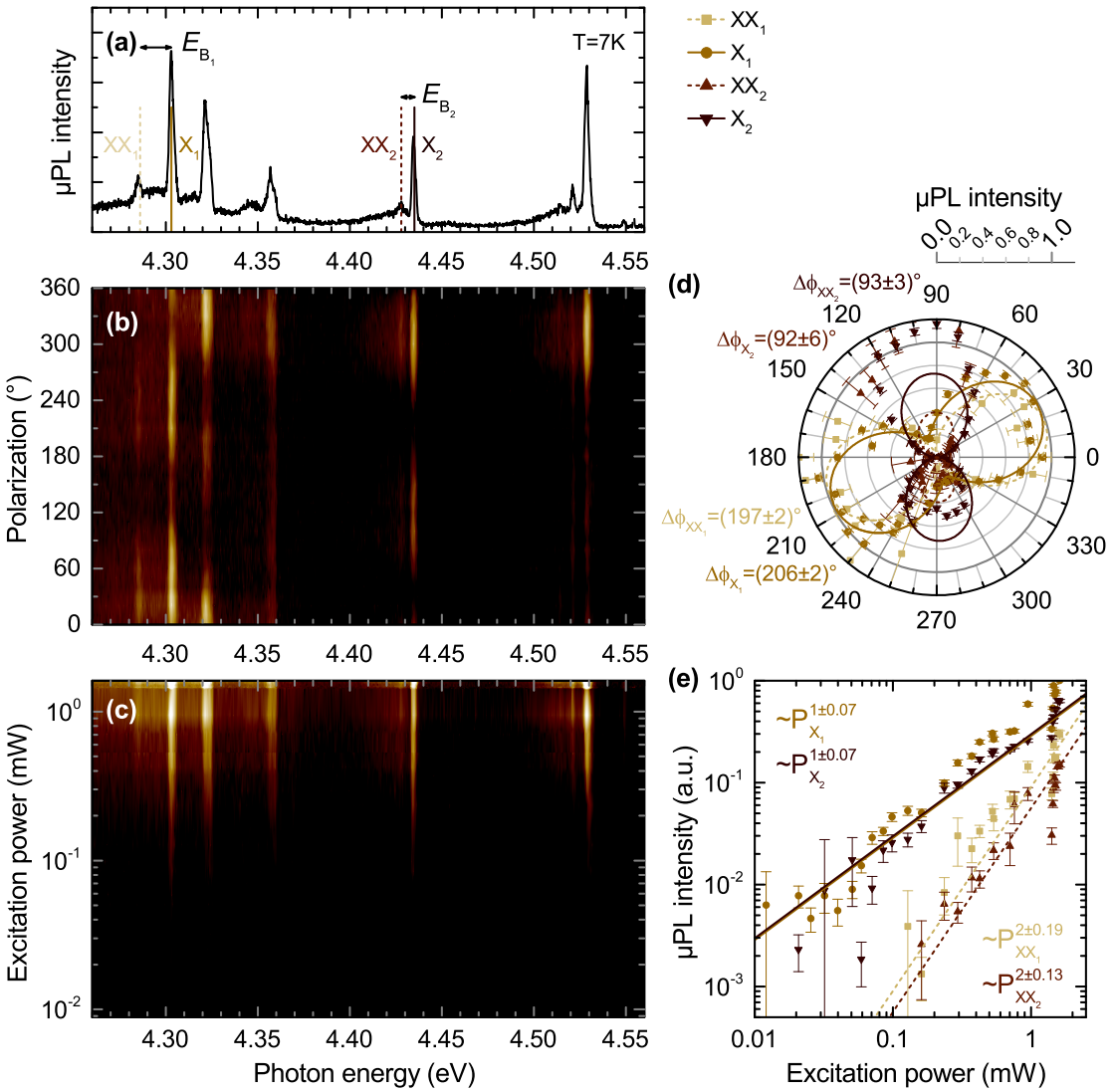


Figure 6.11: Optical properties of capped Stranski-Krastanow GaN quantum dots by micro-photoluminescence measurements ($\mu$PL) at $T = 7\,\mathrm{K}$ with frequency-doubled Ar-ion excitation at $\lambda_{exc} = 244\,\mathrm{nm}$. (a) Representative spectrum at 1.4 mW without polarizer and marked investigated peaks at 4.286 eV ($XX_1$), 4.303 eV ($X_1$), 4.428 eV ($XX_2$), and 4.435 eV ($X_2$). (b) Contour plot of the intensity as a function of photon energy and polarization angle. (c) Contour plot of the intensity as a function of photon energy and excitation power. (d) Polar plot of the intensity as a function of the polarization angle of the investigated peaks. (e) Intensity as a function of the excitation power of the investigated peaks.

## 6.5 Optical properties of capped samples

For optical investigations, a GaN quantum dot sample with a very low density at $t_{GaN} = 24\,\mathrm{s}$ was regrown and immediately capped with AlN. Mesa structures are processed on the wafer by electron beam lithography (Chapter 3.3) to assure individual quantum

dots are probed in a reproducible manner. The sample was placed inside an optical cryostat for micro photoluminescence measurements and cooled by liquid helium to temperatures of $T = 7\,\mathrm{K}$ (Chapter 3.4). The optical response of one mesa structure under a frequency doubled $Ar^{2+}$-ion laser excitation with $\lambda_{\mathrm{exc}} = 244\,\mathrm{nm}$ is shown in Fig. 6.11. An overview spectrum under high excitation of 1.4 mW with no polarization detection is plotted in Fig. 6.11a with two pairs of peaks selected for detailed investigation, one pair at 4.286 eV ($XX_1$) and 4.303 eV ($X_1$), and another pair at 4.428 eV ($XX_2$) and 4.435 eV ($X_2$). All features show strong acoustic phonons on the lower photon energy side, which are typical for GaN quantum dots [182–184]. The polarization dependence of the optical response is shown as a contour plot in Fig. 6.11b. All optical features show a unique polarization dependence. Additionally, all optical features are excitation power dependent (Fig. 6.11c). In a closer look, both luminescence pairs appear to have a similar polarization dependence (Fig. 6.11d) indicating that both pairs originate each from the same quantum dot. In addition to the similar polarization, both pairs show different excitation power dependencies (Fig. 6.11e). On one hand, the high photon energy features at peak 4.303 eV ($X_1$) and 4.435 eV ($X_2$) have a linear excitation power dependence associated with a single exciton transition (Chapter 3.4). On the other hand, the low photon energy features at peak 4.286 eV ($XX_1$) and 4.428 eV ($XX_2$) have a quadratic excitation power dependence associated with a biexciton transition. The biexciton binding energy $E_{\mathrm{B}}$ is about $E_{\mathrm{B}_1} = (17 \pm 4)\,\mathrm{meV}$ and $E_{\mathrm{B}_2} = (7 \pm 4)\,\mathrm{meV}$. This is in good agreement with the literature values, which are reported up to 30 meV for GaN quantum dots [27–31], which highly depend on the structural properties like aspect ratio and height.

A deeper structural investigation was performed of a capped sample grown under low V/III ratio with $V/III = 75$ with $t_{\mathrm{GaN}} = 28\,\mathrm{s}$ by scanning transmission electron microscopy combined with cathodoluminescence. Fig. 6.12a exhibits a bright-field cross-section scanning transmission electron microscopy image of the whole layer stack with the AlN template at the bottom, the AlN buffer layer, the GaN layer, and the AlN capping layer at the top. The very dark line close to the surface corresponds to the GaN and appears more like a rough quantum well than typical quantum dots. Although the resolution does not allow to resolve individual monolayers, it is clearly different to the observation of uncapped GaN quantum dots (Fig. 6.8). Corresponding cathodoluminescence of the same area is shown in Fig. 6.12b. It reveals localized luminescence centers, which might be associated with the excitonic and biexcitonic features measured in micro photoluminescence. The yellow arrows in Fig. 6.12a mark the luminescence centers of Fig. 6.12b. It appears that

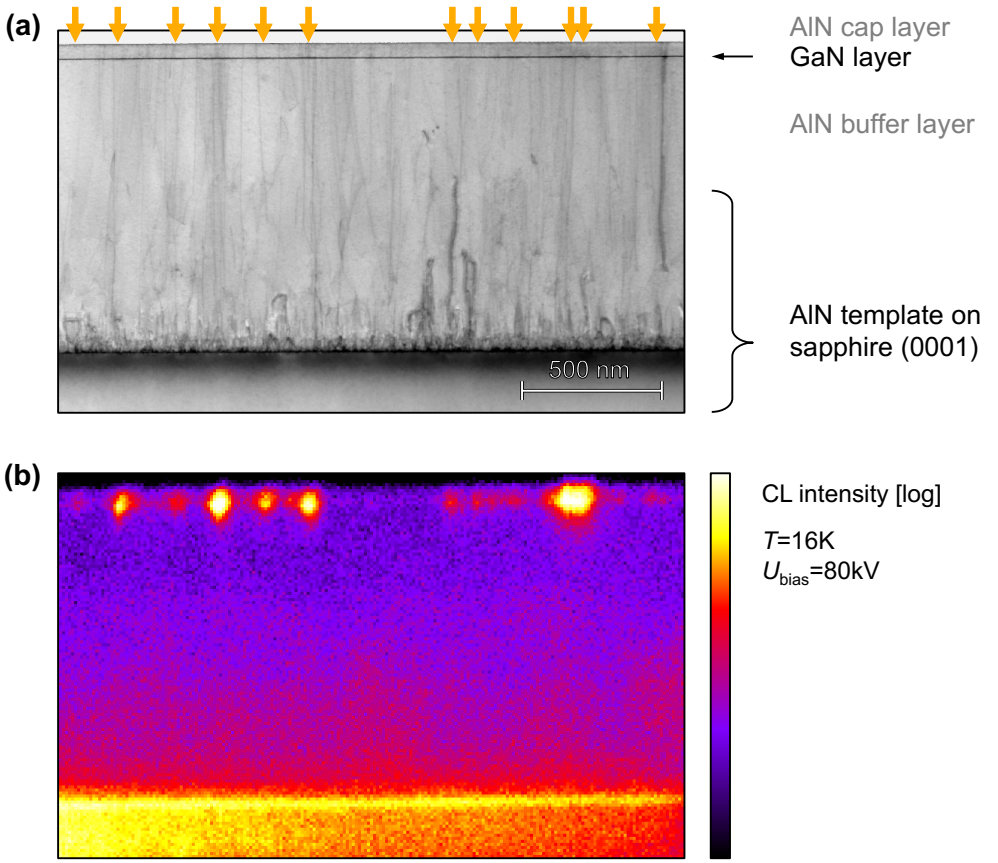


Figure 6.12: (a) Bright-field cross-section scanning transmission electron microscope image of capped GaN with $V/III = 75$ and $t_{\mathrm{GaN}} = 28\,\mathrm{s}$. Luminescence centers of (b) are highlighted with yellow arrows. (b) Corresponding panchromatic cathodoluminescence measurement with $U_{\mathrm{bias}} = 80\,\mathrm{kV}$ at $T = 16\,\mathrm{K}$ (by Alexander Reuper).

the position of the luminescence is not strictly correlated to threading dislocations, as it has been reported by other groups [69–71, 122]. Therefore, the localized emission could be related to thickness fluctuations inside the quantum well, which has been reported for other material systems like InGaN [185, 186].

The capping of the GaN quantum dots was performed via a two step AlN growth. Right after the GaN deposition, AlN was deposited at the low growth temperature of the GaN quantum dots. On one hand, this could indicate that even for low V/III GaN growth a growth interruption is necessary for quantum dot formation occurring during the cool-down of uncapped samples, as reported by Kako [30]. However, no ripening of uncapped quantum dots with ammonia supply could be observed. On the other hand, a high temperature AlN layer was grown to improve the quality of the AlN layer. This could

lead to an additional material diffusion of the GaN, which annihilates the quantum dots yielding rough GaN quantum well layers according to the literature [187, 188]. Further investigations are necessary to maintain the excellent quantum dot structure during the capping process.

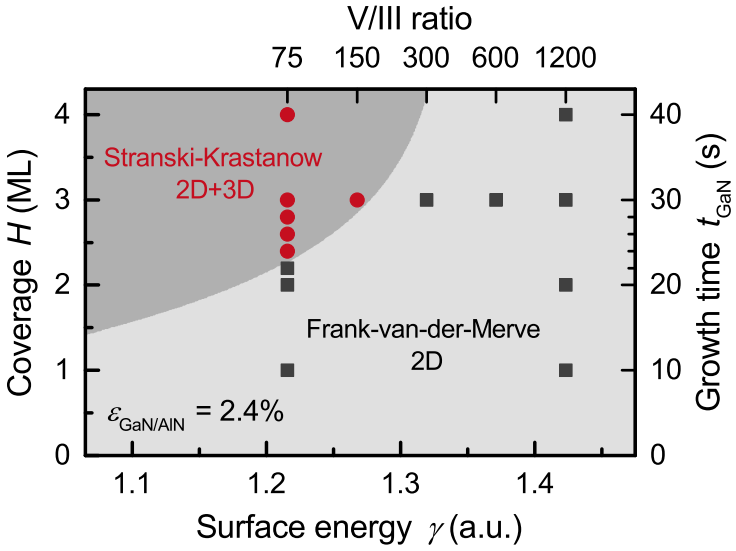


Figure 6.13: Superposition of the phase diagram of the morphology transition between three-dimensional Stranski-Krastanow growth (dark gray, red circles) and two-dimensional Frank-van-der-Merve growth (light gray, black squares) of GaN on AlN obtained with a qualitative growth model and with atomic force microscopy of heteroepitaxial growth.

## 6.6 Conclusion

In this chapter, GaN Stranski-Krastanow quantum dots are achieved by controlling the surface energy in metalorganic vapor-phase epitaxy. Initially, the growth transition between two-dimensional Frank-van-der-Merve growth and three-dimensional Stranski-Krastanow growth is theoretically described by a qualitative growth model. In particular, the influence of the surface energy on the growth mode is discussed at a constant lattice strain of $\epsilon_{\mathrm{GaN/AlN}} = 2.4\%$. Then, the control of the surface energy of GaN during epitaxial growth is demonstrated experimentally by changing the V/III ratio. On one side, a high surface energy with $V/III \geq 300$ yields two-dimensional Frank-van-der-Merve growth. On the other side, a low surface energy for $V/III \leq 150$ yields three-dimensional Stranski-Krastanow growth. A qualitative superposition summarizes the theoretical and experimental results in Fig. 6.13. On one hand, the material coverage of the theoretical model on the y-axis is aligned to the experimental data by atomic force microscopy, transmission electron microscopy, and the growth time. On the other hand, the surface energy $\gamma$ of the theoretical model on the x-axis is qualitatively aligned with the logarithmic V/III ratio due to the observed morphological transition and the expected exponential dependence with the chemical potential of ammonia. A deeper analysis of the Stranski-Krastanow growth yields a critical wetting layer thickness of $\theta_{\mathrm{c}} = (2.5 \pm 1)\,\mathrm{ML}$ and GaN quantum dots shaped like truncated pyramids with $\{10\bar{1}3\}$ side facets. Based on theoretical calculations of the surface energies $\gamma_{0001}$, the growth of GaN quantum dots with metalorganic vapor-phase epitaxy is compared to plasma-assisted and ammonia-assisted molecular beam epitaxy and required surface energies for $\gamma_{10\bar{1}3}$

are estimated. Additionally, capped GaN quantum dots exhibit typical optical features like excitons and biexcitons. Further improvements of the capping process are necessary to maintain the excellent quantum dot structures of uncapped samples.

# 7 Conclusion and outlook

In this thesis, epitaxial GaN quantum dots were achieved and studied on tailor-made smooth AlN templates by metalorganic vapor-phase epitaxy. The presented growth studies provide further insights into homoepitaxial and heteroepitaxial growth. In this framework, three major subjects were investigated.

## 7.1 Conclusion

First of all, smooth AlN templates were required to enable a homogeneous GaN nucleation essential for the self-assembled Stranski-Krastanow quantum dot growth. Therefore, the homoepitaxial morphology transition of AlN between the common step-bunching growth and the desired step-flow growth was investigated to achieve smooth surface morphologies characterized by one monolayer high vicinal terraces. A well established analytical model based on adatom kinetics is presented and, additionally, analyzed by a dynamic Monte-Carlo approach providing explicit surface morphologies to derive transition conditions. With this approach, surface morphologies can be studied as a function of adatom diffusion coefficients correlating with growth conditions and the substrate offcut angle associated with the vicinal terrace width. By adjusting only the substrate offcut angle, smooth step-flow growth can be maintained even for growth conditions typically promoting step-bunching growth morphologies. This theoretical correlation was then applied to common homoepitaxial AlN growth conditions yielding step-bunching growth at large substrate offcut angles $\alpha_{\text{offcut}} \geq 0.18°$ and step-flow growth for small substrate offcut angles $\alpha_{\text{offcut}} \leq 0.12°$. Additionally, two different surface terminations could be accessed by controlling an important growth parameter, the V/III ratio. This enables smooth

step-flow AlN buffer layer necessary for homogeneous quantum dot nucleation.

In a second investigation, GaN quantum dots were achieved by employing a growth interruption after a two-dimensional layer growth under high V/III ratios. This procedure is very common for molecular beam epitaxy, although typically gallium-rich conditions are applied. It could be demonstrated for metalorganic vapor-phase epitaxy, that a growth interruption without ammonia is highly correlated with material desorption for surface temperatures above $T_{\mathrm{pyro}} = 750°\mathrm{C}$. By tailoring the process temperature, the initial GaN layer thickness, and the following growth interruption conditions, GaN quantum dots with very small aspect ratios $< 0.1$ are obtained. Additionally, capped samples exhibit typical optical properties of flat elongated GaN quantum dots, like an exciton fine-structure splitting of about $(7.5 \pm 1.0)\,\mathrm{meV}$.

Finally, GaN Stranski-Krastanow quantum dots were achieved by tailoring the surface energy via the V/III ratio. The associated growth morphology transition between two-dimensional Frank-van-der-Merve growth and three-dimensional Stranski-Krastanow growth was described by a qualitative growth model explaining how a change of the surface energy can yield different growth modes for the relevant fixed lattice mismatch of $\epsilon_{\mathrm{GaN/AlN}} = 2.4\%$. Additionally, Frank-van-der-Merve growth was experimentally obtained under high surface energies with a $V/III \geq 300$ and Stranski-Krastanow growth was obtained under low surface energies with a $V/III \leq 150$. A detailed investigation of the Stranski-Krastanow quantum dots confirmed a wetting layer thickness of $(2.5 \pm 1)\,\mathrm{ML}$ and a truncated pyramidal shape with $\{10\bar{1}3\}$ side facets. By comparing the possible surface energy range of the (0001) basal-plane of all three common growth techniques, an estimation of the $\{10\bar{1}3\}$ side-facet surface energy suggests a much smaller growth window for GaN quantum dots by metalorganic vapor-phase epitaxy compared to both molecular beam epitaxy techniques. Additionally, capped GaN samples reveal typical quantum dot features, like excitons and biexcitons with a binding-energy of $(12 \pm 9)\,\mathrm{meV}$.

## 7.2 Outlook

Although GaN quantum dot growth is achieved by metalorganic vapor-phase epitaxy, many questions remain unanswered for an optoelectronic quantum emitter such as superior capping of quantum dot structures, the origin of optical features, doping of the matrix material, and deterministic positioning of quantum dots for mass production. Although typical optical properties of capped GaN quantum dots could be demonstrated,

transmission electron microscopy measurements indicate, that the truncated pyramidal quantum dot shape is not preserved during the capping process with a combination of a low temperature and high temperature AlN capping layer. Furthermore, the origin of single-exciton emission is rather unknown in photoluminescence measurements. Especially, group-III nitride growth is still accompanied with very high defect densities, which can introduce additional radiative recombination center for excitons. Therefore, further investigations of the capping process are required to maintain the excellent quantum dot structure during the capping process and to control the optical properties of single-exciton emission. Additionally, optical correlation measurements are required to confirm single or entangled photon emission at room temperature.

For electron and hole injection, doping of AlGaN with high aluminum content or even AlN is still very challenging, especially for p-doping. Due to the already low lattice mismatch between GaN and AlN, n-type layers require pseudomorphic AlGaN layers or superlattices, which are still coherently strained to AlN with very little perturbation of the delicate energy-balance for Stranski-Krastanow quantum dot formation. In this study, GaN quantum dots have been solely grown by the use of hydrogen as a carrier gas. Due to the correlated low surface energy for the (0001) basal-plane with hydrogen-termination, nitrogen as a carrier gas could extend the growth window for Stranski-Krastanow growth. Additionally, quantum dot nucleation in the presence of low dislocation densities by the use of bulk AlN substrates could yield higher efficiencies, especially, for low density single quantum dot emitter.

If GaN quantum dot based optoelectronic devices with single or entangled photon emission are achieved, they could enable quantum computation and quantum cryptography operating at room temperature. With those building blocks, handheld quantum devices beyond cryogenic labs are imaginable for everyday life applications.

# Bibliography


[1] P. Zoller, T. Beth, D. Binosi, R. Blatt, H. Briegel, D. Bruss, T. Calarco, J. I. Cirac, D. Deutsch, J. Eisert, A. Ekert, C. Fabre, N. Gisin, P. Grangier, M. Grassl, S. Haroche, A. Imamoglu, A. Karlson, J. Kempe, L. Kouwenhoven, S. Kroll, G. Leuchs, M. Lewenstein, D. Loss, N. Lutkenhaus, S. Massar, J. E. Mooij, M. B. Plenio, E. Polzik, S. Popescu, G. Rempe, A. Sergienko, D. Suter, J. Twamley, G. Wendin, R. Werner, A. Winter, J. Wrachtrup, and A. Zeilinger, *Quantum information processing and communication - Strategic report on current status, visions and goals for research in Europe*, European Physical Journal D **36**, 203 (2005).

[2] H. J. Kimble, *The quantum internet*, Nature **453**, 1023 (2008).

[3] I. Aharonovich, D. Englund, and M. Toth, *Solid-state single-photon emitters*, Nature Photonics **10**, 631 (2016).

[4] S. Kako, C. Santori, K. Hoshino, S. Gotzinger, Y. Yamamoto, and Y. Arakawa, *A gallium-nitride single-photon source operating at 200K*, Nature Materials **5**, 887 (2006).

[5] M. J. Holmes, S. Kako, K. Choi, M. Arita, and Y. Arakawa, *Single Photons from a Hot Solid-State Emitter at 350 K*, ACS Photonics **3**, 543 (2016).

[6] Y. Arakawa and H. Sakaki, *Multidimensional quantum well laser and temperature-dependence of its threshold current*, Applied Physics Letters **40**, 939 (1982).

[7] E. F. Schubert, *Physical Foundations of Solid-State Devices*, (E. F. Schubert, Troy, New York, 2009).

[8] T. D. Ladd, F. Jelezko, R. Laflamme, Y. Nakamura, C. Monroe, and J. L. O'Brien, *Quantum computers*, Nature **464**, 45 (2010).

[9] D. Loss and D. P. DiVincenzo, *Quantum computation with quantum dots*, Physical Review A **57**, 120 (1998).

[10] E. Knill, R. Laflamme, and G. J. Milburn, *A scheme for efficient quantum computation with linear optics*, Nature **409**, 46 (2001).

[11] J. I. Cirac and P. Zoller, *Quantum computations with cold trapped ions*, Physical Review Letters **74**, 4091 (1995).

[12] A. K. Ekert, *Quantum Cryptography based on Bell Theorem*, Physical Review Letters **67**, 661 (1991).

[13] L. M. Duan, M. D. Lukin, J. I. Cirac, and P. Zoller, *Long-distance quantum communication with atomic ensembles and linear optics*, Nature **414**, 413 (2001).

[14] J. G. Ren, P. Xu, H. L. Yong, L. Zhang, S. K. Liao, J. Yin, W. Y. Liu, W. Q. Cai, M. Yang, L. Li, K. X. Yang, X. Han, Y. Q. Yao, J. Li, H. Y. Wu, S. Wan, L. Liu, D. Q. Liu, Y. W. Kuang, Z. P. He, P. Shang, C. Guo, R. H. Zheng, K. Tian, Z. C. Zhu, N. L. Liu, C. Y. Lu, R. Shu, Y. A. Chen, C. Z. Peng, J. Y. Wang, and J. W. Pan, *Ground-to-satellite quantum teleportation*, Nature **549**, 70 (2017).

[15] M. Muller, S. Bounouar, K. D. Jons, M. Glassl, and P. Michler, *On-demand generation of indistinguishable polarization-entangled photon pairs*, Nature Photonics **8**, 224 (2014).

[16] T. Heindel, C. Schneider, M. Lermer, S. H. Kwon, T. Braun, S. Reitzenstein, S. Höfling, M. Kamp, and A. Forchel, *Electrically driven quantum dot-micropillar single photon source with 34% overall efficiency*, Applied Physics Letters **96**, 011107 (2010).

[17] J. P. Reithmaier, G. Sek, A. Loffler, C. Hofmann, S. Kuhn, S. Reitzenstein, L. V. Keldysh, V. D. Kulakovskii, T. L. Reinecke, and A. Forchel, *Strong coupling in a single quantum dot-semiconductor microcavity system*, Nature **432**, 197 (2004).

[18] B. G. Levi, *Nobel Prize in Physics recognizes research leading to high-brightness blue LEDs*, Physics Today **67**, 14 (2014).

[19] H. Amano, N. Sawaki, I. Akasaki, and Y. Toyoda, *Metalorganic vapor-phase epitaxial-growth of a high-quality GaN film using an AlN buffer layer*, Applied Physics Letters **48**, 353 (1986).

[20] S. Nakamura, *GaN growth using GaN buffer layer*, Japanese Journal of Applied Physics Part 2-Letters **30**, L1705 (1991).

[21] S. Nakamura, T. Mukai, and M. Senoh, *High-power GaN p-n-junction blue-light-emitting diodes*, Japanese Journal of Applied Physics Part 2-Letters **30**, L1998 (1991).

[22] M. Kneissl and J. Rass (Eds.), *III-Nitride Ultraviolet Emitters*, (Springer, 2016).

[23] H. Hirayama, *Quaternary InAlGaN-based high-efficiency ultraviolet light-emitting diodes*, Journal of Applied Physics **97**, 091101 (2005).

[24] S. J. Pearton, J. C. Zolper, R. J. Shul, and F. Ren, *GaN: Processing, defects, and devices*, Journal of Applied Physics **86**, 1 (1999).

[25] O. Ambacher, *Growth and applications of Group III nitrides*, Journal of Physics D-Applied Physics **31**, 2653 (1998).

[26] N. Ikeda, Y. Niiyama, H. Kambayashi, Y. Sato, T. Nomura, S. Kato, and S. Yoshida, *GaN Power Transistors on Si Substrates for Switching Applications*, Proceedings of the IEEE **98**, 1151 (2010).

[27] C. Kindel, S. Kako, T. Kawano, H. Oishi, Y. Arakawa, G. Honig, M. Winkelnkemper, A. Schliwa, A. Hoffmann, and D. Bimberg, *Exciton fine-structure splitting in GaN/AlN quantum dots*, Physical Review B **81**, 241309(R) (2010).

[28] G. Callsen, A. Carmele, G. Hoenig, C. Kindel, J. Brunnmeier, M. R. Wagner, E. Stock, J. S. Reparaz, A. Schliwa, S. Reitzenstein, A. Knorr, and A. Hoffmann, *Steering photon statistics in single quantum dots: From one- to two-photon emission*, Physical Review B **87**, 245314 (2013).

[29] G. Hoenig, G. Callsen, A. Schliwa, S. Kalinowski, C. Kindel, S. Kako, Y. Arakawa, D. Bimberg, and A. Hoffmann, *Manifestation of unconventional biexciton states in quantum dots*, Nature Communications **5**, 5721 (2014).

[30] S. Kako, *Optical properties of gallium nitride self-assembled quantum dots and application to generation of non-classical light*, Doctoral thesis, The University of Tokyo, 2005.

[31] D. Simeonov, A. Dussaigne, R. Butte, and N. Grandjean, *Complex behavior of biexcitons in GaN quantum dots due to a giant built-in polarization field*, Physical Review B **77**, 075306 (2008).

[32] S. Tanaka, S. Iwai, and Y. Aoyagi, *Self-assembling GaN quantum dots on AlxGa1-xN surfaces using a surfactant*, Applied Physics Letters **69**, 4096 (1996).

[33] X. Q. Shen, S. Tanaka, S. Iwai, and Y. Aoyagi, *The formation of GaN dots on $Al_xGa_{1-x}N$ surfaces using Si in gas-source molecular beam epitaxy*, Applied Physics Letters **72**, 344 (1998).

[34] S. Tanaka, H. Hirayama, Y. Aoyagi, Y. Narukawa, Y. Kawakami, and S. Fujita, *Stimulated emission from optically pumped GaN quantum dots*, Applied Physics Letters **71**, 1299 (1997).

[35] S. Tanaka, J. S. Lee, P. Ramvall, and H. Okagawa, *A UV light-emitting diode incorporating GaN quantum dots*, Japanese Journal of Applied Physics Part 2-Letters **42**, L885 (2003).

[36] C. W. Hu, A. Bell, F. A. Ponce, D. J. Smith, and I. S. T. Tsong, *Growth of self-assembled GaN quantum dots via the vapor-liquid-solid mechanism*, Applied Physics Letters **81**, 3236 (2002).

[37] T. Kondo, K. Saitoh, Y. Yamamoto, T. Maruyama, and S. Naritsuka, *Fabrication of GaN dot structures on Si substrates by droplet epitaxy*, Physica Status Solidi a-Applications and Materials Science **203**, 1700 (2006).

[38] S. Naritsuka, T. Kondo, H. Otsubo, K. Saitoh, Y. Yamamoto, and T. Maruyama, *In situ annealing of GaN dot structures grown by droplet epitaxy on (111) Si substrates*, Journal of Crystal Growth **300**, 118 (2007).

[39] C. Adelmann, J. Brault, D. Jalabert, P. Gentile, H. Mariette, G. Mula, and B. Daudin, *Dynamically stable gallium surface coverages during plasma-assisted molecular-beam epitaxy of (0001) GaN*, Journal of Applied Physics **91**, 9638 (2002).

[40] M. Arita, F. Le Roux, M. J. Holmes, S. Kako, and Y. Arakawa, *Ultraclean Single Photon Emission from a GaN Quantum Dot*, Nano Letters **17**, 2902 (2017).

[41] W. Seifert, N. Carlsson, M. Miller, M. E. Pistol, L. Samuelson, and L. R. Wallenberg, *In-situ growth of quantum dot structures by the Stranski-Krastanow growth mode*, Progress in Crystal Growth and Characterization of Materials **33**, 423 (1996).

[42] U. W. Pohl, *Epitaxy of semiconductors*, Graduate texts in physics, (Springer, Berlin, 2013).

[43] B. Daudin, F. Widmann, G. Feuillet, Y. Samson, M. Arlery, and J. L. Rouviere, *Stranski-Krastanov growth mode during the molecular beam epitaxy of highly strained GaN*, Physical Review B **56**, R7069 (1997).

[44] B. Daudin, F. Widmann, G. Feuillet, C. Adelmann, Y. Samson, M. Arlery, and J. L. Rouviere, *2D/3D growth of GaN by molecular beam epitaxy: towards GaN quantum dots*, Materials Science and Engineering B-Solid State Materials for Advanced Technology **50**, 8 (1997).

[45] F. Widmann, J. Simon, B. Daudin, G. Feuillet, J. L. Rouviere, N. T. Pelekanos, and G. Fishman, *Blue-light emission from GaN self-assembled quantum dots due to giant piezoelectric effect*, Physical Review B **58**, 15989 (1998).

[46] F. Widmann, B. Daudin, G. Feuillet, Y. Samson, J. L. Rouviere, and N. Pelekanos, *Growth kinetics and optical properties of self-organized GaN quantum dots*, Journal of Applied Physics **83**, 7618 (1998).

[47] G. Mula, C. Adelmann, S. Moehl, J. Oullier, and B. Daudin, *Surfactant effect of gallium during molecular-beam epitaxy of GaN on AlN (0001)*, Physical Review B **64**, 195406 (2001).

[48] C. Adelmann, N. Gogneau, E. Sarigiannidou, J. L. Rouviere, and B. Daudin, *GaN islanding by spontaneous rearrangement of a strained two-dimensional layer on (0001) AlN*, Applied Physics Letters **81**, 3064 (2002).

[49] N. Gogneau, D. Jalabert, E. Monroy, T. Shibata, M. Tanaka, and B. Daudin, *Structure of GaN quantum dots grown under "modified Stranski-Krastanow" conditions on AlN*, Journal of Applied Physics **94**, 2254 (2003).

[50] C. Adelmann, B. Daudin, R. A. Oliver, G. A. D. Briggs, and R. E. Rudd, *Nucleation and growth of GaN/AlN quantum dots*, Physical Review B **70**, 125427 (2004).

[51] N. Gogneau, F. Fossard, E. Monroy, S. Monnoye, H. Mank, and B. Daudin, *Effects of stacking on the structural and optical properties of self-organized GaN/AlN quantum dots*, Applied Physics Letters **84**, 4224 (2004).

[52] B. Daudin, *Polar and nonpolar GaN quantum dots*, Journal of Physics-Condensed Matter **20**, 473201 (2008).

[53] M. Peres, A. J. Neves, T. Monteiro, S. Magalhaes, E. Alves, K. Lorenz, H. Okuno-Vila, V. Fellmann, C. Bougerol, and B. Daudin, *Influence of thermal annealing on*

*the structural and optical properties of GaN/AlN quantum dots*, Physica Status Solidi B-Basic Solid State Physics **247**, 1675 (2010).

[54] B. Damilano, N. Grandjean, F. Semond, J. Massies, and M. Leroux, *From visible to white light emission by GaN quantum dots on Si(111) substrate*, Applied Physics Letters **75**, 962 (1999).

[55] B. Damilano, N. Grandjean, J. Massies, and F. Semond, *GaN and GaInN quantum dots: an efficient way to get luminescence in the visible spectrum range*, Applied Surface Science **164**, 241 (2000).

[56] H. Mariette, *Formation of self-assembled quantum dots induced by the Stranski-Krastanow transition: a comparison of various semiconductor systems*, Comptes Rendus Physique **6**, 23 (2005).

[57] B. Damilano, J. Brault, and J. Massies, *Formation of GaN quantum dots by molecular beam epitaxy using $NH_3$ as nitrogen source*, Journal of Applied Physics **118**, 024304 (2015).

[58] M. Miyamura, K. Tachibana, T. Someya, and Y. Arakawa, *Stranski-Krastanow growth of GaN quantum dots by metalorganic chemical vapor deposition*, Journal of Crystal Growth **237**, 1316 (2002).

[59] J. Zhang, S. Li, H. Xiong, W. Tian, Y. Li, Y. Fang, Z. Wu, J. Dai, J. Xu, X. Li, and C. Chen, *Fabrication of low-density GaN/AlN quantum dots via GaN thermal decomposition in MOCVD*, Nanoscale Research Letters **9**, 341 (2014).

[60] M. Miyamura, K. Tachibana, and Y. Arakawa, *High-density and size-controlled GaN self-assembled quantum dots grown by metalorganic chemical vapor deposition*, Applied Physics Letters **80**, 3937 (2002).

[61] M. Miyamura, K. Tachibana, and Y. Arakawa, *UV photoluminescence from size-controlled GaN quantum dots grown by MOCVD*, Physica Status Solidi a-Applied Research **192**, 33 (2002).

[62] K. Hoshino and Y. Arakawa, *Formation of high-density GaN self-assembled quantum dots by MOCVD*, Journal of Crystal Growth **272**, 161 (2004).

[63] D. Simeonov, E. Feltin, J. F. Carlin, R. Butte, M. Ilegems, and N. Grandjean, *Stranski-Krastanov GaN/AlN quantum dots grown by metal organic vapor phase epitaxy*, Journal of Applied Physics **99**, 083509 (2006).

[64] D. Simeonov, E. Feltin, K. Demangeot, C. Pinquier, J. F. Carlin, R. Butte, J. Frandon, and N. Grandjean, *Strain relaxation of AlN epilayers Stranski-Krastanov GaN/AlN quantum dots grown by organic vapor phase epitaxy*, Journal of Crystal Growth **299**, 254 (2007).

[65] J. C. Zhang, B. Meyler, A. Vardi, G. Bahir, and J. Salzman, *Stranski-Krastanov growth of GaN quantum dots on AlN template by metalorganic chemical vapor deposition*, Journal of Applied Physics **104**, 044307 (2008).

[66] S. Kitamura, K. Hiramatsu, and N. Sawaki, *Fabrication of GaN hexagonal pyramids on dot-patterned GaN/sapphire substrates via selective metalorganic vapor phase epitaxy*, Japanese Journal of Applied Physics, Part 2 (Letters) **34**, L1184 (1995).

[67] A. Matsuse, N. Grandjean, B. Damilano, and J. Massies, *Surface morphology of AlN and size dispersion of GaN quantum dots*, Journal of Crystal Growth **274**, 387 (2005).

[68] J. Enslin, F. Mehnke, A. Mogilatenko, K. Bellmann, M. Guttmann, C. Kuhn, J. Rass, N. Lobo-Ploch, T. Wernicke, M. Weyers, and M. Kneissl, *Metamorphic $Al_{0.5}Ga_{0.5}N$:Si on AlN/sapphire for the growth of UVB LEDs*, Journal of Crystal Growth **464**, 185 (2017).

[69] J. L. Rouviere, J. Simon, N. Pelekanos, B. Daudin, and G. Feuillet, *Preferential nucleation of GaN quantum dots at the edge of AlN threading dislocations*, Applied Physics Letters **75**, 2632 (1999).

[70] B. Daudin, G. Feuillet, G. Mula, H. Mariette, J. L. Rouviere, N. Pelekanos, G. Fishman, C. Adelmann, and J. Simon, *Epitaxial growth of GaN, AlN and InN: 2D/3D transition and surfactant effects*, Physica Status Solidi a-Applied Research **176**, 621 (1999).

[71] G. Schmidt, P. Veit, C. Berger, F. Bertram, A. Dadgar, A. Strittmatter, and J. Christen, *Clustered quantum dots in single GaN islands formed at threading dislocations*, Japanese Journal of Applied Physics **55**, 05FF04 (2016).

[72] M. Roeppischer, *Optische Eigenschaften von Aluminium-Galliumnitrid-Halbleitern*, Doctoral thesis, Technischen Universität Berlin, 2011.

[73] N. Hinkley, J. A. Sherman, N. B. Phillips, M. Schioppo, N. D. Lemke, K. Beloy, M. Pizzocaro, C. W. Oates, and A. D. Ludlow, *An Atomic Clock with 10(-18) Instability*, Science **341**, 1215 (2013).

[74] Z. Y. Xu and B. M. Sadler, *Ultraviolet communications: Potential and state-of-the-art*, IEEE Communications Magazine **46**, 67 (2008).

[75] K. X. Sun, B. Allard, S. Buchman, S. Williams, and R. L. Byer, *LED deep UV source for charge management of gravitational reference sensors*, Classical and Quantum Gravity **23**, S141 (2006).

[76] R. C. Evans, *Einführung in die Kristallchemie*, (De Gruyter, 1976).

[77] S. Strite and H. Morkoc, *GaN, AlN, and InN – A review*, Journal of Vacuum Science & Technology B **10**, 1237 (1992).

[78] C. Y. Yeh, Z. W. Lu, S. Froyen, and A. Zunger, *Zinc-blende-wurtzite polytypism in semiconductors*, Physical Review B **46**, 10086 (1992).

[79] O. Ambacher, J. Smart, J. R. Shealy, N. G. Weimann, K. Chu, M. Murphy, W. J. Schaff, L. F. Eastman, R. Dimitrov, L. Wittmer, M. Stutzmann, W. Rieger, and J. Hilsenbeck, *Two-dimensional electron gases induced by spontaneous and piezoelectric polarization charges in N- and Ga-face AlGaN/GaN heterostructures*, Journal of Applied Physics **85**, 3222 (1999).

[80] I. Vurgaftman and J. R. Meyer, *Band parameters for nitrogen-containing semiconductors*, Journal of Applied Physics **94**, 3675 (2003).

[81] W. Paszkowicz, S. Podsiadlo, and R. Minikayev, *Rietveld-refinement study of aluminium and gallium nitrides*, Journal of Alloys and Compounds **382**, 100 (2004).

[82] J. E. Northrup, R. DiFelice, and J. Neugebauer, *Atomic structure and stability of AlN(0001) and* $(000\bar{1})$ *surfaces*, Physical Review B **55**, 13878 (1997).

[83] J. E. Northrup, J. Neugebauer, R. M. Feenstra, and A. R. Smith, *Structure of GaN(0001): The laterally contracted Ga bilayer model*, Physical Review B **61**, 9932 (2000).

[84] Q. Sun, C. D. Yerino, B. Leung, J. Han, and M. E. Coltrin, *Understanding and controlling heteroepitaxy with the kinetic Wulff plot: A case study with GaN*, Journal of Applied Physics **110**, 053517 (2011).

[85] C. G. Van de Walle and J. Neugebauer, *First-principles surface phase diagram for hydrogen on GaN surfaces*, Physical Review Letters **88**, 066103 (2002).

[86] C. G. Van de Walle and J. Neugebauer, *Role of hydrogen in surface reconstructions and growth of GaN*, Journal of Vacuum Science & Technology B **20**, 1640 (2002).

[87] T. Akiyama, D. Obara, K. Nakamura, and T. Ito, *Reconstructions on AlN Polar Surfaces under Hydrogen Rich Conditions*, Japanese Journal of Applied Physics **51**, 018001 (2012).

[88] T. Akiyama, Y. Saito, K. Nakamura, and T. Ito, *Reconstructions on AlN Nonpolar Surfaces in the Presence of Hydrogen*, Japanese Journal of Applied Physics **51**, 048002 (2012).

[89] C. E. Dreyer, A. Janotti, and C. G. Van de Walle, *Absolute surface energies of polar and nonpolar planes of GaN*, Physical Review B **89**, 081305(R) (2014).

[90] A. R. Smith, R. M. Feenstra, D. W. Greve, J. Neugebauer, and J. E. Northrup, *Reconstructions of the GaN* $(000\bar{1})$ *surface*, Physical Review Letters **79**, 3934 (1997).

[91] C. D. Lee, Y. Dong, R. M. Feenstra, J. E. Northrup, and J. Neugebauer, *Reconstructions of the AlN(0001) surface*, Physical Review B **68**, 205317 (2003).

[92] J. Neugebauer, *Surface Structure and Adatom Kinetics of Group-III Nitrides*, in P. Ruterana, M. Albrecht, J. Neugebauer (Eds.), Nitride Semiconductors, (WILEY-VCH Verlag GmbH & Co. KGaA, 2003).

[93] C. A. Neugebauer and J. L. Margrave, *The heat of formation of aluminum nitride*, Zeitschrift Fur Anorganische Und Allgemeine Chemie **290**, 82 (1957).

[94] R. Madar, G. Jacob, J. Hallais, and R. Fruchart, *High-pressure solution growth of GaN*, Journal of Crystal Growth **31**, 197 (1975).

[95] J. Karpinski and S. Porowski, *High-pressure thermodynamics of GaN*, Journal of Crystal Growth **66**, 11 (1984).

[96] M. R. Ranade, F. Tessier, A. Navrotsky, V. J. Leppert, S. H. Risbud, F. J. DiSalvo, and C. M. Balkas, *Enthalpy of formation of gallium nitride*, Journal of Physical Chemistry B **104**, 4060 (2000).

[97] T. Zywietz, J. Neugebauer, and M. Scheffler, *Adatom diffusion at GaN (0001) and* $(000\bar{1})$ *surfaces*, Applied Physics Letters **73**, 487 (1998).

[98] V. Jindal and F. Shahedipour-Sandvik, *Density functional theoretical study of surface structure and adatom kinetics for wurtzite AlN*, Journal of Applied Physics **105**, 084902 (2009).

[99] I. V. Markov, *Nucleation at Surfaces*, in G. Dhanaraj, K. Byrappa, V. Prasad, M. Dudley (Eds.), Springer Handbook of Crystal Growth, (Springer Berlin Heidelberg, 2010).

[100] D. F. Davidson, K. Kohsehoinghaus, A. Y. Chang, and R. K. Hanson, *A pyrolysis mechanism for ammonia*, International Journal of Chemical Kinetics **22**, 513 (1990).

[101] N. Dietz, M. Strassburg, and V. Woods, *Real-time optical monitoring of ammonia flow and decomposition kinetics under high-pressure chemical vapor deposition conditions*, Journal of Vacuum Science & Technology A **23**, 1221 (2005).

[102] V. A. Fonoberov and A. A. Balandin, *Optical properties of wurtzite and zinc-blende GaN/AlN quantum dots*, Journal of Vacuum Science & Technology B **22**, 2190 (2004).

[103] N. T. Pelekanos, G. E. Dialynas, J. Simon, H. Mariette, and B. Daudin, *GaN quantum dots: from basic understanding to unique applications*, Journal of Physics: Conference Series **10**, 61 (2005).

[104] G. M. O. Hoenig, *Multi particle states in semiconductor quantum dots*, Doctoral thesis, Technische Universität Berlin, 2015.

[105] C. H. Kindel, *Study on Optical Polarization in Hexagonal Gallium Nitride Quantum Dots*, Doctoral thesis, University of Tokio, 2010.

[106] G. Callsen, *Advanced optical signatures of single, wurtzite GaN quantum dots*, Doctoral thesis, Technische Universität Berlin, 2015.

[107] R. Seguin, A. Schliwa, S. Rodt, K. Potschke, U. W. Pohl, and D. Bimberg, *Size-dependent fine-structure splitting in self-organized InAs/GaAs quantum dots*, Physical Review Letters **95**, 257402 (2005).

[108] A. Schliwa and M. Winkelnkemper, *Theory of Excitons in InGaAs/GaAs Quantum Dots*, in D. Bimberg (Ed.), Semiconductor Nanostructures, (Springer-Verlag Berlin Heidelberg, 2008).

[109] M. Abbarchi, C. Mastrandrea, T. Kuroda, T. Mano, A. Vinattieri, K. Sakoda, and M. Gurioli, *Poissonian statistics of excitonic complexes in quantum dots*, Journal of Applied Physics **106**, 053504 (2009).

[110] R. Schwoebel and E. J. Shipsey, *Step motion on crystal surfaces*, Journal of Applied Physics **37**, 3682 (1966).

[111] R. Schwoebel, *Step motion on crystal surfaces .2*, Journal of Applied Physics **40**, 614 (1969).

[112] D. P. Landau and K. Binder, *A Guide to Monte Carlo Simulations in Statistical Physics*, (Cambridge University Press, 2000).

[113] T. Shitara and T. Nishinaga, *Surface-diffusion length of gallium during MBE growth on the various misoriented GaAs(001) substrates*, Japanese Journal of Applied Physics Part 1-Regular Papers Short Notes & Review Papers **28**, 1212 (1989).

[114] W. K. Burton, N. Cabrera, and F. C. Frank, *The growth of crystals and the equilibrium structure of their surfaces*, Philosophical Transactions of the Royal Society of London Series a-Mathematical and Physical Sciences **243**, 299 (1951).

[115] G. Ehrlich and F. G. Hudda, *Atomic view of surface self-diffusion – tungsten on tungsten*, Journal of Chemical Physics **44**, 1039 (1966).

[116] V. A. Shchukin, N. N. Ledentsov, and D. Bimberg, *Epitaxy of Nanostructures*, (Springer, 2003).

[117] A. Strittmatter, *Epitaxial growth of nitride quantum dots*, in B. Gil (Ed.), III-Nitride Semiconductors and their Modern Devices, (Oxford University Press, 2013).

[118] Gwyddion, *2.47*, Software, GNU License, 2016.

[119] J. Stellmach, M. Pristovsek, O. Savas, J. Schlegel, E. V. Yakovlev, and M. Kneissl, *High aluminium content and high growth rates of AlGaN in a close-coupled showerhead MOVPE reactor*, Journal of Crystal Growth **315**, 229 (2011).

[120] Veeco, *MultiMode$^{TM}$ SPM Instruction Manual*, Manual, Digital Instruments Veeco Metrology Group, 1999.

[121] Bruker, *Dimension Icon User Guide*, Manual, Bruker, 2014.

[122] G. Schmidt, C. Berger, P. Veit, S. Metzner, F. Bertram, J. Blaesing, A. Dadgar, A. Strittmatter, J. Christen, G. Callsen, S. Kalinowski, and A. Hoffmann, *Direct evidence of single quantum dot emission from GaN islands formed at threading dislocations using nanoscale cathodoluminescence: A source of single photons in the ultraviolet*, Applied Physics Letters **106**, 252101 (2015).

[123] X. L. Wang and V. Voliotis, *Epitaxial growth and optical properties of semiconductor quantum wires*, Journal of Applied Physics **99**, 121301 (2006).

[124] M. Fuechsle, J. A. Miwa, S. Mahapatra, H. Ryu, S. Lee, O. Warschkow, L. C. L. Hollenberg, G. Klimeck, and M. Y. Simmons, *A single-atom transistor*, Nature Nanotechnology **7**, 242 (2012).

[125] F. Lelarge, B. Dagens, J. Renaudier, R. Brenot, A. Accard, F. van Dijk, D. Make, O. Le Gouezigou, J. G. Provost, F. Poingt, J. Landreau, O. Drisse, E. Derouin, B. Rousseau, F. Pommereau, and G. H. Duan, *Recent advances on InAs/InP quantum dash based, semiconductor lasers and optical amplifiers operating at 1.55$\mu m$*, Ieee Journal of Selected Topics in Quantum Electronics **13**, 111 (2007).

[126] V. Kueller, *Versetzungsreduzierte AlN- und AlGaN-Schichten als Basis für UV LEDs*, Doctoral thesis, Technischen Universität Berlin, 2014.

[127] I. Bryan, Z. Bryan, S. Mita, A. Rice, J. Tweedie, R. Collazo, and Z. Sitar, *Surface kinetics in AlN growth: A universal model for the control of surface morphology in III-nitrides*, Journal of Crystal Growth **438**, 81 (2016).

[128] M. Pristovsek, K. Bellmann, F. Mehnke, J. Stellmach, T. Wernicke, and M. Kneissl, *Surface reconstructions of (0001) AlN during metal-organic vapor phase epitaxy*, Physica Status Solidi B **254**, 1600711 (2017).

[129] J. Myslivecek, C. Schelling, G. Springholz, F. Schaffler, B. Voigtlander, and P. Smilauer, *On the origin of the kinetic growth instability of homoepitaxy on Si(001)*, Materials Science and Engineering B-Solid State Materials for Advanced Technology **89**, 410 (2002).

[130] A. Pascale, I. Berbezier, A. Ronda, A. Videcoq, and A. Pimpinelli, *Self-organization of step bunching instability on vicinal substrate*, Applied Physics Letters **89**, 104108 (2006).

[131] M. Shinohara and N. Inoue, *Behavior and mechanism of step bunching during metalorganic vapor-phase epitaxy of GaAs*, Applied Physics Letters **66**, 1936 (1995).

[132] A. L. S. Chua, E. Pelucchi, A. Rudra, B. Dwir, E. Kapon, A. Zangwill, and D. D. Vvedensky, *Theory and experiment of step bunching on misoriented GaAs(001) during metalorganic vapor-phase epitaxy*, Applied Physics Letters **92**, 013117 (2008).

[133] V. Thevenot, V. Souliere, H. Dumont, Y. Monteil, J. Bouix, P. Regreny, and T. M. Duc, *Behaviour of vicinal InP surfaces grown by MOVPE: Exploitation of AFM images*, Journal of Crystal Growth **170**, 251 (1997).

[134] A. Gocalinska, M. Manganaro, E. Pelucchi, and D. D. Vvedensky, *Surface organization of homoepitaxial InP films grown by metalorganic vapor-phase epitaxy*, Physical Review B **86**, 165307 (2012).

[135] X. Q. Shen, M. Shimizu, and H. Okumura, *Impact of vicinal sapphire (0001) substrates on the high-quality AlN films by plasma-assisted molecular beam epitaxy*, Japanese Journal of Applied Physics Part 2-Letters **42**, L1293 (2003).

[136] X. Q. Shen and H. Okumura, *Plasma-assisted molecular beam epitaxial growth of AlN films on vicinal sapphire (0001) substrates*, Silicon Carbide and Related Materials 2003, Prts 1 and 2 **457-460**, 1553 (2004).

[137] A. Pimpinelli, J. Villain, D. E. Wolf, J. J. Metois, J. C. Heyraud, I. Elkinani, and G. Uimin, *Equilibrium step dynamics on vicinal surfaces*, Surface Science **295**, 143 (1993).

[138] A. Pimpinelli, I. Elkinani, A. Karma, C. Misbah, and J. Villain, *Step motions on high-temperature vicinal surfaces*, Journal of Physics-Condensed Matter **6**, 2661 (1994).

[139] M. H. Xie, S. Y. Leung, and S. Y. Tong, *What causes step bunching-negative Ehrlich-Schwoebel barrier versus positive incorporation barrier*, Surface Science **515**, L459 (2002).

[140] W. Hong, H. N. Lee, M. Yoon, H. M. Christen, D. H. Lowndes, Z. G. Suo, and Z. Y. Zhang, *Persistent step-flow growth of strained films on vicinal substrates*, Physical Review Letters **95**, 095501 (2005).

[141] Z. Y. Fan and N. Newman, *Experimental determination of the rates of decomposition and cation desorption from AlN surfaces*, Materials Science and Engineering B-Solid State Materials for Advanced Technology **87**, 244 (2001).

[142] Y. Kumagai, K. Akiyama, R. Togashi, H. Murakami, M. Takeuchi, T. Kinoshita, K. Takada, Y. Aoyagi, and A. Koukitu, *Polarity dependence of AlN (0001) decomposition in flowing $H_2$*, Journal of Crystal Growth **305**, 366 (2007).

[143] Mathematica, *10.0.2*, Software, Wolfram, 2014.

[144] M. H. Xie, S. M. Seutter, W. K. Zhu, L. X. Zheng, H. S. Wu, and S. Y. Tong, *Anisotropic step-flow growth and island growth of GaN(0001) by molecular beam epitaxy*, Physical Review Letters **82**, 2749 (1999).

[145] B. Damilano, N. Grandjean, F. Semond, J. Massies, and M. Leroux, *Violet to orange room temperature luminescence from GaN quantum dots on Si(111) substrates*, Physica Status Solidi B-Basic Research **216**, 451 (1999).

[146] T. Bretagnon, P. Lefebvre, P. Valvin, R. Bardoux, T. Guillet, T. Taliercio, B. Gil, N. Grandjean, F. Semond, B. Damilano, A. Dussaigne, and J. Massies, *Radiative lifetime of a single electron-hole pair in GaN/AlN quantum dots*, Physical Review B **73**, 113304 (2006).

[147] K. Hoshino and Y. Arakawa, *Effect of thermal treatment on structure of GaN self-assembled quantum dots grown by MOCVD*, Physica Status Solidi C **0**, 1101 (2003).

[148] S. Guha, N. A. Bojarczuk, and D. W. Kisker, *Surface lifetimes of Ga and growth behavior on GaN(0001) surfaces during molecular beam epitaxy*, Applied Physics Letters **69**, 2879 (1996).

[149] N. Grandjean, J. Massies, F. Semond, S. Y. Karpov, and R. A. Talalaev, *GaN evaporation in molecular-beam epitaxy environment*, Applied Physics Letters **74**, 1854 (1999).

[150] O. Ambacher, M. S. Brandt, R. Dimitrov, T. Metzger, M. Stutzmann, R. A. Fischer, A. Miehr, A. Bergmaier, and G. Dollinger, *Thermal stability and desorption of Group III nitrides prepared by metal organic chemical vapor deposition*, Journal of Vacuum Science & Technology B **14**, 3532 (1996).

[151] C. Kim, I. K. Robinson, J. Myoung, K. Shim, M. C. Yoo, and K. Kim, *Critical thickness of GaN thin films on sapphire(0001)*, Applied Physics Letters **69**, 2358 (1996).

[152] R. Held, D. E. Crawford, A. M. Johnston, A. M. Dabiran, and P. I. Cohen, *N-limited versus Ga-limited growth on GaN(0001) by MBE using $NH_3$*, Surface Review and Letters **5**, 913 (1998).

[153] R. Groh, G. Gerey, L. Bartha, and J. I. Pankove, *Thermal-decomposition of GaN in vacuum*, Physica Status Solidi a-Applied Research **26**, 353 (1974).

[154] Z. A. Munir and A. W. Searcy, *Activation energy for sublimation of gallium nitride*, Journal of Chemical Physics **42**, 4223 (1965).

[155] D. Simeonov, *Synthesis and optical investigation of single polar GaN/AlN quantum dots*, Doctoral thesis, École polytechnique fédérale de Lausanne, 2009.

[156] G. Honig, S. Rodt, G. Callsen, I. A. Ostapenko, T. Kure, A. Schliwa, C. Kindel, D. Bimberg, and A. Hoffmann, *Identification of electric dipole moments of excitonic complexes in nitride-based quantum dots*, Physical Review B **88**, 045309 (2013).

[157] K. Bellmann, F. Tabataba-Vakili, T. Wernicke, A. Strittmatter, G. Callsen, A. Hoffmann, and M. Kneissl, *Desorption induced GaN quantum dots on (0001) AlN by MOVPE*, Physica Status Solidi-Rapid Research Letters **9**, 526 (2015).

[158] I. Daruka and A. L. Barabasi, *Dislocation-free island formation in heteroepitaxial growth: A study at equilibrium*, Physical Review Letters **79**, 3708 (1997).

[159] C. Adelmann, B. Daudin, E. Monroy, E. Sarigiannidou, J. L. Rouviere, Y. Hori, J. Brault, N. Gogneau, S. Fanget, and C. Bru-Chevallier, *Controlling the morphology of GaN layers grown on AlN in Ga self-surfactant conditions: From quantum wells to quantum dots*, Physica Status Solidi B-Basic Research **234**, 931 (2002).

[160] E. J. Tarsa, B. Heying, X. H. Wu, P. Fini, S. P. DenBaars, and J. S. Speck, *Homoepitaxial growth of GaN under Ga-stable and N-stable conditions by plasma-assisted molecular beam epitaxy*, Journal of Applied Physics **82**, 5472 (1997).

[161] P. Sohi, D. Martin, and N. Grandjean, *Critical thickness of GaN on AlN: impact of growth temperature and dislocation density*, Semiconductor Science and Technology **32**, 075010 (2017).

[162] N. Grandjean, B. Damilano, and J. Massies, *Group-III nitride quantum heterostructures grown by molecular beam epitaxy*, Journal of Physics-Condensed Matter **13**, 6945 (2001).

[163] S. Y. Karpov, R. A. Talalaev, Y. N. Makarov, N. Grandjean, J. Massies, and B. Damilano, *Surface kinetics of GaN evaporation and growth by molecular-beam epitaxy*, Surface Science **450**, 191 (2000).

[164] J. Brault, B. Damilano, A. Kahouli, S. Chenot, M. Leroux, B. Vinter, and J. Massies, *Ultra-violet GaN/$Al_{0.5}Ga_{0.5}N$ quantum dot based light emitting diodes*, Journal of Crystal Growth **363**, 282 (2013).

[165] J. Brault, S. Matta, T. H. Ngo, D. Rosales, M. Leroux, B. Damilano, M. Al Khalfioui, F. Tendille, S. Chenot, P. De Mierry, J. Massies, and B. Gil, *Ultraviolet light emitting diodes using III-N quantum dots*, Materials Science in Semiconductor Processing **55**, 95 (2016).

[166] J. Brault, S. Matta, T. H. Ngo, M. Korytov, D. Rosales, B. Damilano, M. Leroux, P. Vennegues, M. Al Khalfioui, A. Courville, O. Tottereau, J. Massies, and B. Gil, *Investigation of $Al_yGa_{1-y}N/Al_{0.5}Ga_{0.5}N$ quantum dot properties for the design of ultraviolet emitters*, Japanese Journal of Applied Physics **55**, 05FG06 (2016).

[167] S. Kako, M. Miyamura, K. Hoshino, and Y. Arakawa, *Long-lived excitons up to 1$\mu$s in GaN/AlN self-assembled quantum dots*, Physica Status Solidi B-Basic Research **240**, 388 (2003).

[168] K. Hoshino, S. Kako, and Y. Arakawa, *Stranski-Krastanow growth of stacked GaN quantum dots with intense photoluminescence*, Physica Status Solidi B-Basic Research **240**, 322 (2003).

[169] K. Hoshino, S. Kako, and Y. Arakawa, *Formation and optical properties of stacked GaN self-assembled quantum dots grown by metalorganic chemical vapor deposition*, Applied Physics Letters **85**, 1262 (2004).

[170] I. Daruka and A. L. Barabasi, *Equilibrium phase diagrams for dislocation free self-assembled quantum dots*, Applied Physics Letters **72**, 2102 (1998).

[171] T. Akiyama, K. Nakamura, and T. Ito, *Ab initio-based study for adatom kinetics on AlN(0001) surfaces during metal-organic vapor-phase epitaxy growth*, Applied Physics Letters **100**, 251601 (2012).

[172] M. Mesrine, N. Grandjean, and J. Massies, *Efficiency of $NH_3$ as nitrogen source for GaN molecular beam epitaxy*, Applied Physics Letters **72**, 350 (1998).

[173] D. Leonard, K. Pond, and P. M. Petroff, *Critical layer thickness for self-assembled InAs islands on GaAs*, Physical Review B **50**, 11687 (1994).

[174] J. Brown, F. Wu, P. M. Petroff, and J. S. Speck, *GaN quantum dot density control by rf-plasma molecular beam epitaxy*, Applied Physics Letters **84**, 690 (2004).

[175] V. Chamard, T. Schulli, M. Sztucki, T. H. Metzger, E. Sarigiannidou, J. L. Rouviere, M. Tolan, C. Adelmann, and B. Daudin, *Strain distribution in nitride quantum dot multilayers*, Physical Review B **69**, 125327 (2004).

[176] J. E. Northrup and J. Neugebauer, *Theory of GaN* $(10\bar{1}0)$ *and* $(11\bar{2}0)$ *surfaces*, Physical Review B **53**, 10477 (1996).

[177] H. Li, L. Geelhaar, H. Riechert, and C. Draxl, *Computing Equilibrium Shapes of Wurtzite Crystals: The Example of GaN*, Physical Review Letters **115**, 085503 (2015).

[178] D. Jalabert, J. Coraux, H. Renevier, B. Daudin, M. H. Cho, K. B. Chung, D. W. Moon, J. M. Llorens, N. Garro, A. Cros, and A. Garcia-Cristobal, *Deformation profile in GaN quantum dots: Medium-energy ion scattering experiments and theoretical calculations*, Physical Review B **72**, 115301 (2005).

[179] E. Sarigiannidou, E. Monroy, B. Daudin, J. L. Rouviere, and A. D. Andreev, *Strain distribution in GaN/AlN quantum-dot superlattices*, Applied Physics Letters **87**, 203112 (2005).

[180] M. Korytov, J. A. Budagosky, J. Brault, T. Huault, M. Benaissa, T. Neisius, J. L. Rouviere, and P. Vennegues, *Mechanism of GaN quantum dot overgrowth by* $Al_{0.5}Ga_{0.5}N$*: Strain evolution and phase separation*, Journal of Applied Physics **111**, 084309 (2012).

[181] T. Saito and Y. Arakawa, *Strain energy distribution in GaN and InGaN quantum dots on AlN buffer layers: A valence-force-field approach*, In *25th International Symposium on Compound Semiconductors*, Institute of Physics Conference Series, pp. 741–745, BRISTOL, 1999, Iop Publishing Ltd.

[182] I. A. Ostapenko, G. Hoenig, S. Rodt, A. Schliwa, A. Hoffmann, D. Bimberg, M.-R. Dachner, M. Richter, A. Knorr, S. Kako, and Y. Arakawa, *Exciton acoustic-phonon coupling in single GaN/AlN quantum dots*, Physical Review B **85**, 081303(R) (2012).

[183] I. Ostapenko, *Influence of defects, phonons and strain on the luminescence properties of nitride- and arsenide-based quantum dots*, Doctoral thesis, Technische Universität Berlin, 2012.

[184] M.-R. Dachner, *Influence of phonons on light emission and propagation in semiconductor nano optics*, Doctoral thesis, Technische Universität Berlin, 2013.

[185] T. Saito and Y. Arakawa, *Atomic structure and phase stability of $In_xGa_{1-x}N$ random alloys calculated using a valence-force-field method*, Physical Review B **60**, 1701 (1999).

[186] C. Tessarek, S. Figge, T. Aschenbrenner, S. Bley, A. Rosenauer, M. Seyfried, J. Kalden, K. Sebald, J. Gutowski, and D. Hommel, *Strong phase separation of strained $In_xGa_{1-x}N$ layers due to spinodal and binodal decomposition: Formation of stable quantum dots*, Physical Review B **83**, 115316 (2011).

[187] J. Coraux, B. Amstatt, J. A. Budagoski, E. Bellet-Amalric, J. L. Rouviere, V. Favre-Nicolin, M. G. Proietti, H. Renevier, and B. Daudin, *Mechanism of GaN quantum dots capped with AlN: An AFM, electron microscopy, and x-ray anomalous diffraction study*, Physical Review B **74**, 195302 (2006).

[188] Z. Q. Qi, S. L. Li, S. C. Sun, X. H. Huang, Y. Li, W. Zhang, W. Ye, J. N. Dai, Y. Tian, Y. Y. Fang, and C. Q. Chen, *Optical performance improvement of GaN/AlN quantum dots via a two-step grown caplayer*, Journal of Alloys and Compounds **651**, 673 (2015).

# List of publications

**Peer-reviewed Articles**

K. Bellmann, U. W. Pohl, C. Kuhn, T. Wernicke, and M. Kneissl, *Controlling the morphology transition between step-flow growth and step-bunching growth*, Journal of Crystal Growth **478**, 197 (2017).

M. Pristovsek, K. Bellmann, F. Mehnke, J. Stellmach, T. Wernicke, and M. Kneissl, *Surface reconstructions of (0001) AlN during metal-organic vapor phase epitaxy*, physica status solidi (b) **254**, 1600711 (2017).

J. Enslin, F. Mehnke, A. Mogilatenko, K. Bellmann, M. Guttmann, C. Kuhn, J. Rass, N. Lobo-Ploch, T. Wernicke, M. Weyers, and M. Kneissl, *Metamorphic Al0.5Ga0.5N:Si on AlN/sapphire for the growth of UVB LEDs*, Journal of Crystal Growth **464**, 185 (2017).

M. Rychetsky, I. Koslow, B. Avinc, J. Rass, T. Wernicke, K. Bellmann, L. Sulmoni, V. Hoffmann, M. Weyers, J. Wild, J. Zweck, B. Witzigmann, and M. Kneissl, *Determination of polarization fields in group III-nitride heterostructures by capacitance-voltage-measurements*, Journal of Applied Physics **119**, 095713 (2016).

A. Mogilatenko, J. Enslin, A. Knauer, F. Mehnke, K. Bellmann, T. Wernicke, M. Weyers, and M. Kneissl, *V-pit to truncated pyramid transition in AlGaN-based heterostructures*, Semiconductor Science and Technology **30**, 114010 (2015).

K. Bellmann, F. Tabataba-Vakili, T. Wernicke, A. Strittmatter, G. Callsen, A. Hoffmann, and M. Kneissl, *Desorption induced GaN quantum dots on (0001) AlN by MOVPE*, Physica Status Solidi – Rapid Research Letters **9**, 526 (2015).

A. Kadir, K. Bellmann, T. Simoneit, M. Pristovsek, and M. Kneissl, *Influence of group*

*III and group V partial pressures on the size and density of InGaN quantum dots in MOVPE*, Physica Status Solidi a – Applications and Materials Science **209**, 2487 (2012).

K. Bellmann, T. Ernst, A. Strittmatter, T. Markurt, M. Albrecht, T. Wernicke, and M. Kneissl *Surface energy induced growth transition of GaN on (0001) AlN*, manuscript in preparation based on chapter 6.

**Conference contributions**

K. Bellmann, U. W. Pohl, A. Sabelfeld, C. Kuhn, T. Wernicke, and M. Kneissl, *Surface-morphology transition between step-flow growth and step bunching*, DPG Frühjahrstagung 2017 Dresden.

K. Bellmann, U. W. Pohl, A. Sabelfeld, C. Kuhn, T. Wernicke, and M. Kneissl, *Phase diagram for island growth, step flow growth and step bunching*, IWN 2016 Orlando.

K. Bellmann, U. W. Pohl, A. Sabelfeld, C. Kuhn, T. Wernicke, and M. Kneissl, *AlN growth transition between step flow growth and step bunching*, DPG Frühjahrstagung 2016 Regensburg.

K. Bellmann, T. Ernst, A. Reuper, G. Schmidt, A. Strittmatter, T. Wernicke, J. Christen, and M. Kneissl *Surface energy control and GaN quantum dot growth by MOVPE*, ICNS 2015 Beijing.

K. Bellmann, D. Henning, C. Reich, T. Wernicke, V. Küller, A. Knauer, and M. Kneissl *Selective GaN QD nucleation on low defect density ELO AlN (0001)*, ICDS 2015 Espoo.

K. Bellmann, T. Ernst, A. Strittmatter, T. Wernicke, and M. Kneissl *GaN QDs on AlN grown by MOVPE*, DPG Frühjahrstagung 2015 Berlin.

K. Bellmann, T. Ernst, A. Strittmatter, T. Wernicke, and M. Kneissl *GaN Quanten-punktwachstum auf (0001) AlN*, DGKK 2014.

K. Bellmann, F. Tabataba-Vakili, T. Wernicke, S. Kalinowski, G. Callsen, A. Hoffmann, G. Schmidt, P. Veit, F. Bertram, J. Christen, A. Strittmatter, G. Callsen, A. Hoffmann, and M. Kneissl, *Desorption induced GaN QDs grown on AlN (0001)*, PLMCN 2014 Montpellier.

K. Bellmann, F. Tabataba-Vakili, A. Strittmatter, S. Kalinowski, V. Küller, A. Knauer, T. Wernicke, M. Weyers, and M. Kneissl *GaN Quantenpunktwachstum auf (0001) AlN*,

DGKK 2013.

K. Bellmann, D. Dinh, C. Reich, A. Strittmatter, V. Küller, A. Knauer, M. Weyers, T. Wernicke, M. Pristovsek, and M. Kneissl *Dreidimensionales GaN Wachstum auf (0001) AlN*, DGKK 2012.

K. Bellmann, T. Simoneit, A. Kadir, M. Pristovsek, and M. Kneissl *Growth mechanisms of thin GaN on AlN*, DPG Frühjahrstagung 2012 Berlin.

K. Bellmann, A. Kadir, M. Pristovsek, and M. Kneissl *Control of size and density of InGaN QDs*, DGKK 2011.

K. Bellmann, A. Kadir, T. Schwaner, T. Kolbe, J. Stellmach, and M. Kneissl *Green electroluminescence from InGaN quantum dots grown by MOVPE*, iNow 2011 St. Petersburg/Würzburg.

# List of Figures


2.1 Schematic wurtzite crystal structure . . . . . 6
2.2 Bandgap of AlN and GaN . . . . . 7
2.3 Schematic 2x2 Ga and N terminated surface reconstruction . . . . . 8
2.4 Theoretical formation energy of different surface reconstructions . . . . . 9
2.5 Chemical potential $\mu_N$ as a function of partial pressure $p_N$ . . . . . 11
2.6 Schematic band diagram of GaN quantum-dots inside AlN . . . . . 13
2.7 Schematic surface cross section with vicinal terraces $l_0$ (substrate offcut $\alpha$) 15
2.8 Schematic surface energy potential for adatom kinetics . . . . . 16
2.9 Schematic diagram of terrace ledge kink model . . . . . 17
2.10 Three major surface morphologies of homoepitaxy . . . . . 19
2.11 Three major surface morphologies of heteroepitaxy . . . . . 21

3.1 Schematic reactor diagram of metalorganic vapor-phase epitaxy . . . . . 24
3.2 Schematic surface reactions inside a reactor . . . . . 25
3.3 Atomic force microscopy measurement signal . . . . . 27
3.4 Atomic force microscopy data analysis . . . . . 28
3.5 Electron beam lithography process steps . . . . . 29
3.6 Electron beam lithography processed mesa structure properties . . . . . 30
3.7 Schematic setup of micro photoluminescence . . . . . 32

4.1 Schematic cross section with adatom fluxes . . . . . 37
4.2 Adatom density and flux for different vicinal terrace widths $l_0$ . . . . . 40
4.3 Adatom density and flux for different diffusion constants $k_-, k_+, \lambda_s, C_s$ . . 43
4.4 Adatom incorporation for Monte-Carlo approach . . . . . 46
4.5 Schematic iteration chain of the Monte-Carlo algorithm . . . . . 47
4.6 Simulated layer growth at different conditions . . . . . 49
4.7 Homoepitaxial morphology phase diagrams as function of $k_+, k_-, \lambda_s$ . . . 51
4.8 Homoepitaxial morphology phase diagrams as function of $C_s, k_-, \lambda_s$ . . . . 52

4.9 Homoepitaxial morphology phase diagram as function of $l_0, k_-, \lambda_s$ . . . . . 54
4.10 AlN Sample structure . . . . . 55
4.11 AlN surface morphology for different substrate offcuts . . . . . 56
4.12 Surface morphology phase diagram with different AlN growth conditions . 57
4.13 Superposition of homoepitaxial morphological data and analytical model . 60

5.1 Desorption GaN sample structure . . . . . 63
5.2 GaN surface morphologies for different growth interruption times $t_{GRI}$ . . 65
5.3 Quantitative analysis of surface morphology for different $t_{GRI}$ . . . . . 65
5.4 GaN surface morphologies for different desorption temperatures $T_{GRI}$ . . . 67
5.5 Determination of activation energy for GaN desorption . . . . . 67
5.6 Structural and optical properties of desorption induced GaN quantum dots 68
5.7 Optical properties of individual desorption induced GaN quantum dots . . 70

6.1 Heteroepitaxial morphology phase diagram as function of $H$, $\epsilon$ . . . . . 79
6.2 Heteroepitaxial morphology phase diagram as function of $H$, $\gamma$ . . . . . 82
6.3 Surface energy induced GaN sample structure . . . . . 83
6.4 Surface morphology of GaN grown under high V/III ratio . . . . . 84
6.5 Surface morphology of GaN grown under different V/III ratios . . . . . 85
6.6 Surface morphology of GaN grown under low V/III ratio . . . . . 87
6.7 Quantitative surface morphology analysis of wetting layer thickness . . . . 89
6.8 Scanning transmission electron microscopy images of GaN quantum dots . 90
6.9 Side facet analysis of a GaN quantum dot . . . . . 91
6.10 Influence of the surface energy of different facets on the 2D to 3D transition 93
6.11 Optical properties of capped Stranski-Krastanow GaN quantum dots . . . 95
6.12 Structural and optical properties of capped GaN quantum dots . . . . . 97
6.13 Superposition of heteroepitaxial morphological data and analytical model 99

# List of growth samples

**2 Basic principles of group-III nitride epitaxy**

Fig. 2.10 TS2183, TS3449-2, TS3449-3

**3 Experimental methods**

Fig. 3.3 TS2961

Fig. 3.4 TS2961

Fig. 3.6 TS2348, E4443-9Db

**4 Achieving smooth step-flow AlN surfaces**

Fig. 4.11 TS3453-1, TS3453-2, TS3453-3

Fig. 4.12 TS3457-1, TS3457-2, TS3457-3,
TS3455-1, TS3455-2, TS3455-3,
TS3449-1, TS3449-2, TS3449-3,
TS3453-1, TS3453-2, TS3453-3,
TS3451-1, TS3451-2, TS3451-3

**5 Desorption induced GaN quantum dot growth**

Fig. 5.2 TS2142, TS2128, TS2129,
TS2157, TS2158, TS2161

Fig. 5.3 TS2128, TS2129, TS2157, TS2158

Fig. 5.4 TS2155, TS2154, TS2128,
TS2149, TS2151, TS2156

Fig. 5.5 TS2128, TS2149, TS2151, TS2156

Fig. 5.6a TS2317

Fig. 5.6b TS2348

Fig. 5.7 TS2348

**6 Surface energy induced 2D to 3D transition in GaN**

| | |
|---|---|
| Fig. 6.4 | TS3449-2, TS2979, TS2980, TS2981, TS2983 |
| Fig. 6.6 | TS3453-3, TS2953, TS2954, TS2959, TS2960, TS2961, TS2962, TS2955, TS2956 |
| Fig. 6.7a | TS2953, TS2954, TS2959, TS2960, TS2961, TS2962, TS2955, TS2956 |
| Fig. 6.7b | TS2960, TS2961, TS2962, TS2955, TS2956 |
| Fig. 6.8 | TS2962 |
| Fig. 6.5 | TS2981, TS2986, TS2987, TS2988, TS2955 |
| Fig. 6.9 | TS2962 |
| Fig. 6.11 | TS2966 |
| Fig. 6.12 | TS2966 |

# Acknowledgments

I would like to thank everyone, who supported me during my thesis. First of all, I thank Prof. Dr. Michael Kneissl for giving me the opportunity and trust to work in his workgroup. Then, I am grateful to the whole committee, Prof. Dr. Michael Lehmann, Prof. Dr. Michael Kneissl, Prof. Dr. Ferdinand Scholz, and Prof. Dr. Udo W. Pohl, for reviewing this thesis.

I appreciate the fruitful, critical, and constructive discussions with Prof. Dr. Udo W. Pohl, Prof. Dr. André Strittmatter, and Dr. Tim Wernicke. They supported me with their scientific experience to learn many secrets of epitaxial alchemy.

All the measurements and analysis of thousands of samples would not have been possible without the help of six remarkable students. Tino Simoneit, Farsane Tabataba-Vakili, Torsten Ernst, Wenera Zent, Alexander Sabelfeld, and Gökhan Kurt tested my scientific expertise and taught me patience.

I am grateful to all scientific collaborations, like AlN template support from the Ferdinand-Braun-Institut, Leibniz-Institut für Höchstfrequenztechnik with Prof. Dr. Markus Weyers, Dr. Arne Knauer, and Dr. Viola Küller; micro photoluminescence at the Technische Universität Berlin with Prof. Dr. Axel Hoffmann, Dr. Gordon Callsen, and Stefan Kalinowski; scanning transmission electron microscopy and cathodoluminescence at the Universität Magdeburg with Prof. Dr. Jürgen Christen, Gordon Schmidt, and Alexander Reuper; high-resolution transmission electron microscopy at the Leibniz Institute for Crystal Growth with Dr. Martin Albrecht, Dr. Toni Markurt, and Dr. Tobias Schulz; cleanroom processes in the Nano Photonic Center with Ronny Schmidt, Stefan Bock, Monir Ryschetsky, and Dr. Luca Sulmoni; positron spectroscopy at the Aalto University with Prof. Dr. Filip Tuomisto and Tanja Heikkinen; and tip-enhanced Raman spectroscopy with Dr. Emanuele Poliani.

## Chapter 7. Acknowledgments

I would like to thank the research training group of the Collaborative Research Centre 787 and the whole workgroup for the stimulating atmosphere, in particular, my office mates Jan-Robert van-Look, Ralph Debusmann, Dr. Martin Frentrup, Dr. Frank Mehnke, and Johannes Enslin.

Last but not least, I express my deepest gratitude to my family, especially to my wife Anja Bellmann, who supported me in any situation.

Berlin, den 25.11.2017